UNIVERSITY OF CALIFORNIA,
IRVINE

Computational characterization of the electroencephalogram in patients with infantile spasms syndrome

DISSERTATION

submitted in partial satisfaction of the requirements
for the degree of

DOCTOR OF PHILOSOPHY

in Biomedical Engineering

by

Rachel June Smith

Dissertation Committee:
Assistant Professor Beth A. Lopour, Chair
Professor Zoran Nenadic
Professor Frithjof Kruggel

2019

DEDICATION

To

my parents, who sacrificed so much.

[6] Do not forsake wisdom, and she will protect you;
love her, and she will watch over you.
[7] The beginning of wisdom is this: Get wisdom.
Though it cost all you have, get understanding.

Proverbs 4:6-7

TABLE OF CONTENTS

LIST OF FIGURES

LIST OF TABLES

ACKNOWLEDGMENTS

I would first like to thank my mentor and ally, Dr. Beth Lopour, for her extraordinary leadership throughout my time at UCI. She prioritized my learning in every situation, and it was a joy to work alongside her these past five years.

This dissertation could not have been possible without our clinical collaborator, Dr. Daniel Shrey. His tireless diligence in gathering data for our lab was invaluable, and he has set the bar extremely high for clinical collaborators in the future.

I would also like to acknowledge our other collaborators: Dr. Shaun Hussain, Dr. Rajsekar Rajaraman, Dr. Hernando Ombao, and Dr. Virginia Liu. I thoroughly enjoyed working with each one of these brilliant people, and I hope we can maintain contact in the future.

Completing a PhD is not an easy task; my friends and family supported me every step of the way. I thank them for their willingness to help in any way possible. I only hope I can give back a portion of the joy they have brought me over these years.

My parents sacrificed so much for their children's education. They taught us to value hard work and to reach for big dreams. I only hope they see how impactful their help has been to me in this endeavor. I believe humanity will benefit from their sacrifice.

Lastly, I want to thank Dr. Mackenzie Turvey for his unwavering support throughout graduate school. Without his influence, I may never have pursued graduate school at all.

CURRICULUM VITAE

(423) 505-8931 • racheljs@uci.edu

Education

2019	Ph.D., University of California, Irvine Biomedical Engineering Advisor: Beth A. Lopour
2017	M.S., University of California, Irvine Biomedical Engineering
2014	B.S., University of Tennessee, Knoxville Biomedical Engineering

Peer-Reviewed Publications

Smith RJ, Sugijoto A, Rismanchi N, Hussain SA, Shrey DW, Lopour BA: Long-range temporal correlations reflect treatment response in the electroencephalogram of patients with infantile spasms. *Brain Topography*. 30(6), pp 810-821. Nov 2017.

Duty CE, Kunc V, Compton B, Post BK, Erdman D, **Smith RJ**, Lind RF, Lloyd P, Love LJ: Structure and mechanical behavior of Big Area Additive Manufacturing (BAAM) materials. *Rapid Prototyping Journal*. 23(1), pp 181-189. Jan 2017.

Rao P, Kong Z, Duty CE, Kunc V, **Smith RJ**, Love LJ: Assessment of Dimensional Integrity and Spatial Defect Localization in Additive Manufacturing (AM) using Spectral Graph Theory (SGT). *Journal of Manufacturing Science and Engineering.* 138(5), 051007. Nov 2015.

Love LJ, Kunc V, Rios O, Duty CE, Elliot A, Post BK, **Smith RJ**, Blue C: The Importance of Carbon Fiber to Polymer Additive Manufacturing. *Journal of Materials Research*. 29(17), pp 1893-1898. Sept 2014.

Manuscripts in Submission or Preparation

Smith RJ, Shrey DW, Alipourjeddi E, Lopour BA: Temporally-evolving functional networks in infant scalp EEG. *Human Brain Mapping.* (in preparation)

Smith RJ, Shrey DW, Rajaraman R, Hussain SA, Lopour BA: Computational electroencephalographic biomarkers of epileptic spasms. *Epilepsia.* (in preparation)

Smith RJ, Shrey DW, Ombao H, Lopour BA: Inference on Long-Range Temporal Correlations in Human EEG Data. *Journal of Biomedical and Health Informatics*. (under review)

Ngo D, Chau J, Lopour BA, Sun Y, **Smith RJ**, Shrey DW, Ombao HC: A Geometric Approach to Visualization and Testing of Coherence Matrices of Multivariate Time Series. *JASA.* (under review)

Conference Papers

Smith RJ, Shrey DW, Hussain SA, Lopour BA: Quantitative Characteristics of Hypsarrhythmia in Infantile Spasms. *40th International Conference of the IEEE Engineering in Medicine and Biology Society.* July 2018.

Rao P, Kong Z, Duty CE, **Smith RJ**: Three Dimensional Point Cloud Measurement Based Dimensional Integrity Assessment for Additive Manufactured Parts Using Spectral Graph Theory. *ASME 11th International Manufacturing Science and Engineering Conference.* June 2016.

Dinwiddie RB, Kunc V, Lindal JM, Post BK, **Smith RJ**, Love LJ, Duty CE: Infrared Imaging of the Polymer 3D-Printing Process. *SPIE Defense, Security and Sensors Conference.* Jun 2014.

Invited Talks

Smith RJ (2017, Oct): *Computation in Epilepsy Research*. Talk given at Lee University in an undergraduate psychology course. Invited by Dr. Robert Fisher, Department of Behavioral & Social Sciences. Cleveland, TN.

Smith RJ, Sugijoto A, Rismanchi N, Kim O, Shrey DW, Hussain SA, Ombao HC, Lopour BA (2017, Feb): *Network Quantification in the EEGs of Infantile Spasms Patients.* Talk presented at the Big Data in Brain Science Workshop hosted by the Data Science Initiative at UC Irvine. Invited by Dr. Hernando Ombao, Department of Statistics. Irvine, CA.

Conference Presentations

Smith RJ, Ombao CH, Hussain SA, Shrey DW, Lopour BA (2018, Nov): *Long-range Temporal Correlations in EEG as a Marker of Treatment Response for Infantile Spasms.* Oral presentation at the Computational Neuroimaging and Neuroengineering Symposium at the University of California, Riverside.

Smith RJ, Shrey DW, Hussain SA, Lopour BA (2018, July): *Quantitative Characteristics of Hypsarrhythmia in Infantile Spasms*. Poster presented at the 40th International Conference of the IEEE Engineering in Medicine and Biology Society in Honolulu, HI.

Smith RJ, Shrey DW, Hussain SA, Lopour BA (2017, June): *Temporal and Spectral Characteristics of Hypsarrhythmia in Infantile Spasms*. Poster presented at the 9th Annual Pathways to Cures: Translational Science Research Day by the Institute of Clinical and Translational Science at the University of California, Irvine.

Smith RJ, Sugijoto A, Rismachi N, Shrey DW, Lopour BA (2016, Dec): *Measurement of Treatment Response in Infantile Spasms Patients Using Long-range Temporal Correlations.* Poster presented at the 70th annual meeting of the American Epilepsy Society in Houston, TX.

Smith RJ, Sugijoto A, Shrey DW, Lopour BA (2016, June): *Prediction of Treatment Outcome in Infantile Spasms Patients.* Talk and poster presented at the 8th Annual Pathways to Cures:

Translational Science Research Day by the Institute of Clinical and Translational Science at the University of California, Irvine.

Smith RJ, Sugijoto A, Shrey DW, Lopour BA (2016, June): *Prediction of Treatment Outcome in Infantile Spasms Patients.* "Rapid-Fire Talk" and poster presented at the 17th Annual UC Systemwide Bioengineering Symposium in San Francisco, CA.

Smith RJ, Post BK, Lind RF, Love LJ (2014, Oct): *Novel Methodology for Custom Orthotic Design and Manufacturing*. Poster presented at the IEEE-NIH Special Topics Conference on Healthcare Innovations and Point-of-Care Technologies Conference in Seattle, WA.

Record of Invention Submissions

2018 **TherapyScore: A Quantitative Hypotension Treatment Indicator**: Edwards Lifesciences. Irvine, CA. (Main inventor)

2014 **Breakaway Supports for Large-Scale Additive Manufacturing**: Oak Ridge National Laboratory. Oak Ridge, TN. (Supporting inventor)

Awards and Scholarships

2018 ***Computational Neuroimaging and Neuroengineering Symposium: Best Oral Presentation***
University of California, Riverside

2018 ***PITT Future Faculty Development Program*** **[$1,200]**
University of Pittsburgh
Travel and lodging expenses awarded to participants of the NSF-funded faculty development program.

2018 ***Henry Samueli School of Engineering Pedagogical Fellow*** **[$5,000]**
University of California, Irvine
Provide pedagogical training and advice to graduate students and faculty in the School of Engineering. Implement special initiatives to aid integration of evidence-based teaching practices in undergraduate engineering education.

2018 ***Graduate Dean's Dissertation Year Fellowship*** **[$23,554]**
University of California, Irvine
Awarded to nineteen students across UCI campus to encourage doctoral degree completion. The award provides stipend and in-state tuition for two quarters of the dissertation year.

2018 ***Most Promising Future Faculty Award*** **[$9,528]**
University of California, Irvine
One of two graduate students selected from campus-wide pool of nominees that exemplify excellence in teaching, research, and service to the university. The award is comprised of a one- quarter dissertation fellowship and fee waiver.

2018 ***Pedagogical Fellows Program*** **[$2000]**
University of California, Irvine
Graduate students are selected from across campus to enroll in classes focused on evidence-based teaching principles. Pedagogical Fellows lead the TA training

course before the start of the school year to train fellow graduate students in how to teach undergraduates most effectively.

2017 ***Fletcher Jones Fellowship: Henry Samueli School of Engineering Nominee***
University of California, Irvine
One graduate student is selected from each School to compete for the one-year fellowship awarded from the Fletcher Jones Foundation. The award assists with doctoral degree completion.

2016, 2017 ***Biomedical Engineering Graduate Student of the Year Award***
University of California, Irvine
Awarded to one graduate student in the Biomedical Engineering department for excellence in teaching and mentorship. Recipients are chosen by undergraduate students. (2 consecutive years)

2016 ***Inaugural Summer Course in Adaptive Neurotechnologies*** **[$1400]**
National Center for Adaptive Neurotechnologies, Albany, NY
Funding awarded to students participating in the three-week workshop for travel, room and board.

Teaching Experience

2018 ***Guest Lecturer****: Neural Time Series* (graduate course, Spring)
"Inter-trial phase clustering and phase/power relationships"

2017 ***Guest Lecturer***: *Quantitative Physiology I: Sensory Motor Systems* (Fall)
"Muscle Force/Velocity Relationships"

2017 ***Teaching Assistant***: *Biomechanics II: Dynamics* (Winter)
Students use Newton's laws to understand how objects accelerate under unbalanced forces. I led discussion sections in which we solved example and practice problems.

2016 ***Guest Lecturer***: *Quantitative Physiology I: Sensory Motor Systems* (Fall)
"Muscle Energetics and Fatigue"
"Epilepsy: Mechanisms and Technology"

2016 ***Teaching Assistant***: *Quantitative Physiology I: Sensory Motor Systems* (Fall)
Students mathematically model physiological processes in the nervous, musculoskeletal, and auditory system. I guided students' quarter-long project in which they designed a brain-computer-interface-controlled hospital bed.

2016 ***Teaching Assistant***: *Biomechanics II: Dynamics* (Winter)

2016 ***Teaching Assistant***: *Biomedical Engineering Senior Lab: EEG* (Spring)
Students learned how to operate EEG equipment and analyze EEG data to extract features pertinent to attention. I supervised and guided the use of the equipment and analysis and graded their final lab reports.

2015 ***Teaching Assistant***: *Quantitative Physiology I: Sensory Motor Systems* (Fall)

Certifications

2018 ***Certificate in Mentoring Excellence:*** *Graduate Division*

Six-module course focused on skills and resources related to mentorship. The twelve-hour course covered topics such as ethics, communication, diversity, conflict resolution, and wellness.

2017 ***Center for Integration of Research, Teaching, and Learning (CIRTL) Associate:***
UCI Center for Engaged Instruction
CIRTL is an NSF, SLOAN, and GLHEC-funded Center dedicated to growing STEM faculty in pedagogy and research. Completion of evidence-based teaching training, participation in a learning community, learning through diversity, and teaching as research earns Associate level.

2017 ***Certificate in Teaching Excellence****: UCI Center for Engaged Instruction*
Quarter-long class focused on pedagogical training in evidence-based practices to best facilitate learning. The course required three peer observations of teaching.

2017 ***Course Design Certification Program****: UCI Center for Engaged Instruction*
Eight-hour workshop series centered on undergraduate-level course design. The course culminated in the creation of a syllabus for the designed course.

Professional Development

2018 ***PITT Future Faculty Development Program****: University of Pittsburgh, Pittsburgh, PA*
Two-day workshop aimed to prepare future STEM faculty for a career in academia. Talks and workshops included the application process, balancing service obligations, negotiating start-up packages, grant-writing, and publishing best practices.

2018 ***Algorithms R&D Intern****: Edwards Lifesciences, Irvine, CA*
Summer internship in the Critical Care Division of a global cardiovascular device company. Developed a quantitative scoring system derived from hemodynamic parameters calculated from the arterial blood pressure waveform. The score provides decision support to clinicians to administer specific therapies to avoid hypotensive events in the operating room during surgery.

2018 ***Pedagogical Fellows Program****: Division of Teaching Excellence and Innovation*
Year-long training program for graduate students to receive targeted training in evidence-based teaching practices. The first two quarters focus on advanced pedagogy. PFs then lead TA summer trainings for graduate students new to TAships. The last quarter focuses on academic job preparation.

2017 ***Big Data in Brain Science Workshop****: UCI Data Science Initiative*
Graduate students and faculty presented tutorials and current research highlighting advances in the analysis of big data in neural computation.

2016 ***Inaugural Summer Course in Adaptive Neurotechnologies****: National Center for Adaptive Neurotechnologies, Albany, NY*
Twenty-four students from across the US were chosen to participate in a three-week-long course on the advancement of adaptive neurotechnologies.

2014 ***Mechanical R&D Intern****: Oak Ridge National Laboratory, Manufacturing Demonstration Facility*

Assessed geometric integrity of additive manufactured parts using spectral graph theory and proposed a novel method to manufacture custom orthoses with a pilot design for amputee Army veteran.

2013 ***Mechanical R&D Intern****: Oak Ridge National Laboratory, High Flux Isotope Reactor*
Determined the experimental resolution of the CG-3 Bio-SANS Velocity Selector with the neutron sciences group.

2013 ***Undergraduate Research****: University of Tennessee, Knoxville*
Mentor: Dr. Xiaopeng Zhao
Expanded smartphone technology to determine heart rate variability parameters using comparative PPG and ECG signals analysis.
Machine Learning Study Group: Attend and present papers on current literature in machine learning techniques.

Professional Service and Mentorship

2019 ***Henry Samueli School of Engineering Pedagogical Fellow:*** surveyed Engineering professors regarding graduate student lecture experience, organized and led 4-week Engineering Pedagogy Reading group, panelist for MAE 295: Developing Teaching Excellence, peer-reviewed teaching philosophy statements.

2018, 2019 ***TA Professional Development Program (TAPDP) Instructor:*** led two 12-hour (1.5 day) training workshops designed to prepare new engineering Teaching Assistants for their role in the classroom. Topics included Lesson Planning, Active Learning, Grading, Office Hours, Diversity and Inclusion, and others. My sections enrolled 25 and 22 graduate TAs.

2018 ***Pedagogical Liaison Mentor:*** co-mentored graduate student interested in pedagogy and enrolled in the Division of Teaching Excellence and Innovation's Pedagogical Liaison program. Pedagogical Liaisons perform ten hours of service to the university while learning from Pedagogical Fellows about evidence-based teaching practices.

2018 ***Graduate InterConnect Program Peer Mentor:*** provided incoming international graduate students with support through email communications over the summer, International Graduate Student Orientation, and face-to-face interaction in the Fall quarter. We planned social events, maintained a FAQ blog, and connected with our mentees through their first months in the US.

2017 ***Interdisciplinary Reading Group in Systems Neuroscience Co-organizer:*** interested graduate students meet to discuss current topics and models from systems neuroscience literature.

2017 ***Graduate Association of Biomedical Engineering Students (GABES) Alumni Committee member:*** invited alumni to campus for an event promoting professional development/networking for BME graduate students.

2017 ***DECADE (Diverse Educational Community and Doctoral Experience) BME Student Representative*****:** moderated workshop "Developing a Teaching CV",

attended community meetings, served as liaison between BME students and faculty mentor, wrote articles for DECADE press.

2017 ***GABES-BMES Mentor-Mentee program*:** Mentored undergraduate BME student navigating college life in engineering.

2017 ***Research Mentor:*** Mentored undergraduate student on a project in EEG artifact detection. The project culminated in a poster presentation in the 2017 Undergraduate Research Symposium.

2016 ***"MATLAB Basics" Presenter for IEEE Club:*** led two-hour workshop focused on basic programming in MATLAB for undergraduates in the IEEE club.

STEM Outreach

2019 *Moderator for DECADE Panel: Elements of the Teaching CV. UC Irvine. Irvine, CA.*

2018 *Panelist for NASA-funded CSULA DIRECT-STEM project: Applying for Graduate School. UC Irvine. Irvine, CA.*

2018 *Panelist for Engineering STEM Prep Night. Samueli Academy. Santa Ana, CA.*

2018 *Volunteer demonstrator of EMG signal acquisition at Imaginology Fair for K-12 grade students. OC Fairgrounds. Costa Mesa, CA.*

2018 *Panelist for Multicultural Symposium: Women in STEM Fields. Sage Hill High School. Newport Beach, CA.*

2018 *Volunteer demonstrator at Perry Elementary Science Night with GABES (Graduate Association of Biomedical Engineering Students). Huntington Beach, CA.*

2017 *Volunteer judge for the Junior Science and Humanities Symposium for high school students in Southern California. UC Irvine.*

2017 *Speaker at Brews and Brains: Orange County Community Meetup to give TED-style talk about the quantitative EEG in the diagnosis and treatment of infantile spasms, my research at UC Irvine.*

2017 *Panelist for GiGaTEC (Girls Gateway to Technology and Engineering Careers) inaugural event: my experience as an athlete and a woman in STEM. UC Irvine.*

2014 *Instructor in Veteran Workshop Training Project: Reverse engineering with high-resolution laser scanning. Manufacturing Demonstration Facility, Oak Ridge National Laboratory. Knoxville, TN.*

2014 *Invited lecture: "What is Engineering: A Student's Perspective". Girls Preparatory School. Chattanooga, TN.*

ABSTRACT OF THE DISSERTATION

Computational characterization of the electroencephalogram in patients with infantile spasms syndrome

By

Rachel June Smith

Doctor of Philosophy in Biomedical Engineering

University of California, Irvine, 2019

Assistant Professor Beth A. Lopour, Irvine, Chair

Infantile spasms (IS) is a potentially catastrophic epileptic encephalopathy that typically presents in children six to twelve months of age and is characterized by clusters of seizures consisting of abrupt muscle spasms. IS is associated with a host of comorbidities, high mortality rates, debilitating neurocognitive stagnation and psychomotor delay, and often progresses to other highly refractory forms of epilepsy. Diagnosis and clinical treatment decisions in IS are difficult due to the wide range of underlying etiologies and concomitant epilepsies. Patients with IS also exhibit a broad spectrum of electroencephalographic (EEG) morphologies, including a disorganized, high-amplitude pattern called hypsarrhythmia. Additionally, although the presence of hypsarrhythmia is often used as a diagnostic criterion for IS, there is low inter-rater reliability for identification of the pattern, and it is not a strong predictor of outcome. This lack of diagnostic accuracy and inefficient treatment response evaluation can delay successful treatment, which is associated with worse long-term outcomes.

Computational EEG biomarkers of IS that are independent of the presence of hypsarrhythmia could supplement standard visual inspection of the EEG and enable objective identification of the disease and assessment of treatment response. We quantified basic characteristics of the pre-treatment EEG signal such as the amplitude, power spectrum, and Shannon entropy in cohorts of IS patients both with and without hypsarrhythmia. We identified significant differences between IS patients and age-matched control subjects, and these differences were robust to the presence of hypsarrhythmia. We also investigated the strength of long-range temporal correlations in the EEG with detrended fluctuation analysis (DFA) and developed statistical methods to infer confidence intervals for this metric. DFA differentiated IS patients from control subjects and reflected treatment response in post-treatment data. Lastly, we calculated EEG-based functional connectivity networks via cross-correlation and characterized long-term functional connectivity network changes in IS patients over multiple days. Analysis of normal control subjects allowed us to account for physiological fluctuations of the functional connections during sleep/wake cycles. In all, this work describes the pathological features of IS EEG data, providing an objective basis for diagnosis and laying the groundwork for early biomarkers of treatment response.

CHAPTER 1

BACKGROUND

1.1 Epilepsy and Infantile spasms syndrome

1.1.1 Definitions and key terms

Epilepsy is a chronic neurological disease that affects nearly 65 million people worldwide [1]. According to the International League Against Epilepsy (ILAE), the disease is defined by any of the following conditions: "1) at least two unprovoked (or reflex) seizures occurring more than 24 hours apart; 2) one unprovoked (or reflex) seizure and a probability of further seizures similar to the general recurrence risk (at least 60%) after two unprovoked seizures, occurring over the next 10 years; or 3) diagnosis of an epilepsy syndrome [2]". A *seizure* is defined to be "a transient occurrence of signs and/or symptoms due to abnormal excessive or synchronous neuronal activity in the brain [2]." Following these definitions, clinicians diagnose and treat cases of epilepsy according to a variety of factors including the patient's seizure type, etiology, and age [2].

Infantile spasms syndrome (IS) is one of eight epilepsy syndromes the ILAE has classified as an epileptic encephalopathy [3]. Epileptic encephalopathies are conditions in which "the epileptiform abnormalities themselves are believed to contribute to the progressive disturbance in cerebral function" [4]. Epileptic encephalopathies are generally unresponsive to standard therapies, and this can cause devastating neurocognitive effects later in life [3].

1.1.2 Types of seizures

Epileptic seizures are generally divided into three categories: focal seizures (formerly termed *partial* seizures), generalized seizures, and unknown [5]. Focal seizures originate in a small population of neurons and oftentimes propagate to other regions or whole hemispheres of the brain in what is called “secondary generalization” [6]. The symptoms of focal seizures vary widely because they depend on the location of the seizure focus within the brain [6]. Focal seizures are also subdivided into two categories: those in which the patient retains awareness and those in which awareness is impaired [5]. If the patient loses consciousness, it is most often that the focal seizure has secondarily generalized [6]. However, before this secondary generalization occurs, patients may experience *auras*. Auras are caused by the initial abnormal electrical activity within the seizure focus and can produce sensations of fear, a rising feeling in the abdomen, or specific odors [6].

Generalized seizures, on the other hand, begin without auras and involve both hemispheres of the brain [6]. Generalized seizures are further separated into convulsive and non-convulsive seizure types (also called motor and non-motor seizures) [5]. Formerly called the *grand mal* seizure, the most prototypic convulsive seizure involves tonic-clonic movements [6]. The most common non-convulsive generalized seizures are called *absence* seizures and occur most often in children [6]. These seizures are associated with a loss of consciousness, but the patient maintains posture, and the events often do not last longer than 15 seconds [6]. The patient may or may not have motor abnormalities accompanying the seizure, like lip smacking or eyelid fluttering [7].

Epileptic spasms are classified as an unknown seizure type. In IS, the spasms are identified clinically as a sudden and brief contraction of axial and proximal limb muscles followed by longer tonic contractions [7], [8]. In rarer cases, the tonic component is absent and

only the initial phasic component is seen [9]. The semiology of the spasms may vary significantly depending on the muscle groups involved and whether the patient is supine or sitting during the attack [9]. Spasms are symmetric in most cases, but a variety of asymmetric or focal signs may be detected [7]. Because the spasms are not motor seizures, it is rarer to see head or eye deviation or hand or foot contractions [7]. The spasms occur mostly in clusters and can be precipitated by arousal from sleep, transitioning from NREM sleep to REM sleep, handling, and loud noises [7], [10]. The cluster will begin and end mildly, but spasms increase in intensity during the middle part of the cluster [7]. There can be as many as 100 spasms in a cluster, and the attack can last over ten minutes [9], [11].

1.1.3 Etiologies associated with epilepsy and IS

Although seizure classification is important in the diagnosis and treatment of epilepsy, the disease is not only defined by the seizure type. It is clinically important to determine what caused the seizures to begin so therapies can target the underlying cause [12]. Epilepsy etiology is categorized into three groups, according to the ILAE: genetic, structural/metabolic, and unknown [12].

Genetic epilepsies "are a direct result of a known or presumed genetic defect(s) in which seizures are the core symptom of the disorder" [12]. As of 2013, over 70 genes have been linked to an epileptic phenotype and over half of these genes were discovered in humans [6], [13]. These genetic mutations can cause defects in ion channel units, proteins involved in synaptic transmission, vesicle proteins, synaptic receptors, and molecules involved in Ca^{2+} signaling [6]. It is estimated that genetic factors account for about 40% of epilepsy etiologies; however, Mendelian epilepsies (those that can demonstrate inheritance) only account for 1% of these cases

[14]. Thus, most cases are multigenic, commonly referred to as “complex epilepsy”, and the role environmental factors play in susceptibility to epilepsy in combination with genetic components is still to be determined [14].

Structural and metabolic defects define a second etiological classification of epilepsy. These epilepsies can arise due to metabolic causes such as aminoacidopathies, but also structural lesions from stroke, trauma, brain tumors, and infection [1], [12]. An epilepsy can still be classified in this group if the structural/metabolic cause of the disease has strong genetic connections, such as tuberous sclerosis or cortical malformations [12]. It is hypothesized that seizures arise from structural lesions in a maladaptive response to the injury [6]. For example, patients that experience cortical injury due to head trauma can develop seizures several months after the incident. The emergence of pathological neuronal behavior could be due to axonal sprouting, alterations in dendritic structure, changes in control of transmitter release, and variation in activity of ion channels and pumps that resulted from the impact [6]. Although direct implications are yet to be found, these changes are believed to induce hyperexcitability and a specific electro-chemical process important in epileptogenesis called *kindling* [6].

Infantile spasms is associated with as many as 200 different etiologies [15], and these underlying causes are often divided into three etiological groups according to the prior ILAE definitions: symptomatic, cryptogenic, and idiopathic (they were recently replaced with the terms genetic, structural-metabolic, and unknown) [7], [8]. The term *symptomatic* refers to cases of infantile spasms that arise from a diagnosed underlying disorder and account for more than 70-80% of cases [7], [16]. *Cryptogenic* cases refer to those in which no specific cause can be identified, but the patient exhibits neurological symptoms, signs, or developmental delay. The

idiopathic group includes cases with no detectable underlying cause and in which no neurological symptoms or signs can be identified [8].

According to a British study of 207 infants, the most common symptomatic etiologies are hypoxic-ischemic encephalopathy (HIE), chromosomal malfunctions, brain malformations, stroke, and tuberous sclerosis [17]. Cerebral malformations in the prenatal periods are a major cause of infantile spasms; abnormal neurogenesis, neuronal migration and neuronal organization can manifest with cortical dysplasia, microcephaly, agyria/polygyria, and heterotopias [7]. Genetic etiologies account for 13% of the symptomatic IS population, with the most common chromosomal abnormalities including Down syndrome and X-linked genes such as CDKL5 in female patients and ARX in male patients [7]. Studies in monozygotic twins [18] and familial risk [19] also support strong genetic components in these cases.

1.1.4 Incidence and prevalence of epilepsy and IS

The incidence and prevalence of epilepsy varies by age and by world region. Prevalence of epilepsy is lowest early in life, peaks around adolescence, and gradually decreases after age 30 [20]. The incidence of epilepsy is higher in those under 18 years of age (46.9/100,000 person-years) compared with those 19 years of age and above (34.63/100,000 person-years) [20]. A 2017 meta-analysis of epilepsy epidemiology reported significantly higher active annual period prevalence and incidence rate of epilepsy in low-middle income countries than high-income countries. The prevalence was 5-8/1000 in high-income countries and 10/1000 in low-income countries and even higher rates were observed in rural areas [1], [20]. These differences by country income can be attributed to the expense or inaccessibility of anti-epileptic drugs, as well as levels of risk for infections and levels of antenatal and perinatal care [1], [20]. Interestingly,

the cumulative incidence of epilepsy was higher in high-income countries in comparison to low-income countries, but this may be attributed to the lower premature mortality rate and better diagnostic techniques in high-income countries [20].

Infantile spasms (IS) strikes within the first year of life in 90% of cases [8]. The incidence of infantile spasms is 2-5/10,000 newborns with a slight male dominance [8], [9], however the incidence rates can vary widely, even among high-income countries [21]. The onset of spasms occurs at a peak age of 4 to 7 months and spasms typically persist 25 to 32 months [8]. The age-specific prevalence of IS is 1-2/10,000 by the age of 10 years, with the highest prevalence corresponding to high geographic latitudes [21]. Infantile spasms constitutes approximately 34% of all epilepsies diagnosed within the first year of life, which has an incidence rate of 124/100,000 [22]. The next most common epilepsy diagnosis for children under 12 months is benign infantile epilepsy, which has an incidence rate of 22/100,000 [22]. This places extreme importance on accurate diagnostic tools, as a misdiagnosis of IS for benign infantile epilepsy can have severe neurocognitive consequences for the patient later in life.

1.1.5 Comorbidities of epilepsy

In addition to the burden of the disease itself, epilepsy patients are often diagnosed with comorbidities, conditions that occur during the course of another disease, at a higher rate than the general population [23]. Physical comorbidities such as heart disease, peptic ulcers, arthritis, and migraines are up to eight times more common in epilepsy patients [23]. Psychiatric comorbidities such as depression and anxiety are twice as prevalent among people with epilepsy, and are highly associated with reduced quality of life and poor seizure outcomes [23]. Epilepsy increases chances of premature mortality [23]. Nearly all mortalities are due to comorbidities, with

neoplasms, cardiovascular disease, and cerebrovascular disease posing the greatest risks [23]. The mortality rates from epilepsy are higher in lower-income countries (37 times greater than the general population) than higher income countries (2-5 times greater than the general population) [1]. Although SUDEP (Sudden Unexpected Death in Epilepsy) is generally regarded as the most common cause of death in high-income countries [1], one study showed that only 4% of deaths attributed to SUDEP had no comorbid association [24]. However, in lower-income countries and rural areas drowning or status epilepticus are more common and account for more epilepsy-related and SUDEP deaths [1], [24].

In children with epilepsy, the odds ratios (OR) for comorbid conditions are amplified even further [25]. Children with "complicated epilepsies", defined as any other diagnosed neurologic/developmental disorder, were at much greater odds to experience malnutrition (OR = 27.9), chromosomal abnormalities (OR = 31.9), sleep disorders (OR = 17.9), visual impairment or blindness (OR = 50.3), and intellectual disability (OR = 84.0) [25].

1.1.6 Diagnosis of epilepsy and IS

Diagnosis of epilepsy begins with descriptions about seizure semiology from friends and family, but it is preferable to capture the seizures on video in the clinic. Procedures to diagnose different types of epilepsy require different tests, but almost all require a personal and family history, a recount of the age of onset, an identification of seizure type, a neurological and cognitive status examination, a 12-lead electrocardiogram (ECG) to rule out cardiac abnormalities, and an interictal electroencephalogram (EEG) [1]. Brain magnetic resonance imaging (MRI) is common, except when the patient presents with typical syndromes, and lumbar puncture and blood tests can also be used to confirm or reject specific causes [1]. Diagnostic

biomarkers can help clinicians provide objective basis for a diagnosis of epilepsy [26]. Some proposed diagnostic biomarkers include the presence of high-frequency oscillations in intracranial or scalp EEG [27], [28], the differential and increased/decreased expression of specific microRNAs [29], [30], and reduced temporal lobe white matter fractional anisotropy on diffusion tensor imaging [31], though these are not yet standard clinical practice.

Similar to other forms of epilepsy, diagnosis of infantile spasms begins with a physical examination of the patient [9]. Diagnosis of infantile spasms is difficult because of the wide variation in spasm semiology; spasms can be a slight head nod or violent muscle contractions [9]. Parents may not recognize the abnormal movements and delay taking the child to a pediatrician [9]. Even in the clinic, subtle spasms may be misdiagnosed for gastroesophageal reflux, constipation, colitis, or benign infantile epilepsy [32]. Additionally, even after an IS diagnosis, parents often substantially underestimate the frequency of the spasms [9].

Once infantile spasms is suspected, the ictal and interictal EEG are required for diagnosis. The clinician visually assesses the EEG for signs of positive-vertex slow waves, spindle-like activity, and diffuse flattening (i.e. voltage attenuation) during ictal periods, as well as a stereotypical EEG pattern called *hypsarrhythmia* during interictal periods [9], [33]. The characteristics of hypsarrhythmia are further discussed in Section 1.2.4. Visual assessment of these patterns is challenging and has unacceptably low interrater reliability [34], [35], and this has drastic implications for prompt treatment initiation in these patients.

1.1.7 Treatment of epilepsy and IS

After an epilepsy diagnosis, clinicians must decide how to treat the disease. The goal of treatment is a *resolution* of epilepsy. According to the ILAE: “Epilepsy is considered to be

resolved for individuals who had an age-dependent epilepsy syndrome but are now past the applicable age or those who have remained seizure-free for the last 10 years, with no seizure medicines for the last 5 years [2].” *Resolution* was chosen by the ILAE instead of “cured” because a history of epilepsy indisputably places the risk of future seizures higher than the risk in the general population [2]. However, the term “in remission” does not convey the absence of the disease in those that were successfully treated [2]. *Resolution* implies the patient no longer has epilepsy but does not guarantee it will not return [2].

The first line treatment of epilepsy is anti-epileptic drugs (AEDs). The selection of a specific AED depends on factors such as the seizure type, the possibility of adverse effects, the pharmacokinetic properties, ease of use, and cost [36]. The majority of the AEDs act by blocking voltage-dependent sodium channels or calcium channels, but some mainly operate by increasing GABA activity levels [36].

Most patients who become seizure-free due to treatment with AEDs respond to the initially prescribed drug [1]. If a patient’s seizures are not controlled after the first-line treatment, the clinician will often consider alternative monotherapies or combination therapies (after treatment protocol non-adherence is ruled out) [1]. However, the probability of the patient responding to therapies administered after the first-line treatment diminishes proportionally to the number of alternative drugs tested [1]. Thus, if the patient has seen no reduction in the seizure frequency after the fist- or second-line AEDs, the disease is designated as a “drug-resistant epilepsy” and the clinician may look to alternative methods [37]. These include surgical intervention, neurostimulation, diet therapies, and some exploratory therapeutic approaches [38].

Neurosurgery has been regarded as a “last resort” for treatment of drug-resistant epilepsy in spite of the American Academy of Neurology’s recommendation for referral for surgical

evaluation after failing AED therapy [37]. In specific cases of focal epilepsy, surgical resection of the epileptic tissue provide much higher chances of seizure freedom than the continuation of another AED [39]. Patients that are not good surgical candidates may be candidates for therapeutic brain stimulation [38]. Although the curative mechanisms of the various forms of stimulation remain elusive, vagus nerve stimulators (VNS) and deep brain stimulation (DBS) have provided up to a 50% reduction in seizure frequency in some patient populations [40]. Lastly, alternative therapies such as a ketogenic diet, antioxidant therapy, and newer therapies such as gene therapy, cell therapy, and exosome therapy have been indicated for some drug-resistant epilepsy patients [38].

The treatment of infantile spasms is extremely difficult; the spasms are highly refractory and conventional AEDs are considered ineffective [7]. Two therapies, namely adrenocorticotropic hormone (ACTH) and vigabatrin, are the first-line AEDs in infantile spasms [41], [42]. The treatment choice between ACTH, vigabatrin, or a non-standard therapy and response rates can vary widely across different centers and studies; consensus on optimal treatment in all cases is not yet attained [43]. ACTH is administered daily at 1-2 IU/kg for two weeks and then tapered off [7]. ACTH has been reported to have a relapse rate of around 55%, but a second course of therapy can control seizures in approximately 75% of patients [7]. One important downside to ACTH is the severity of the side effects. Treatment-related mortality is as high as 5% and common side effects include infections, increased arterial blood pressure, gastritis, and hyperexcitability [7], [44]. Recent studies show similar efficacies in low-dose regimens of ACTH as opposed to high-dose, and lower doses may ameliorate some of the severe side effects of the therapy [45].

Vigabatrin has been shown to be more effective than ACTH in certain etiologies of IS such as tuberous sclerosis [41]. In general, vigabatrin has lower initial response rates but also lower relapse rates than ACTH (48% vs 74% for vigabatrin and ACTH, respectively) [7]. In one study of epileptic spasms due to tuberous sclerosis, vigabatrin achieved a 100% response rate [46]. The main side effect in vigabatrin is its retinal toxicity that produces irreversible visual field loss in around 20% of pediatric patients [7]. Lower doses of vigabatrin may reduce the chances of the patient experiencing these effects [7].

The United Kingdom Infantile Spasms Study (UKISS) prospectively compared hormonal therapy (ACTH) to vigabatrin in a multi-center randomized trial of 107 infants [47]. Seventy-five percent of all enrolled patients initially responded in both groups, half of the patients continued to be spasm free after 1 month, and 40% remained spasm free at 6 months [47]. If the first treatment failed, initiating the other had a good chance of response, which is atypical of AED therapies in other forms of epilepsy [1]. No differences in neurodevelopmental outcomes between treatments for symptomatic etiologies were found, but the Vineland adaptive behavior scale (VABS) scores were higher in the patients successfully treated with ACTH with cryptogenic etiologies [47].

Other therapies such as neurosurgery and the ketogenic diet are considered if the patient fails the first-line treatments of ACTH, vigabatrin, or other steroids such as prednisolone [9]. Neurosurgery is only applicable in infants with symptomatic IS with focal cortical abnormalities, and thus cannot be regarded as first-line in all cases. The ketogenic diet has shown insufficient efficacy to be a first-line treatment in IS, but can be considered if first-line treatments fail or have been deemed inappropriate for the patient (e.g. in some mitochondrial disorders) [9].

The cost associated with the treatment of infantile spasms is staggering [48]. The cost of medication *alone* in IS treatment can reach $93,100 [48]. For comparison, it is estimated that the cost of treating uncontrolled childhood epilepsy (not infantile spasms) can reach $5000 per year [49], [50]. Although this value is burdensome on families to be sure, it pales in comparison to the cost of infantile spasms treatment [48]. It is estimated that one round of treatment for IS, including hospitalization, outpatient, services, and medication costs reaches over $200,000 [48]. This value inflates further in refractory cases, as this implies more hospital visits and additional rounds of new therapies [49].

1.1.8 Forms of pediatric epilepsy associated with IS

Table 1.1.8.1 lists selected epileptic syndromes, categorized by age.

Table 1.1.8.1 Pediatric Epilepsy Syndromes [7]

Syndromes in the neonatal period	Benign familial neonatal epilepsy (BFNE)
	Ohtahara syndrome
Syndromes in infancy	Epilepsy of infancy with migrating partial seizures
	West syndrome
	Myoclonic epilepsy in infancy (MEI)
	Benign infantile epilepsy
	Benign familial infantile epilepsy
	Dravet syndrome
	Myoclonic encephalopathy in non-progressive disorders
Syndromes in childhood and adolescence	Lennox-Gastaut Syndrome (LGS)
	Childhood absence epilepsy (CAE)
	Rasmussen syndrome (RS)
	Progressive myoclonus epilepsies

In neonatal epilepsy syndromes such as BFNE, the prognosis is favorable: psychomotor development tends to be normal and patients do not develop subsequent epilepsies [7]. In others

forms of neonatal epilepsy, such as Ohtahara syndrome (also known as early infantile epileptic encephalopathy), the effects of the seizures can be devastating [7]. Ohtahara syndrome is associated with a suppression-burst EEG pattern, increased risk of mortality, severe neurological impairment, and progression to other age-dependent encephalopathies such as infantile spasms and Lennox-Gastaut syndrome [7].

Infantile epilepsies vary in seizure semiology, electrographic manifestations, and risk of mortality and comorbidity [7]. In addition to infantile spasms, Dravet syndrome is a severe myoclonic epilepsy that begins early in life, around 3-8 months of age, and is characterized by developmental delay and the progression of focal seizures into adulthood [7].

Lennox-Gastaut syndrome (LGS) is a childhood epilepsy that is preceded by infantile spasms syndrome approximately 30% of LGS cases, and follows infantile spasms in 20-50% of IS cases [7], [51]. LGS is defined by: "1) epileptic seizures: axial tonic, atonic and atypical absence; 2) EEG abnormalities: bursts of diffuse slow spike-waves during wakefulness and bursts of fast rhythmic waves and slow polyspikes and above all generalized fast rhythms at about 10 Hz during sleep; and 3) a slowness in intellectual growth and associated personality disorders [7]." Patients with LGS often cannot live independently, as over 80% of patients continue to have daily or weekly seizures into adulthood. It is prognostically unfavorable if LGS was preceded by infantile spasms syndrome [7].

1.1.9 Prognosis and long-term outcome in IS

Some groups have identified favorable prognostic factors in cases of infantile spasms [15]. Patients who are older when the spasms first begin have a greater chance of treatment success and better neurocognitive outcomes [15]. The specific etiology of the spasms does not

always predict clinical outcome [52], but cryptogenic etiologies generally respond better to treatment than patients with symptomatic etiologies [15], [53], [54]. The mortality rate is estimated to be 10% before the age of 3 [55]. Over 75% of the patients that survive past age 3 have below-normal intelligence levels [15], [56]. Psychiatric disorders, hyperkinetic behavior, and infantile autism are seen in 25% of patients [15]. Because IS often transitions into other forms of epilepsy such as Lennox-Gastaut syndrome, almost 70% of patients continue to have seizures, with around one-third of those experiencing daily seizures [15]. Shortening the lead time to treatment, the time delay between the onset of spasms and successful treatment, correlates to better patient outcomes [15], [55]. Accurate diagnoses and suitable treatment assessment tools shorten the lag time to successful treatment, improving overall outcomes [15], [55].

1.2 Electroencephalography

1.2.1 Neurophysiological basis of EEG

EEG is an indispensable tool for the diagnosis and follow-up of epilepsy patients. EEG provides a temporally-resolved picture of the electrical activity in the brain that can help clinicians localize pathological neuronal activity.

Neuronal activation can be described by two main processes: the first is the action potential, a fast depolarization of the neuronal membrane that is mediated by sodium and potassium voltage-dependent ionic conductances; the second is a slower change in the membrane potential due to synaptic activation associated with different neurotransmitter systems [57]. Although action potentials cause larger voltage changes than synaptic potentials, the synaptic potentials are longer and spread across a greater spatial area, allowing for both temporal and

spatial summation [58]. This summed activation can be large enough to be detected on the scalp [58].

The waveforms detected with EEG are dominated by the activity of cortical pyramidal neurons [59]. Excitation of post-synaptic neurons creates an extracellular voltage near the dendrites that is more negative than elsewhere along the neuron [59]. This creates a *dipole*, an element with two adjacent, oppositely charged sites [58]. The recording electrode measures the summed positive and negative dipole charges in their vicinity as a function of time. However, the orientation of the dipoles determines what the recording electrode "sees" [59]. Dipoles oriented "radially", or pointing directly outward, produce the strongest deflections in EEG because the positive or negative end of the neuron is directed normal to the electrode surface. Dipoles oriented "tangentially", or parallel to the scalp surface will contribute positive and negative charge equally to the recording electrode and will produce no deflection in the EEG data [59]. Neurons must be oriented in the same direction and activated simultaneously in order for the activity to be measured on the scalp [59].

Volume conduction is the process by which charge propagates through extracellular space from the neuron to the recording electrode on the scalp [58]. Ions of the same charge are repelled and opposite charges are attracted, forming a "wave" that propagates through each medium from the extracellular space through cerebrospinal fluid, dura layers, skull layers, and scalp to the electrode [59]. The movement of ions in these spaces is impeded by physiological barriers such as myelin-coated nerve tracts and different tissue densities [59]. One consequence of volume conduction is the spreading of electrical signals, such that a single source may be detected by more than one sensor. This effect must be particularly considered in investigations of

functional connectivity, so that significantly high levels of interaction are not falsely inferred from a common source measured by the pair of electrodes.

1.2.2 EEG in infants

The electrographic activity in pediatric subjects visually appears drastically different from healthy adult EEG. The patterns in pediatric EEG are also highly variable, creating difficulty in defining standards of healthy activity. In addition, the rapid development of the neonatal and infant brain blurs the developmental timeline. Thus, age-specific rhythms may or may not be present in perfectly healthy children at differing brain maturation states [60].

At the earliest stage of life, wakeful background activity is dominated by delta (1-4 Hz) and theta (4-7 Hz) oscillations. However by the end of the first year of life, the delta oscillations diminish, leaving predominantly theta oscillations [61]. The posterior dominant rhythm is typically not present at birth, but appears at around 3 months of age. The frequency of the posterior dominant rhythm increases over time, with its rate determined by the level of brain maturation [60]. These occipital rhythms are usually in the delta band (1-3 Hz) at 4 months of age, then theta (4-7 Hz) by around 1 year of age, and up to 8 Hz by three years of age [62]. The amplitude of the posterior dominant rhythm is higher in children than adults [63].

By 4-6 months of age, a common 5-6 Hz activity in the central regions emerges as a possible early manifestation of the mu rhythm [61]. Beta activity develops between 6 months and 2 years of age over the central and posterior regions, then migrates anteriorly with development [63]. The amplitude of beta activity is typically less than 20 μV, however, importantly for our analyses, the administration of anti-epileptic drugs such as barbituates, benzodiazepines, and chloral hydrates increase the amplitude and amount of beta activity [62].

Another common feature in pediatric EEG is generalized slowing. Similar to the posterior dominant rhythm, generalized slowing begins in lower frequencies within the first few months of life and increases in frequency with brain development [60].

During drowsiness, rhythms generally slow to 2-3 Hz and increase in amplitude. At 4-20 months of age, drowsiness elicits hypnogogic hypersynchrony: high-amplitude, synchronous 3-5 Hz waves in both hemispheres [61]. An increase in beta activity over the frontocentral regions, diffuse rhythmic theta activity, and vertex waves may all be common during deep drowsiness [62].

At the onset of sleep, neonates typically enter active sleep. Between 1-2 months, however, infants will enter quiet sleep at onset, and oscillatory activity switches from a tracé alternant pattern to a high voltage slow pattern [61]. At 3 months, infants spend about 50% of their sleep time in REM sleep, but it gradually decreases to 30% with development. The tracé alternant and high voltage slow waves begin to disappear and sleep stages become distinguishable by 6 months [61].

In stage II sleep, pediatric subjects tend to have high voltage EEG with less synchrony than adult subjects [60]. During the first year of life, sleep spindles, vertex sharp transients, and K-complexes and other features of stage II sleep are acquired [61]. Sleep spindles are 12-14 Hz runs of activity with a rectified morphology, V waves have a sharp high-amplitude negative polarity with a wide distribution, and K-complexes are sharp negative waves followed by a high amplitude longer duration positive wave [63]. Stage III and IV sleep is defined by rhythmic delta and theta frequencies as well as a decrease in the presence of sleep spindles [62]. Low voltage activity and slow alpha waves are present in REM sleep, with short bursts of saw-tooth waves [62].

1.2.3 EEG in epilepsy

Although not the definitive factor in every case, EEG most often provides strong clinical support for diagnosis in epilepsy [60]. Epileptiform patterns are distinguished from non-epileptiform sharp transients and paroxysmal waveforms by several criteria: the spikes and sharp waves are typically asymmetric, usually have more than one phase, and should be distinct from background activity [61]. Spike waveforms typically last 20-80 ms [62]. They can be focused in a given region of the brain, originate from many areas (multi-focal), or generalize across the entire brain at once. In adults, the burst of neuronal activity causing a spike will often show up in 3-4 electrodes, creating a physiologic field [62], [63]. However in infancy, it is possible to see a spike in only one electrode [63]. Approximately 6-11 cm^2 of synchronously discharging cortex is needed to be detected on scalp electrodes [62]. The spike is sharp, with a rising slope steeper than its descending slope [60]. The spike-wave complex is defined by three phases: first the spike, then a deflection below baseline, and lastly a high-amplitude, time-locked 2-3 Hz slow wave [60], [63]. The discharges can be generalized and may have polyspike-wave complexes in some cases [60]. The sharp wave is a longer paroxysmal potential, lasting 80 to 200 ms, and is slightly less sharp than a spike. The sharp wave is hypothesized to be generated by a larger neuronal network, increasing its duration while decreasing its sharpness [60]. Although thought to be less localizing of aberrant behavior than spikes, the sharp wave is strongly indicative of epileptic behavior in the EEG [60].

In focal epilepsies, wave shape, duration, and distribution differ between ictal periods, times during a seizure, and interictal periods, times between seizures. Ictal waveforms change in shape, frequency and amplitude over the course of the seizure [61]. The duration varies by the

clinical manifestation, and the distribution is wider in ictal patterns, as they begin focally and gradually diffuse [61]. Some common interictal patterns in focal epilepsies include: 3 Hz spike-and-slow wave, the sharp-and-slow wave, atypical repetitive spike-and-slow wave, polyspike-and-slow wave, and paroxysmal fast activity [62]. Ictal patterns are almost always stereotyped for individual patients, but often involve evolving repetitive sharp waves and spikes that modify in frequency, amplitude, topography and morphology over the course of the seizure [62]. In pediatric EEG, some criteria of poor prognosis, such as generalized paroxysmal fast activity, localized background flattening, continuous focal slow waves, and abnormal asymmetric background activity have been identified [62].

Generalized epileptiform patterns differ from focal activity more in the distribution than morphology of waveforms [61]. Generalized epileptiform activity is typically synchronous, has similar amplitude, and is present in corresponding parts of the hemisphere or the entire head [61]. Ictal discharges are often long repetitions of interictal patterns, an example being the "typical" 3 Hz spike-and-wave complex and the slow spike-and-wave discharge [61].

1.2.4 EEG in IS and hypsarrhythmia

EEG during the ictal periods of infantile spasms almost always include diffuse, high-amplitude slow waves [7]. Beta activity (14-30 Hz), or "fast" activity, has been associated with infantile spasms and generally superimposes on the ascending portion of the slow wave [7], [64]–[66]. Some report over ten different ictal patterns in IS, with patterns such as high-voltage slow wave, sharp wave, and voltage attenuation most commonly identified [7]. The similarity of the spasm semiology to the startle reflex, along with the electroclinical findings of fast activity

and spiking unilaterally occur, lead researchers to believe the spasms could be generated by brainstem circuits with unilateral cortical descending input [7].

The interictal EEG is more stereotyped when the spasms onset is within the first year of life [7]. *Hypsarrhythmia* is the pattern most associated with IS, and is characterized by asynchronous high-amplitude slow waves, a disorganized background, and multi-focal independent spikes [7], [11]. Hypsarrhythmia is reported to be present in approximately 70% of IS cases [10]. In NREM sleep, the EEG oscillates between lower theta-beta activity and diffuse irregular asymmetric spike-wave discharges, creating a paroxysmal alternating pattern [7]. Although it is generally a diffuse pattern, hypsarrhythmia can be lateralized, most often in symptomatic cases [7], [67]. Additionally, the multifocal spikes present in the EEG can correspond to focal cortical lesions or a region of the brain associated with comorbid partial seizures in symptomatic cases [7], [68]. There are also several variants of hypsarrhythmia, and these variants vary widely in power and spectral characteristics [10], [69].

1.3 Dissertation Roadmap

Currently, diagnosis and treatment response assessment in IS heavily rely on clinical EEG findings [9]. Clinicians *visually* assess the EEG signals for abnormal patterns and identify changes in the EEG associated with a response to therapy after treatment administration [21]. Hypsarrhythmia specifically is often used a criterion for IS diagnosis and the absence of the pattern after treatment is used as a criterion for treatment response, even if this means the EEG is still abnormal after treatment [34].

However, it has been shown that the inter-rater reliability for the identification of hypsarrhythmia is unacceptably low, with a kappa value of 0.4 among six blinded pediatric

encephalographers (Randolph's free-marginal multi-rater kappa statistic) [34]. This problem is further compounded by an inability to reach a consensus on the definition of hypsarrhythmia [70]. Several groups have attempted to objectify identification of hypsarrhythmia by developing different scoring schemes of accepted features, such as the BASED score [35], the Kramer Global Score [52], [71], and the hypsarrhythmia paroxysm index [72]. However, all of these schemes rely on visual identification of the features of the pattern, leaving subjectivity in EEG assessment. Computational EEG metrics may provide objectivity in clinical EEG assessment and improve diagnostic capabilities.

Thus, we developed computational EEG metrics that successfully discriminate between awake EEG data with and without hypsarrhythmia in a cohort of 21 IS patients. In Chapter 2, we describe how the amplitude, power spectrum, and power-law scaling can discriminate the hypsarrhythmia pattern with high accuracy.

To characterize power-law scaling in the EEG of IS subjects, we used an algorithm called Detrended Fluctuation Analysis (DFA). The output of the algorithm is a single number, the DFA exponent, that describes the strength of long-range temporal correlations in the data. This single number precludes statistical analyses over time or within single subjects. Hence, in Chapter 3, we describe a novel statistical analysis method based on the moving block bootstrap to derive confidence intervals for the DFA exponent, expanding the utility of DFA in neural data analysis.

Next, recent literature suggests that hypsarrhythmia may be less clinically useful than once believed. In fact, it was shown in the largest prospective study as of 2017 that the presence of hypsarrhythmia did not predict treatment outcome [73]. Patients that present with IS without hypsarrhythmia still exhibit extremely poor outcomes. This could partially be due to the fact that patients with IS without hypsarrhythmia are less likely to receive first-line treatment because it si

likely to be misdiagnosed [74], [75]. Additionally, definitions of response after treatment typically only require a resolution of hypsarrhythmia, although abnormal and epileptiform waveforms after treatment herald high risk for spasm relapse [76]–[79]. As such, we sought to identify biomarkers of the EEG that reflected disease burden in IS patients that were independent of the presence of hypsarrhythmia. In Chapter 4, we report our analysis of EEG from a cohort of 50 IS patients recorded at UCLA that exhibited longer lead times to treatment than most studies and had only a small fraction (8/50) of patients with hypsarrhythmia on the pre-treatment EEG.

Lastly, the consistency of EEG patterns in IS suggests common underlying functional networks associated with the disease [80], [81]. Indeed, studies with SPECT [82], PET [83], fMRI [84], and source localization [85] found that subcortical-cortical interactions may play a role in the development of IS [82] and how generalized abnormal EEG patterns are observed despite focal etiologies. In Chapter 5, we investigated functional connectivity using an algorithm based in cross-correlation and identified differences in networks patterns between IS and control subjects. We also show that these networks change over the course of a 24-period, revealing intrinsic patterns that corroborate circadian patterns in ictal onset of spasm clusters [10].

We believe these computational metrics will aid clinicians in the diagnosis and assessment of treatment in infantile spasms patients. This work meets a critical need in evaluation of IS because this patient population presents a huge burden on the healthcare system with high-risk and high-cost therapies [48], and prompt treatment initiation is imperative to maximize their overall developmental outcome [86]. We hypothesize these metrics will enable more accurate diagnoses of IS and aid in the assessment of treatment of this vulnerable patient population.

CHAPTER 2

TEMPORAL and SPECTRAL CHARACTERISTICS of the EEG with HYPSARRHYTHMIA

2.1 Amplitude and Power Spectrum in hypsarrhythmia

2.1.1 Introduction

Infantile spasms (IS) is often accompanied by a chaotic electroencephalographic (EEG) pattern known as hypsarrhythmia [8]. In contrast with the low amplitude, mixed frequency activity of normal awake EEG (Figure 2.1A), classic hypsarrhythmia is defined by multi-focal, independent epileptiform discharges on a disorganized background activity with asynchronous large amplitude slow waves (Figure 2.1B) [42]. There are also several variants of hypsarrhythmia that include episodes of voltage attenuation, burst-suppression patterns, increased interhemispheric synchronization, and hyperactive epileptiform foci [69]. Quantifying the presence and severity of hypsarrhythmia is nontrivial, as these variants exhibit drastically different power and spectral characteristics [34], [70]. For example, Hussain et al. showed that the inter-rater reliability for hypsarrhythmia identification is unacceptably low, with kappa less than 0.5 (2015). This can impede accurate diagnosis and evaluation of short-term treatment response for patients with IS. Therefore, computational measurements of hypsarrhythmia are needed to improve the accuracy, objectivity, and reliability of these assessments [34]. Improving these methods may also reduce the time between diagnosis and successful treatment, but basic characteristics have never been reported. Here, we address this gap in the literature by measuring amplitude and spectral features of EEG with hypsarrhythmia.

2.1.2 Methods

2.1.2.1 Data collection and pre-processing

Scalp EEG data was recorded from infantile spasms and control patients using Nihon-Kohden acquisition hardware and software in the Epilepsy Monitoring Unit at the Children's Hospital of Orange County (CHOC). Nineteen scalp EEG electrodes recorded neural activity, placed according to the 10-20 international electrode placement system. Data were sampled at 200 Hz or 500 Hz with electrode impedances below 5 kOhms. A clinical pediatric epileptologist at CHOC (DS) retrospectively collected the datasets from the electronic medical record and stored them in an encrypted database. Approval to perform this study was obtained from the CHOC Institutional Review Board.

We gathered EEG and clinical data for 21 infantile spasms patients. Two separate recordings were collected during wakefulness (median recording duration: 22.1, IQR 19.4-24.1 minutes). The first recording was performed at the time of the infantile spasms diagnosis prior to treatment (median age: 6.3, IQR 5.2-8.1 months), and the second was done after treatment initiation to assess response (median time to second recording: 29, IQR 19-42.25 days). The data was clipped without reviewer knowledge of treatment status or outcome. Awake EEG was chosen for analysis because EEG characteristics vary significantly across different sleep stages. The pre-treatment EEGs of all 21 patients exhibited findings consistent with hypsarrhythmia. In three patients, this pattern occurred intermittently, whereas in the other 18 it was consistently present.

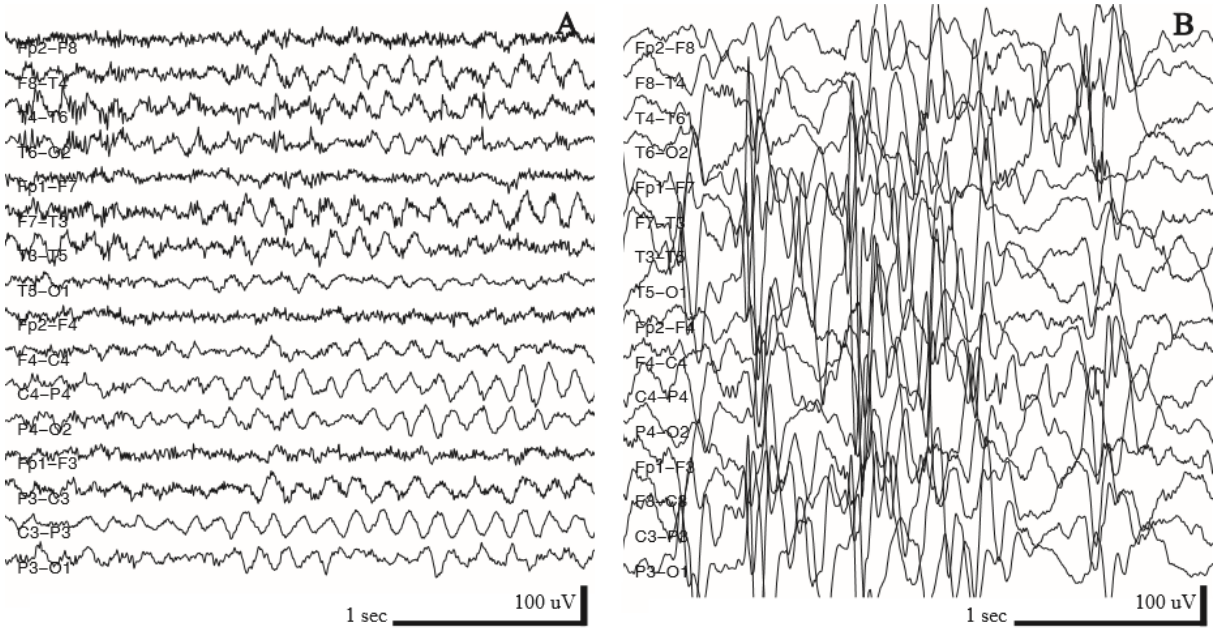

Figure 2.1 Example EEG traces. (A) Awake EEG from a control subject and (B) Awake EEG from a subject with infantile spasms and hypsarrhythmia.

We also collected data for 21 control subjects of a similar age distribution (median age: 7, IQR 5.75-11.25 months). In this group, neurologists had ordered routine EEGs for suspected neurological abnormalities due to trauma or atypical behavior, but later classified the EEG as normal. These recordings contained both sleep and awake data, and the sections of wakefulness were selected for analysis (median recording duration: 12.2, IQR 10.1-16.3 minutes). Additional exclusion criteria for control patients in this study included a history of epilepsy, abnormal developmental history, abnormal video-EEG telemetry monitoring, and known neurological conditions.

We divided the data into three groups: patient data with hypsarrhythmia (HYPS), patient data without hypsarrhythmia (NoHYPS), and control subjects (CONTROL). All pre-treatment data was classified as HYPS (n=21), as well as data from patients that had persistent

hypsarrhythmia after treatment (n=4, total HYPS n=25). Patients whose data no longer met criteria for hypsarrhythmia after treatment were classified as NoHYPS (n=17).

Data were re-referenced to a linked-ear montage. We broadband bandpass-filtered the re-referenced data using an FIR filter for the amplitude and spectral analysis (pass band: 1-55 Hz, order: 200, transitions: 0.25-1 Hz, 55-58 Hz) and then removed signal epochs marked as artifact by board-certified pediatric epileptologists at CHOC.

Table 2.1 Infantile Spasms Patient Clinical Information

Patient Number	Age at Treatment Initiation (months)	Spasms Etiology	Medication	Time between Onset of Spasms and Treatment (days)	Treatment Response	
					Hypsarrhythmia Resolved	Spasms Resolved
1	12.0	Cortical Malformation	VGB	35	No	No
4	5.5	Neonatal HIE	ACTH	7	Yes	Yes
5	8.7	Unknown, Prematurity, Diffuse Cerebral Atrophy	ACTH	4	Yes	Yes
6	6.8	Tuberous Sclerosis	VGB	4	Yes	Yes
8	4.5	Dysmorphic, likely genetic	ACTH	14	Yes	No
9	6.0	Neurofibromatosis Type I	ACTH	3	Yes	No
10	4.5	Unknown	ACTH	10	Yes	No
11	7.9	Paroxysmal Bifunctional Protein Deficiency	ACTH	7	Yes	Yes
13	3.7	GBS Ventriculitis and hydrocephalus	VGB	7	No	No
16	6.6	CDKL5 Mutation	ACTH, VGB	23	Yes	No
18	18.3	Unknown	ACTH	270	Yes	Yes
19	4.9	Neonatal HIE	ACTH	8	Yes	Yes
20	6.3	Unknown	ACTH	30	Yes	Yes
22	7.7	Unknown	ACTH	30	Yes	Yes
25	7.7	Tuberous Sclerosis	VGB	7	Yes	No
28	6.0	Chromosome 8 Abnormality & Stroke	ACTH	4	Yes	Yes
29	5.8	Lissencephaly & Pachygyria	ACTH	5	Yes	Yes
30	5.3	Lissencephaly	ACTH	90	No	No
31	19.4	Bacterial Meningoencephalitis	ACTH	90	Yes	No
32	9.0	Prematurity and Left-sided IVH	ACTH	4	Yes	Yes
34	4.9	Unknown	ACTH	28	No	No

Clinical information for 21 infantile spasms patients.
Acronyms are defined as follows: HIE = hypoxic-ischemic encephalopathy, WM = white matter, GBS = Group B streptococcus, ACTH = adrenocorticotropic hormone, and VGB = vigabatrin.

2.1.2.2 Amplitude Analysis

Amplitude values were calculated from the range of the filtered data in 1 s windows in the Cz electrode. We aggregated all amplitude values from patients within each group and constructed amplitude histograms. Statistical significance was assessed using the median amplitude value from individual patients. Electrode Cz was chosen because it is minimally affected by muscle and eye movement artifacts.

The variation of the signal amplitude across channels was visualized via topographic maps. We first constructed individual patient maps by calculating the median amplitude value in each channel from the recording. These values were normalized by dividing by the largest channel median value. The group topographic maps were constructed from the mean of the normalized patient values within each group. The figures were generated using the MATLAB-based EEGLAB function topoplot() [87].

2.1.2.3 Power Spectrum Analysis

The frequency content of the signal was analyzed with the fast Fourier Transform. We computed the magnitude of the Fourier coefficients in five second windows of continuous data and averaged over all windows in the dataset to obtain a mean power spectrum. We performed this calculation for every channel in each dataset. The median power maps for HYPS and NoHYPS groups were normalized to the median power values of the CONTROL group to reveal deviations from healthy physiological processing.

The spectral edge frequency (SEF) is defined as the frequency under which 95% of the power resides. We calculated the SEF for every channel in each patient. We compared group-wise differences by constructing topographic maps of the mean SEF from patients within each group.

2.1.3 Results

2.1.3.1 High amplitude in hypsarrhythmia

The mode of the amplitude was higher for HYPS (150-160 μV), compared to 40-50 μV for NoHYPS, and 60-70 μV for CONTROL data (Figure 2.2A). The median amplitude in the Cz electrode was significantly higher in HYPS when compared to NoHYPS and CONTROL data (Wilcoxon rank-sum test: $p<1e-6$ for NoHYPS, $p<1e-7$ for CONTROL) (Figure 2.2B). There was no difference between the median signal amplitude in the Cz electrode in NoHYPS and CONTROL data (Wilcoxon rank-sum test: $p=0.3042$).

The topographic amplitude maps were symmetric in all cases and displaced anteriorly in NoHYPS and slightly anteriorly in HYPS compared to controls (Figure 2.3). We assessed statistical significance of topographic maps with random polarity inversion permutation testing [88]. The HYPS map revealed high amplitudes were more common in the frontal and central brain regions. Channels F3, F4, Fz, C3, Cz, P3, and Pz exhibited significantly high normalized values ($p<0.05$ from bootstrapped distribution) (Figure 2.3A). NoHYPS subjects showed a consistent lower amplitude in the parietal electrodes (P3, P4 and Pz) and significantly higher amplitude in Fp1 and Fp2 (bootstrap, $p<0.05$) (Figure 2.3B). CONTROL subjects showed consistently higher values in channels Fp1, Fp2, F3, F4, Cz, and Pz (bootstrap, $p<0.05$) (Figure

2.3C). We note, however, the highest amplitudes residing in the midline may be partially artefactual due to the linked-ear reference.

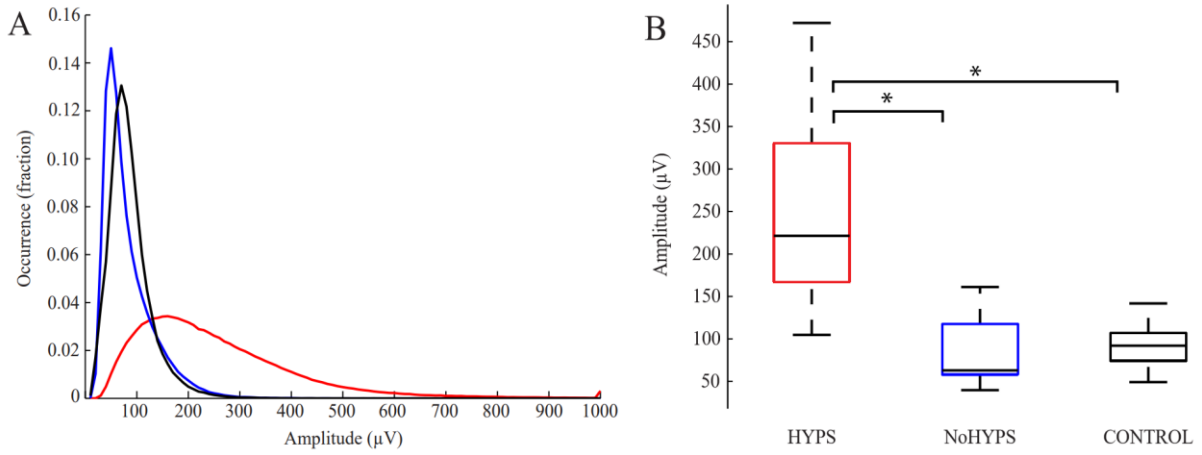

Figure 2.2 (A) Channel Cz amplitude histograms from all subjects in each group. The lines connect histogram bar centers. Red indicates HYPS, blue indicates NoHYPS and black indicates CONTROL groups. (B) The median amplitude from the Cz electrode in each group.

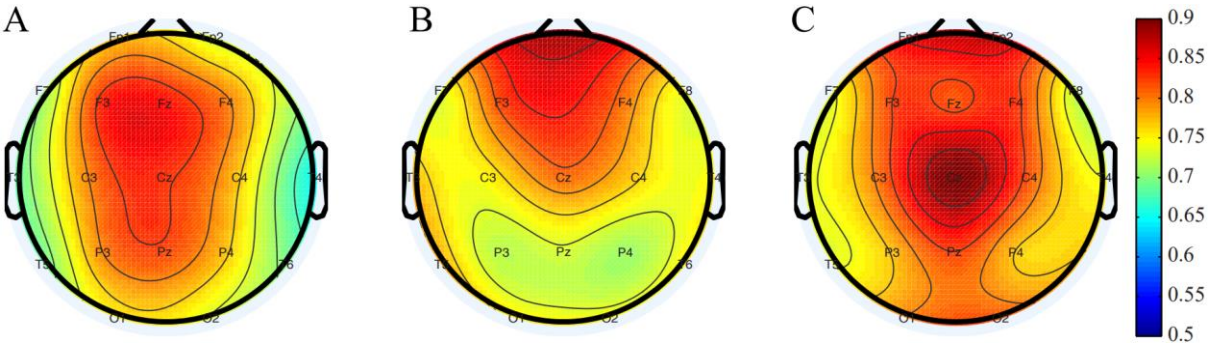

Figure 2.3 Mean topographic map of median normalized amplitude for (A) HYPS, (B) NoHYPS, and (C) CONTROL subjects.

2.1.3.2 High power in lower frequency bands in hypsarrhythmia

In HYPS, power was greater in the delta (1-3 Hz) and alpha (8-12 Hz) frequency bands when compared to CONTROL (Figure 2.4A). The power in the beta (13-30 Hz) frequency band in HYPS was similar to CONTROL data (Figure 2.4A). There was a slight suppression of activity in the theta (4-7 Hz) and low alpha frequency band in the NoHYPS data compared to CONTROL data (Figure 2.4B).

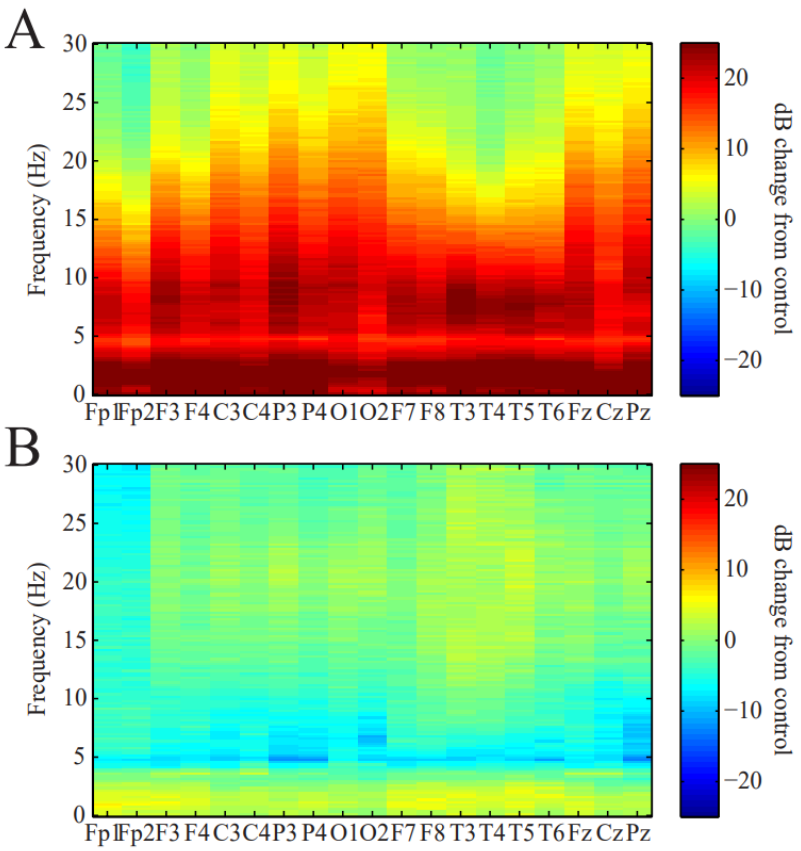

Figure 2.4 Power spectrum generated via fast Fourier Transform. Group mean power in all frequencies and all channels was normalized to the respective mean value from the CONTROL power spectra. (A) Relative differences between HYPS and CONTROL. (B) Relative differences between NoHYPS and CONTROL.

The topographical maps of the SEF in HYPS revealed that the values are consistent across EEG channels (Figure 2.5). SEF values for HYPS were statistically different from

NoHYPS in 17 of the 19 channels (all except O1 and O2, Wilcoxon rank-sum: $p<0.05$, adjusted by Benjamini-Hochberg procedure). HYPS differed from CONTROL SEF values in all channels (Wilcox. rank-sum, adjusted: $p<0.05$). NoHYPS and CONTROL SEF topographic maps revealed wide variation in SEF values across the scalp, each with very high values in the temporal channels. NoHYPS and CONTROL SEF values differed significantly only in channels Fp1 and Fp2 (Wilcox. rank-sum, adjusted: $p<0.05$).

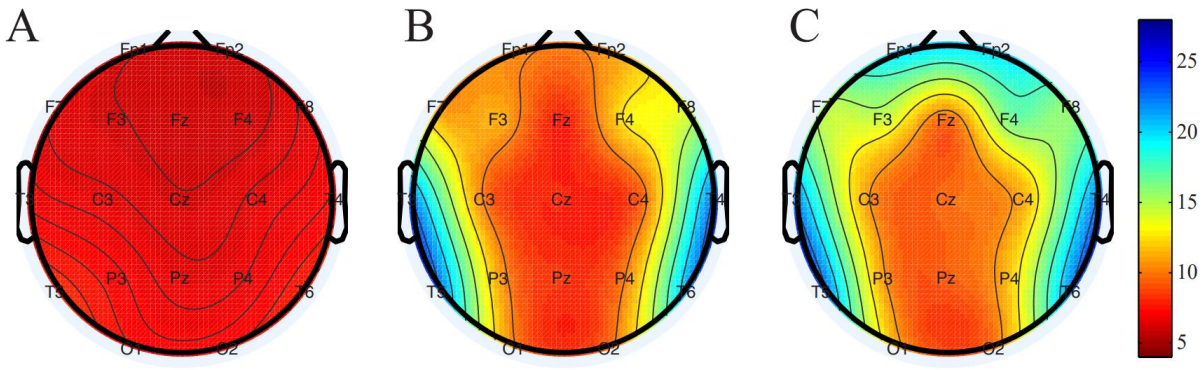

Figure 2.5 Spectral edge frequency topographic maps for (A) HYPS, (B) NoHYPS, and (C) CONTROL subjects.

2.1.4 Discussion

In this study, we quantified the amplitude and power spectrum of the hypsarrhythmia EEG pattern in IS patients.

Currently, identification of hypsarrhythmia is performed visually by clinicians based on general descriptions of the pattern. For example, hypsarrhythmia is often described as a high-amplitude (>200 μV) signal [11]. However, this definition often becomes hard to distinguish visually if the high amplitude oscillations are intermittent, when the amplitude is close to the 200 μV cutoff threshold, or if the clinician uses a different EEG reference. Attempts to objectify the

identification of hypsarrhythmia have included different scoring schemes [35], [52], [72], but these techniques still rely on visual identification of components of the pattern.

Thus, computational techniques are required, and we believe the significance of our study lies in the simplicity of the quantitative measures presented. Other groups have quantitatively described more complex characteristics of hypsarrhythmia such as the presence of multi-focal independent spikes [89], fast oscillations [65], nonlinear properties [90], neuronal network patterns [84], [85], and temporal structure [91]. Although these properties have reliably distinguished the pattern from normal control data, they require special analysis tools that are not readily available in commercial EEG systems. The simple measures we present in this study are trending algorithms frequently used in ICU monitoring systems, and thus reduce the barrier to implementation of computational EEG analysis in IS diagnosis.

One limitation of this study is that we selected and classified datasets based on the visual identification of hypsarrhythmia. We plan to mitigate the effect of human bias in future studies by implementing a scoring system [35] with multiple clinical reviewers, while conceding that complete objectivity cannot be obtained with these methods. Another limitation is that we compare patients with IS to healthy controls, and thus cannot be certain these results are specific to IS among the many types of epilepsy. To address this, we specifically plan to investigate these measures in various other forms of epilepsy, including Lennox-Gastaut syndrome (LGS), a type of pediatric epileptic encephalopathy that often develops in children with IS.

Amplitude, power spectrum, and SEF are readily available and clinically understood tools that may aid epileptologists in the identification of hypsarrhythmia in EEG data. We believe these measures, in combination with other, more complex measurements, could comprise a robust system to score and classify EEG with and without hypsarrhythmia. Because successful

treatment of IS is defined by both the cessation of spasms and the resolution of hypsarrhythmia, such a system could also enable a quantification of treatment response in these patients. This tool could have widespread impact in both industrial and clinical settings: 1) Computational measures of treatment response could minimize the number of placebo controls needed in clinical trials of novel therapies; and 2) If clinicians can assess early treatment response, they could adjust treatment methods if a particular medication is ineffective early in the treatment process. As prompt initiation of effective therapies maximizes developmental progress and reduces the chance of comorbidities in these high-risk patients, the introduction of these measures in the evaluation of IS patients may improve long-term outcomes.

2.2 Long-range temporal correlations in hypsarrhythmia

2.2.1 Introduction

As opposed to hypsarrhythmia, which is qualitatively described as a "chaotic" pattern, it is known that EEG activity in a healthy human brain possesses scale-free structure over multiple time scales [92]. Neural data has been shown to exhibit amplitude modulations on a power-law scale, in which the power in the amplitude envelope y is related to its frequency f by: $y = \frac{1}{f^{\alpha}}$, with a scaling constant α termed the Hurst parameter [92]. The power-law scaled nature of amplitude fluctuations in EEG data gives rise to long-range temporal correlations in the time series [93].

The autocorrelation is one of the simplest methods to assess long-range temporal structure in time series data. It has been used to characterize periodic phenomena in childhood absence seizures [94] and to perform automatic detection of neonatal seizures [95]. However, the autocorrelation function often provides a noisier estimate of the decay of temporal correlations than more complex methods [96]. The noise level in these calculations can be reduced by using techniques that are based on random walk theory rather than analyzing the time series directly [97]. Specifically, detrended fluctuation analysis (DFA) has been shown to be robust to certain nonstationarities in positively correlated signals, such as discontinuities due to artifact removal, and it is appropriate for use on shortened data segments [98], [99]. Both of these factors directly affect the stability of the autocorrelation. Thus, we used both the autocorrelation and DFA to characterize the long-range temporal dependence in EEG data associated with infantile spasms before and after treatment. We hypothesized that the presence of infantile spasms and

hypsarrhythmia would disrupt long-range temporal correlations in the EEG and that a response to treatment would be associated with the return of temporal correlations to normal levels.

2.2.2 Methods

2.2.2.1 Data pre-processing

The EEG data were re-referenced to a linked-ear montage and divided into narrow frequency bands using FIR filters for the delta (1-3 Hz), theta (4-7 Hz), alpha (8-12 Hz), and beta (13-30 Hz) ranges. Epileptologists at CHOC marked and removed artifacts due to eye blinks, muscle activity, movement, poor electrode contact, and periods of photic stimulation prior to analysis.

2.2.2.2 The autocorrelation function

We calculated the autocorrelation of the amplitude envelope of infantile spasms patients with and without hypsarrhythmia in the Cz electrode. The amplitude envelope was extracted from the bandpass-filtered data by applying the Hilbert transform and calculating the magnitude of the analytic signal. We then calculated the autocorrelation using a biased cross-correlation of the envelope at all possible time lags, normalized to correlation values between 0 and 1. To assess the significance of temporal correlations in the data, we compared the result of the autocorrelation to surrogate data that was created by shuffling the Fourier phases of the original envelope. We calculated the time lag at which each patient autocorrelation function failed to exceed the 95^{th} percentile of the surrogate data. This represented the time lag at which the correlations in the time series were not significantly different from chance levels.

2.2.2.3 Detrended Fluctuation Analysis

Detrended Fluctuation Analysis (DFA) was implemented using the following algorithm, adapted from Hardstone et al. (2012):

First, the amplitude envelope was extracted from each channel by similar methods used in the autocorrelation calculation. We then subtracted the mean of the amplitude envelope and computed the cumulative sum of the signal to create the signal profile. This signal profile was divided into equally-sized windows with 50% overlap. Within each window, we performed a linear fit of the signal profile, subtracted the fit from the time series, and calculated the standard deviation of the detrended signal. After computing the standard deviations of the detrended signal for all windows of that size, we recorded the median standard deviation for that window size. This process was repeated for logarithmically-spaced window sizes from 3 seconds to 25 seconds in length.

When the median standard deviations are plotted on a logarithmic scale against the log-spaced window sizes, the result is linear with slope α (Figure 2.6). This slope is a direct estimation of the Hurst parameter and indicates the strength of the temporal correlations present in the time series [99]. The slope of the resultant DFA plot varies between 0 and 1.0. Exponents less than 0.5 designate anti-correlated signals, while positively correlated signals have an exponent greater than 0.5, indicating strong long-range temporal correlations. Uncorrelated signals, such as white noise, result in a DFA exponent of 0.5.

We averaged α from all individual channels to obtain a single value approximating the strength of long-range temporal correlations in the EEG, as individual channels within a subject exhibited consistent slopes (Figure 2.6). The intercept of the DFA plot was calculated from the linear fit of the channel average by extrapolating on the logarithmic plot to find the fluctuation

value when window size was one sample, the value at which the logarithm of the window size equals zero. (Figure 2.6 filled black dot).

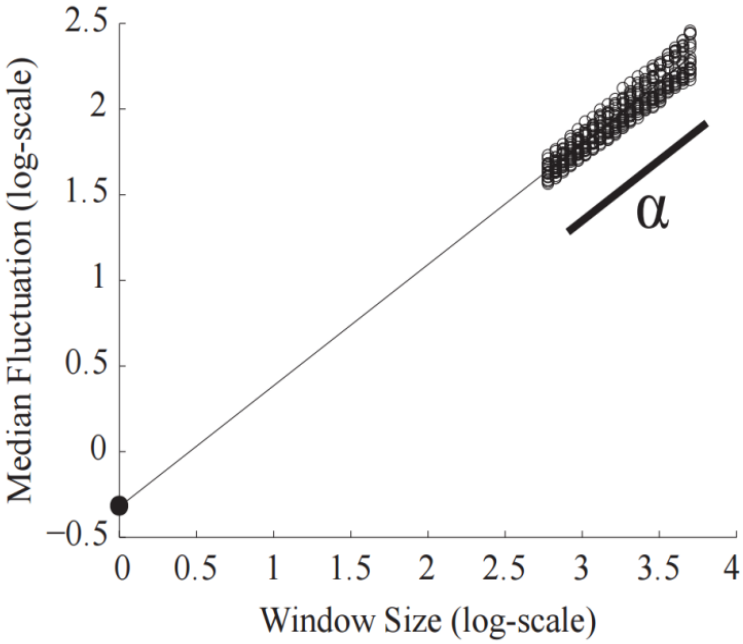

Figure 2.6 Example DFA plot. The DFA exponent, α, is the slope of the linear fit of the average of all channels. Each channel's median fluctuation value (standard deviation of the detrended signal) is plotted as a circle for each window size. Window size is measured in data points. The intercept is calculated as the theoretical fluctuation value when the logarithm of the window size equals zero, represented by the filled dot on the y-axis.

Note that DFA has been shown to robustly measure temporal dependence in positively-correlated signals, even when the data contains discontinuities due to artifact removal [98]. Although DFA has been criticized by several groups in this regard [100], [101], their concerns are often aimed at the generalizability of the technique to all signal nonstationarities. We use the method under the careful assumption that neural signals are positively correlated and we use sufficiently long window sizes to mitigate the uncertainty of the measure in small data segments. Other forms of the algorithm increase the largest window size to 1/10 of the signal length [99],

but the use of large windows can cause a piecewise linear result with one or more "cross-over" points, requiring special analysis techniques [98], [102]. Therefore, we set the smallest window size to 3 seconds and the largest window size to 25 seconds to maintain consistent linearity at all window sizes (mean SSE: 0.0017 +/- 0.0042).

2.2.2.4 Support Vector Machine Classification

To quantify our ability to distinguish between patients with and without hypsarrhythmia, we trained one-dimensional and two-dimensional support vector machines (SVM). The one-dimensional SVM imposes a simple threshold, while the two-dimensional SVM optimizes a linear classifier to separate the two groups. To train the SVM, we randomly selected half of the subjects with hypsarrhythmia (n=25) and half of the subjects without hypsarrhythmia (both spasms and control patients, n=38) and used the MATLAB function "svmtrain". We then tested the classifier with the remainder of the data using the MATLAB function "svmclassify". The number of correct classifications, the sensitivity, and specificity were recorded over 1000 iterations of randomly-selected training and testing datasets.

2.2.2.5 Effect of amplitude and standard deviation on DFA parameters

To gain insight into how basic characteristics of the EEG data, including amplitude and standard deviation, affect the DFA measurement, we performed simulations using pink noise. Pink noise was generated at 200 Hz for 20 minutes to match the characteristics of our EEG dataset. After bandpass filtering, the amplitude envelope was extracted by performing the Hilbert transform and calculating the magnitude of the analytic signal.

We then measured the DFA exponent and intercept of the simulated signal, using scaling factors to independently vary the amplitude and variance of the envelope. The 1000 scaling factors were linearly-spaced values from 1 to 100. To vary the overall amplitude, we calculated the mean value of the amplitude envelope, multiplied the mean by the scaling factor, and added this constant to the original envelope (Figure 2.7, green line). To scale the variance, we first subtracted the mean from the original amplitude envelope, multiplied the zero-mean signal by the scaling factor, and added the original mean value back into the signal (Figure 2.7, blue line). For each scaling factor, DFA was performed on all three envelopes: the original envelope, the envelope with increased amplitude, and the envelope with increased variance.

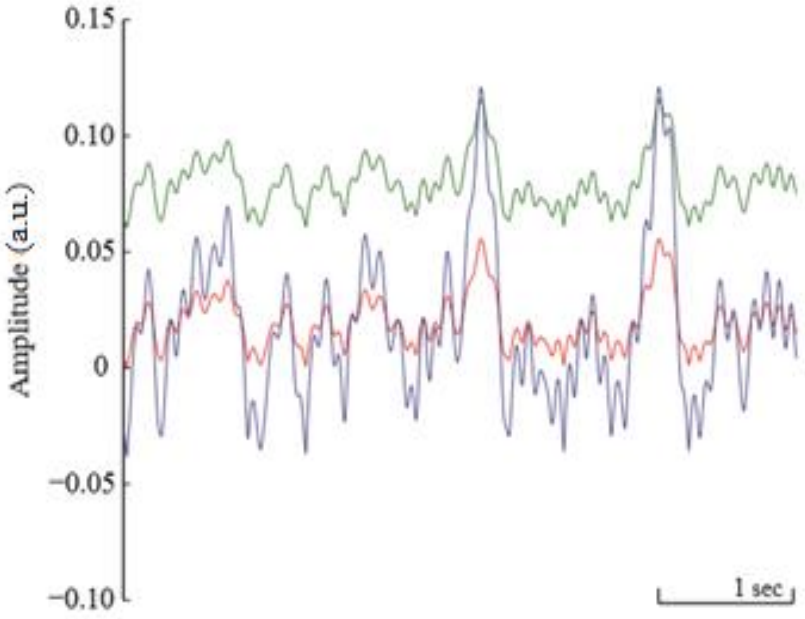

Figure 2.7 Example amplitude envelope traces used in simulated EEG filtered in the alpha band. The red line is the original extracted amplitude envelope from a simulated EEG signal. The green and blue lines depict the original envelope scaled with increased amplitude and variance, respectively.

2.2.3 Results

2.2.3.1 Hypsarrhythmia is associated with weaker long-range temporal correlations

In the beta frequency band, the EEGs of patients without hypsarrhythmia exhibited stronger autocorrelation values over all time lags when compared to data with hypsarrhythmia (Figure 2.8A). Both patient groups showed significant correlations over longer time lags than surrogate data (Figure 2.8A), but the autocorrelation of data without hypsarrhythmia remained significantly higher than surrogate data over longer time lags (Wilcoxon rank-sum: $p<0.01$, $z = -2.58$, Figure 2.8B). Results in other frequency bands were not significant (data not shown). The differences in the beta band motivated further investigation into how hypsarrhythmia disrupts temporal structure in EEG. Note, however, that we were unable to directly compare to the autocorrelation functions for the control group, as the control subject EEG data was often shorter and contained both sleep and wakeful states. The autocorrelation measurement is negatively impacted by the discontinuities created by concatenating the awake segments, and it was not possible to extract uninterrupted segments of awake data of sufficient length to directly compare the autocorrelation functions of the three groups.

Thus, further quantification and a comparison with control data warranted the use of detrended fluctuation analysis to more robustly characterize the strength of long-range temporal correlations in the data. First, we compared DFA exponents of patients with hypsarrhythmia to those without, regardless of whether the data was collected before or after treatment. Recall that some patients did not respond to treatment and still had hypsarrhythmia in the post-treatment EEG (4 out of 21 patients, see Table 2.1). Patients with hypsarrhythmia exhibited lower DFA exponents than control subjects in all frequency bands (Figure 2.9, Wilcoxon rank-sum test: $p<0.0125$ corrected for multiple comparisons, average $z = -3.74$). Patients without

hypsarrhythmia had significantly greater DFA exponents than patients with hypsarrhythmia in the theta ($p<0.0125$, $z = -3.31$), alpha ($p<0.0125$, $z = -2.92$), and beta ($p<0.0001$, $z = -3.92$) bands. There was no significant difference between patients without hypsarrhythmia and control patients in any frequency band (Figure 2.9).

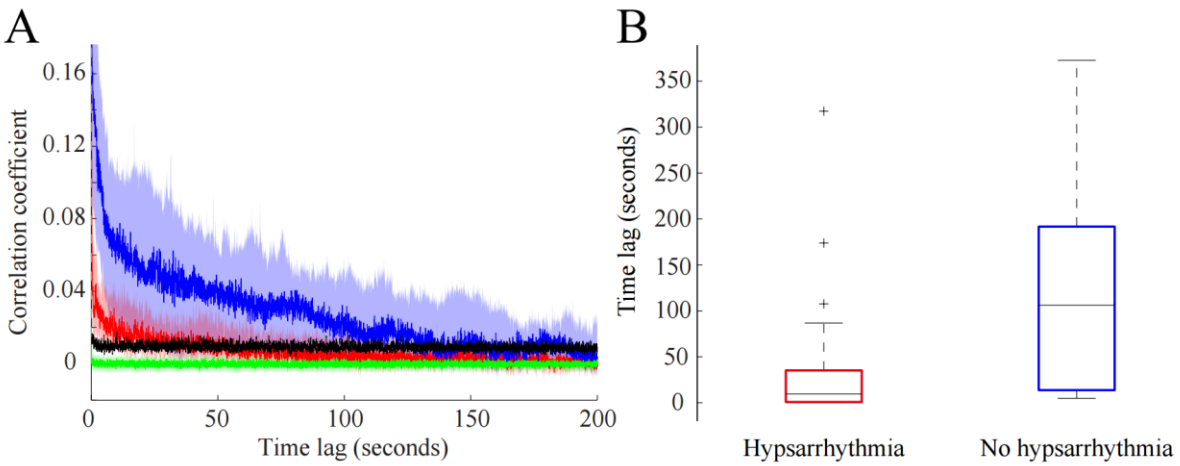

Figure 2.8 EEG data with hypsarrhythmia is associated with decreased temporal correlations in the beta frequency band when calculated with autocorrelation. (A) The median normalized autocorrelation function of the amplitude envelope in patients with hypsarrhythmia (red, n=25), patients without hypsarrhythmia (blue, n=17), and surrogate data (green, n=42). The respective shaded areas represent data between the 25th and 75th quantile of individual autocorrelation functions. The black line indicates the 95th quantile of the surrogate data used as the threshold of significance for patient data. (B) Boxplots of the distribution of lag times at which individual patient autocorrelation functions were no longer significant, for patient data with (red) and without (blue) hypsarrhythmia. Patients with intermittent hypsarrhythmia are included in the hypsarrhythmia boxplot.

2.2.3.2 DFA parameters enable classification of patients with and without hypsarrhythmia

DFA analysis results in a straight line that is characterized by both its slope (exponent) and y-intercept (Figure 2.6). The DFA exponent measures how the amplitude envelope is modulated over time, whereas the DFA intercept is a function of the standard deviation of the amplitude envelope (see Figure 2.14D). When these two quantities were plotted against one

another, we saw a separation between subjects with hypsarrhythmia (Figure 2.10, red and pink circles) and those without hypsarrhythmia (Figure 2.10, blue and black circles), regardless of treatment status (pre- or post-treatment). We note a strong negative correlation between the DFA intercept and DFA exponent in our data, despite the fact that they are derived from independent properties of the signal (Figure 2.10).

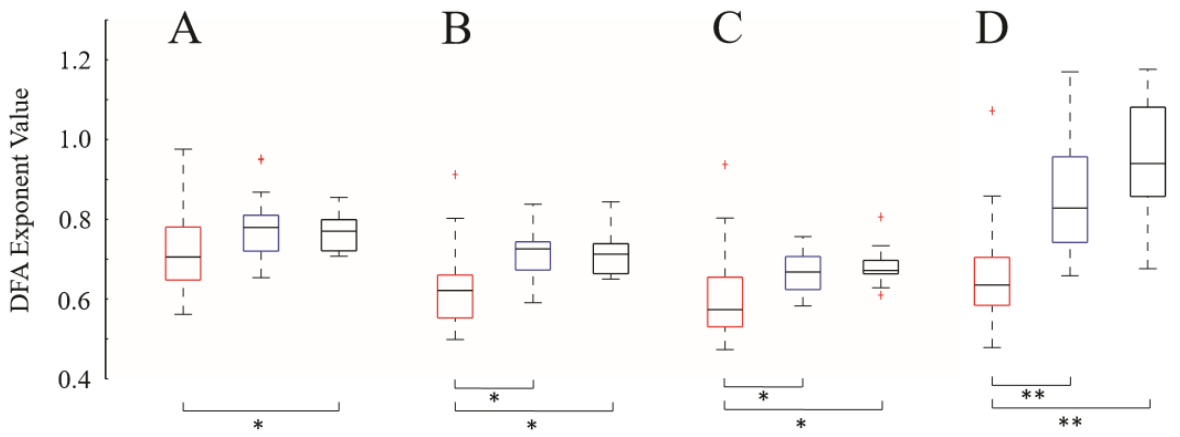

Figure 2.9 Hypsarrhythmia is associated with lower values of the DFA exponent (* = p<0.0125, ** = p<0.0001). Results are shown for (A) delta band (z = -2.54), (B) theta band (z = -3.64), (C) alpha band (z = -3.77), and (D) beta band (z = -5.03). Z-values report significance between hypsarrhythmia and controls. The red box designates hypsarrhythmia (n=25), blue indicates no hypsarrhythmia (n=17), and black represents control patients (n=21). Patients with intermittent hypsarrhythmia are included in the hypsarrhythmia boxplot.

Table 2.2 Support Vector Machine Classification of Hypsarrhythmia

Frequency Band	Classification Accuracy		Sensitivity		Specificity	
	Exponent only	Exponent and Intercept	Exponent only	Exponent and Intercept	Exponent only	Exponent and Intercept
Delta	69.1%	91.6%	62.95%	91.86%	73.77%	91.06%
Theta	77.6%	86.8%	67.52%	77.30%	85.27%	93.37%
Alpha	78.0%	88.9%	64.11%	74.27%	87.64%	98.99%
Beta	80.9%	82.9%	79.62%	75.90%	80.62%	88.24%

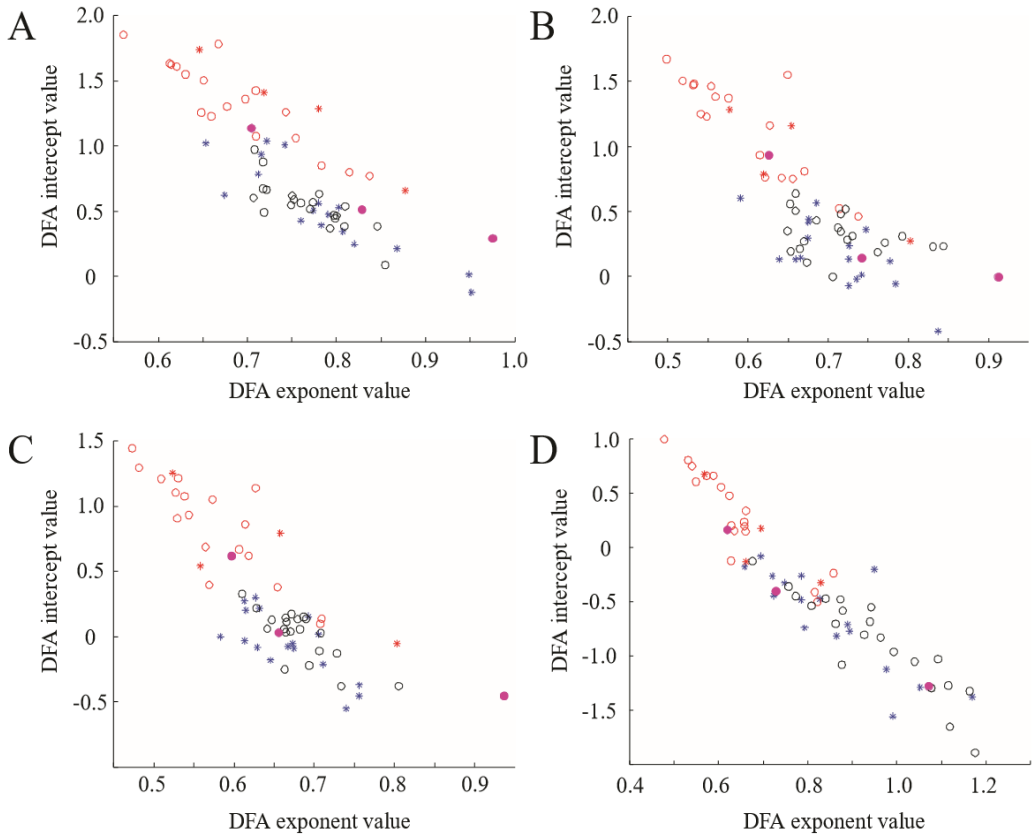

Figure 2.10 A plot of DFA exponent versus DFA intercept results in separation of patients with hypsarrhythmia from those without, enabling classification. Red open circles designate hypsarrhythmia pre-treatment and magenta closed circles indicate intermittent hypsarrhythmia pre-treatment. The red and blue stars indicate hypsarrhythmia and no hypsarrhythmia post-treatment, respectively. Black open circles represent control subjects. Results are shown for the (A) delta, (B) theta, (C) alpha, and (D) beta frequency bands.

We used a support vector machine to quantify our ability to classify patients with and without hypsarrhythmia. The SVM was trained first using only the DFA exponent as input (the one-dimensional case based on a simple threshold for the exponent), and then with both the exponent and intercept as inputs (the linear, two-dimensional case). When the data were classified using only the DFA exponent, the highest classification accuracy was 80.9%, based on the beta frequency band, with 80% sensitivity and 81% specificity (Table 2.2). When the

intercept was added as a parameter, the mean classification accuracy, sensitivity, and specificity increased an average of 11% in all categories. Using both parameters as input, we achieved a maximum classification accuracy of 92% in the delta band with 92% sensitivity and 91% specificity (Table 2.2).

2.2.3.3 The change in the DFA exponent reflects treatment response

Successful treatment of infantile spasms is defined by both a resolution of hypsarrhythmia and a cessation of clinical spasms. In our dataset, 10 of the 21 patients were classified as "non-responders" because they still exhibited clinical spasms after the administered treatment. Four of those 10 patients had persistent hypsarrhythmia following treatment.

We expected a group-wise increase in strength of long-range temporal correlations due to the resolution of hypsarrhythmia in 17 subjects (see also Figure 2.9). An analysis of pair-wise measurements in the theta and beta bands of pre- and post-treatment datasets showed that a significant number of responders exhibited an increase in strength of long-range temporal correlations after treatment (Wilcoxon left-tailed sign-rank test: $p<0.01$), whereas non-responders did not (Figure 2.11B and 2.11D).

In the beta band, responders had a greater increase in strength of long-range temporal correlations after treatment than non-responders (Figure 2.11D). The median post-treatment DFA exponent in the beta band of responders was not significantly different from the median value for the control patients (Wilcoxon rank-sum: $p=0.4509$, $z = -0.75$). However, the non-responder post-treatment median exponent was significantly lower than the control patient median exponent (Wilcoxon rank-sum: $p<0.001$, $z = -3.44$) (Figure 2.11D). Accounting for the DFA intercept induces further separation between responders and non-responders (Figure 2.12). These

results suggest that the change in the DFA exponent may reflect the clinical response to treatment, rather than just the presence or absence of hypsarrhythmia.

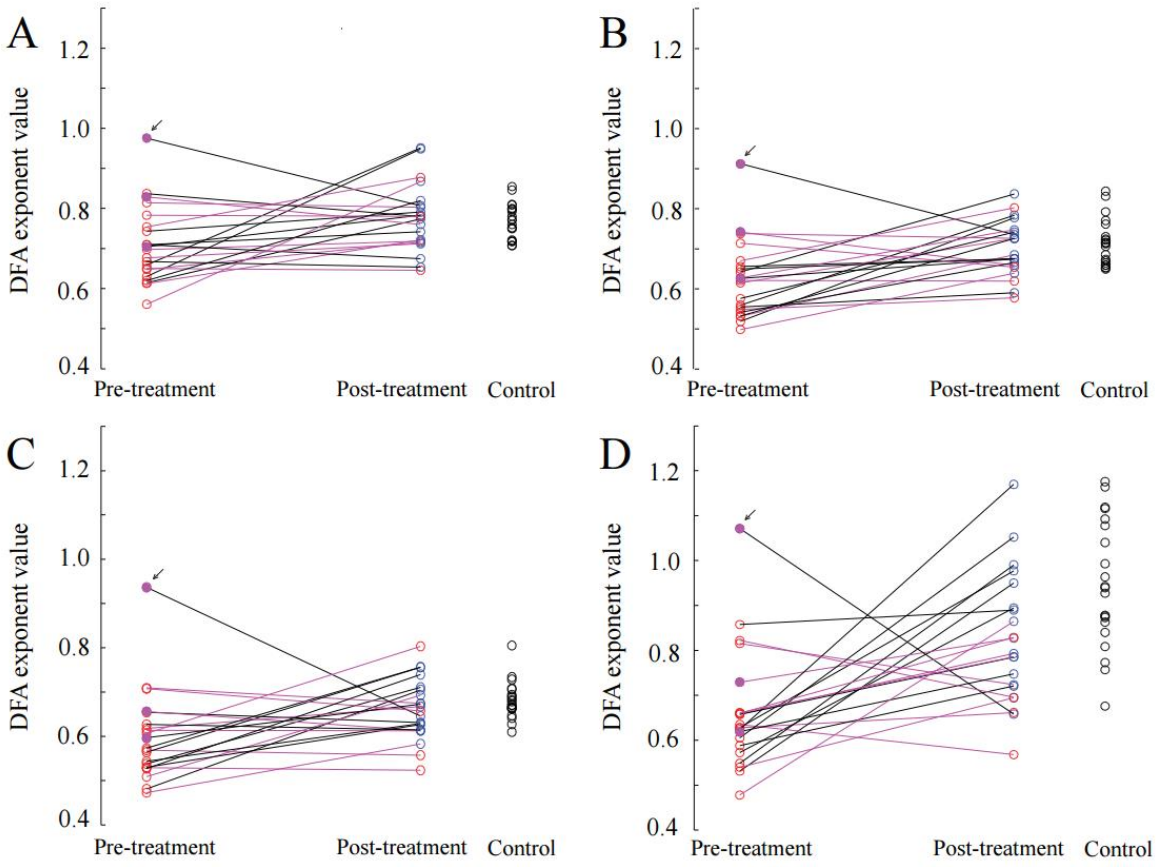

Figure 2.11 Greater increases in DFA exponent in the beta band are associated with treatment success. Data is shown for patients with hypsarrhythmia (red open circles), patients with intermittent hypsarrhythmia (magenta closed circles), patients without hypsarrhythmia (blue open circles), and control subjects (black open circles). The black lines indicate that the patient was a responder who had a resolution of hypsarrhythmia and spasms after treatment. The magenta lines represent patients that were non-responders with persistent spasms after treatment. The small black arrows indicate outlier patient 18 (see Discussion). Results are shown for the (A) delta, (B) theta, (C) alpha, and (D) beta frequency bands.

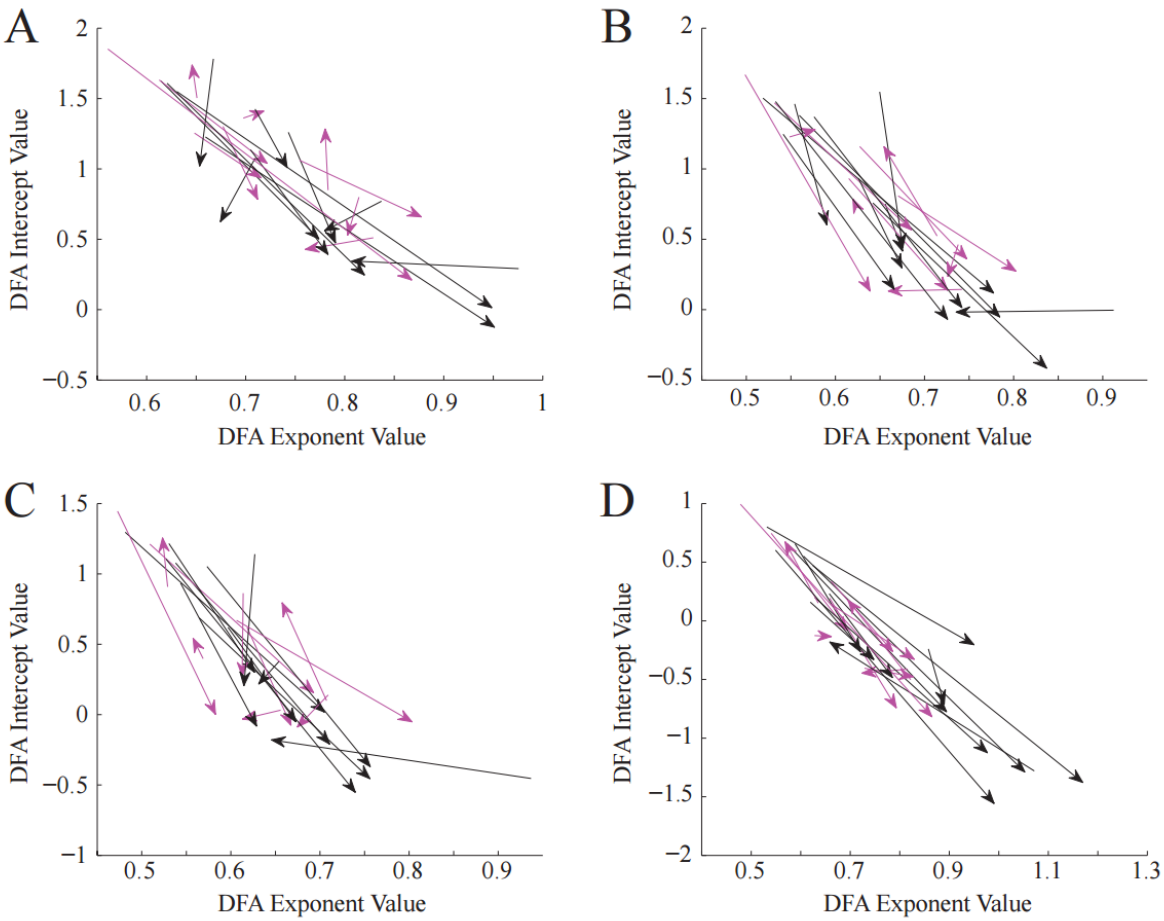

Figure 2.12 Treatment response vectors with both DFA exponent and DFA intercept as parameters. For each patient, the vector originates at the pre-treatment DFA exponent and intercept and ends at the post-treatment values. The magenta vectors represent non-responders and black vectors represent responders. Results are shown for the (A) delta band, (B) theta band, (C) alpha band, and (D) beta band.

2.2.3.4 Interpretation of DFA exponent and intercept relative to basic EEG characteristics

Because the long-range temporal correlation measurement integrates information over many time scales, it is informative to interpret the DFA parameters relative to basic characteristics of the EEG that can be visually assessed by the human eye and are used for clinical diagnosis. For example, hypsarrhythmic EEG is clinically defined as a high amplitude signal, so pre-treatment EEGs with hypsarrhythmia have a much higher amplitude than post-

treatment EEGs without hypsarrhythmia. Indeed, our calculation of amplitude histograms in patient EEGs revealed a decrease in amplitude after treatment, consistent with a resolution of hypsarrhythmia in most cases (17 out of 21 patients) (Figure 2.13). To investigate how this change in amplitude affected the analysis of temporal correlations, we performed DFA on simulated data with varying amplitude characteristics. We modulated both the overall amplitude value as well as the variance of the amplitude envelope (Figure 2.7). Our simulations confirmed that the DFA exponent is robust to variations in the amplitude of the signal (Figure 2.14A and 2.14C). The DFA intercept is also independent from the EEG amplitude (Figure 2.14B), but it exhibits a logarithmic relationship to the scaled amplitude variance (Figure 2.14D, see also Figure 2.7, blue line).

2.2.4 Discussion

In this study, we demonstrated a relationship between infantile spasms and hypsarrhythmia and the strength of long-range temporal correlations in the developing brain. Consistent with the idea that long-range temporal correlations reflect the brain's normal functional control of synchrony, we found that the strength of correlations in the EEGs of infantile spasms patients were weaker than those seen in healthy brains. Using the DFA parameters, the presence of hypsarrhythmia could be classified with up to 92% accuracy. We further found that successful treatment caused the strength of long-range temporal correlations to return to the level of control patients, with responders exhibiting a significantly greater increase in exponent values than non-responders. These results suggest that the strength of long-range

temporal correlations may not only be an indicator of hypsarrhythmia, but also reflect treatment response.

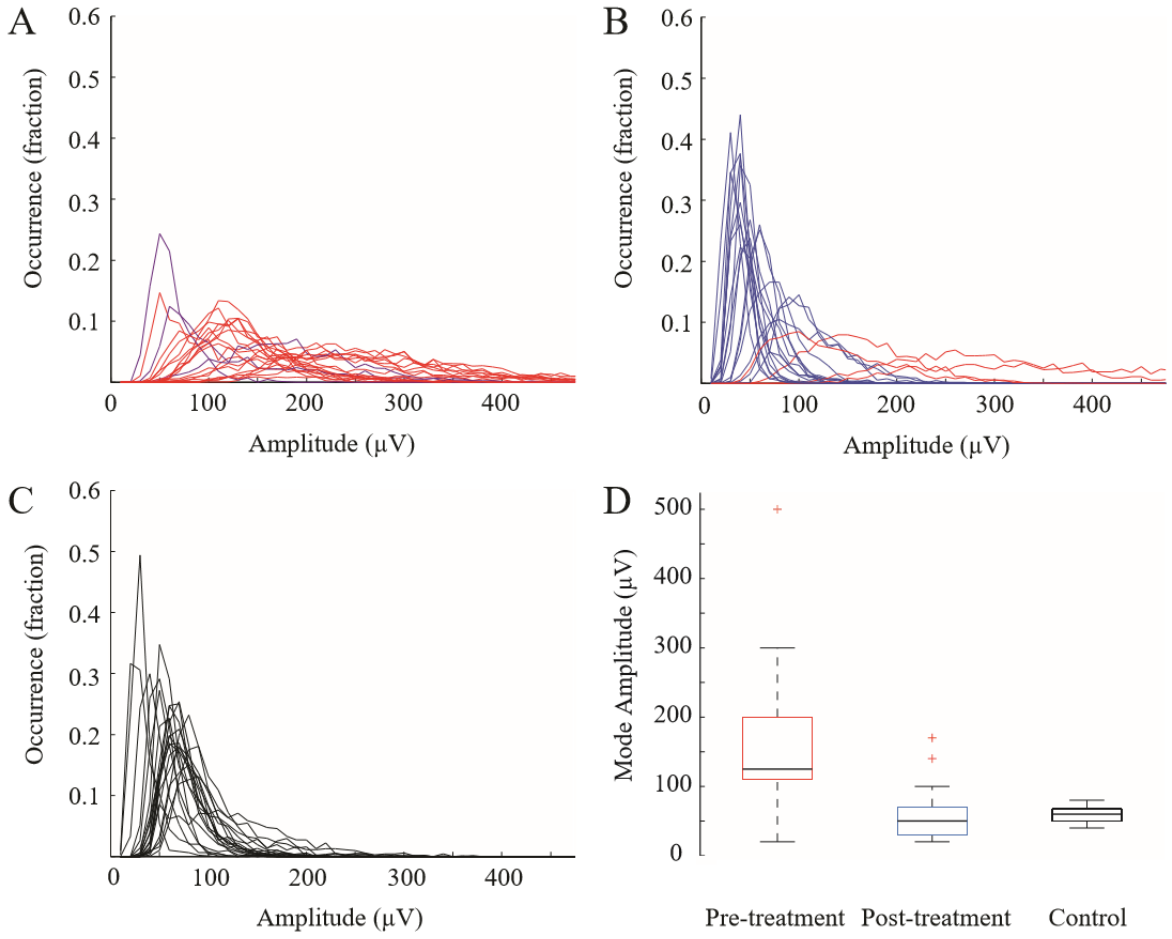

Figure 2.13 Histograms of EEG amplitude. The count in each bin is represented as a fraction of the total number of occurrences. Histograms for (A) pre-treatment, (B) post-treatment and (C) control patients. Red lines designate patients with hypsarrhythmia, magenta for patients with intermittent hypsarrhythmia, blue for patients without hypsarrhythmia, and black indicates control patients. (D) Boxplot of the mode amplitude values for all pre-treatment (red), post-treatment (blue), and control patients (black). Pre-treatment boxplot includes patients with intermittent hypsarrhythmia, and post-treatment boxplot includes patients that had persistent hypsarrhythmia and spasms after treatment.

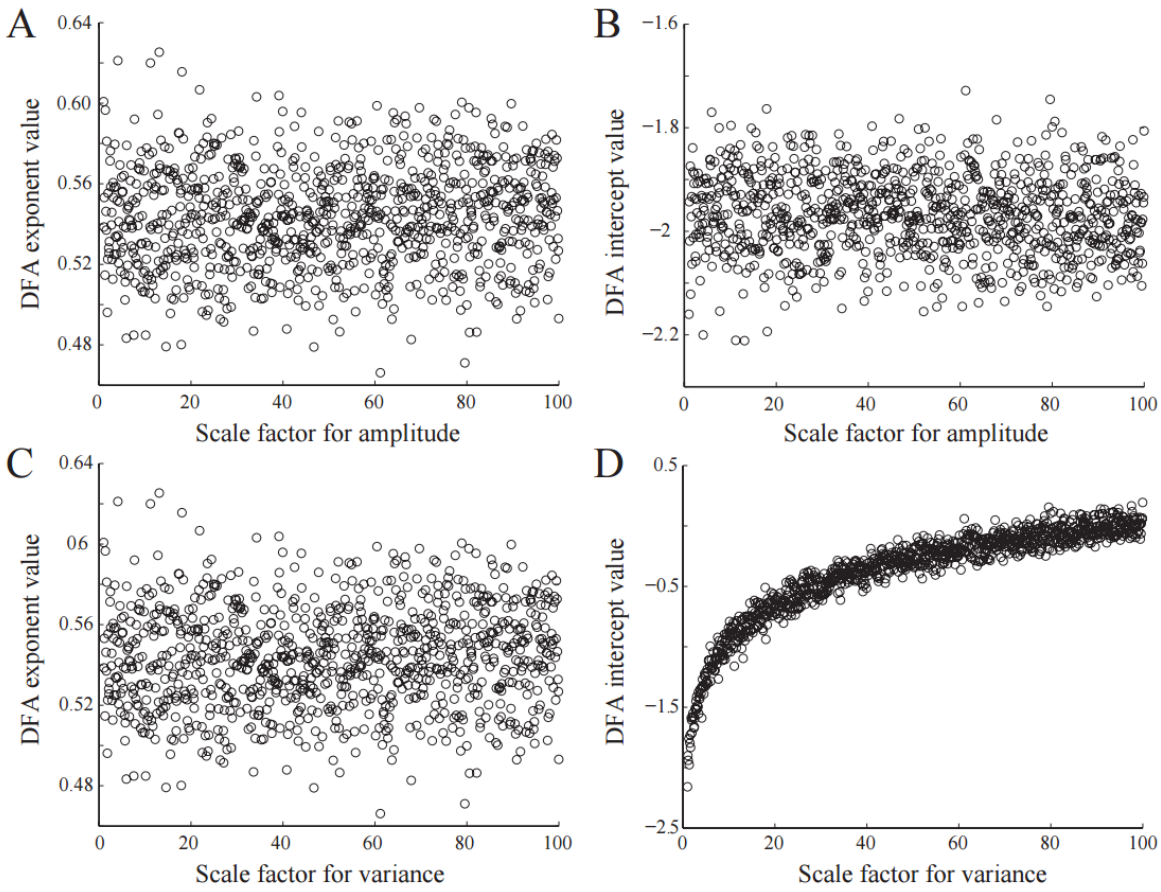

Figure 2.14 DFA results based on 1/f distributed noise filtered into the alpha band (8-12 Hz). (A) DFA exponent does not vary with increasing amplitude. (B) DFA intercept does not vary with increasing amplitude. (C)DFA exponent does not vary with increasing envelope variance. (D) DFA intercept varies logarithmically with increasing envelope variance.

Researchers and clinicians have tried to quantify various characteristics of hypsarrhythmia in an attempt to ameliorate the subjectivity of the assessment [52]. Some groups have attempted to quantitatively describe the underlying functional and neuronal network that facilitates hypsarrhythmia through EEG-fMRI [84], source analysis methods [85], and detection of fast oscillations [65]. Though the hypsarrhythmia signal is often empirically described as "chaotic," with the term describing the signal's disorganized appearance [8], the mathematical

definition of chaos and signal nonlinearity has been explored in several forms of epilepsy [90], [94], [103]. In hypsarrhythmia, an inter-ictal phenomenon, the deviation from stochastic behavior was greater than in control data, but not as nonlinear as seen during seizure periods [90]. Our results correspondingly indicate that temporal structure reliably exists in hypsarrhythmia, although it is disrupted as an effect of the disease.

DFA has been used clinically to show that the scaling properties of the EEG change when a patient experiences a stroke, enabling accurate detection of stroke by EEG in the absence of MRI [104]. In a study of epilepsy, long-range temporal correlations measured by DFA in depth electrodes and subdural EEG were shown to be stronger when in close proximity to the epileptogenic zone [105], [106]. Similar to our results, the effects of proximity to the seizure onset zone and treatment were the most prevalent in the beta frequency band [105]. However the pathogenic zone in that study showed elevated levels of long-range temporal correlations, whereas our results showed weaker correlations in the untreated, pathologic state [105]. Under the interpretation of DFA as measuring the functional self-control of the underlying network of the brain, we associated weaker temporal correlations with an inability to self-regulate the amplitude modulations necessary for healthy processing over long time scales.

The classification accuracy of infantile spasms patients in this study indicates that the strength of long-range temporal correlations measured with DFA is highly differentiable in patients with and without hypsarrhythmia. We used a support vector machine to classify patients in this study to simulate how this measure might perform if used in a clinical environment. Because the training and testing procedures used in the SVM are independent of one another, the classification accuracy indicates how well new data would be categorized in the clinic based on data from a cohort of patients from a prior study. While our dataset is quite small, the high

accuracy, sensitivity, and specificity are promising, and they support future investigation on the use of DFA in hypsarrhythmia identification for both diagnosis and treatment evaluation.

An assessment of long-range temporal correlations, by definition, analyzes longer temporal scales than typical time-frequency analyses. Because human reviewers are only able to visualize several seconds of EEG data at a time, a measure of control of the neural network over long time frames is a novel way to probe the severity of infantile spasms and hypsarrhythmia. Additionally, our quantitative measurement of long-range temporal correlations in these patients is unique in that we are assessing the ability of the neural network to regulate its own activity. The results of our simulations with pink noise indicate that DFA captures more complex characteristics of the EEG with greater clinical relevance than amplitude alone: the changes in DFA parameters after treatment are not influenced by large decreases in amplitude, but rather are secondary to alteration of the neuronal activity that underlies spasms and hypsarrhythmia.

Although there were slight increases in DFA exponents in the other frequency bands following successful treatment, the increases were most significant in the beta band. We hypothesize this may be the case for several reasons. First, studies show that high amplitude beta activity is a predominant EEG feature in healthy infants [107]. Secondly, paroxysmal fast activity (PFA) and focal or lateralized beta activity is commonly seen in infantile spasms and other epileptic syndromes [66], [108]. In addition, some of the medications prescribed for patients with IS, such as barbiturates and benzodiazepines, are often associated with an increase in beta activity [107]. Although beta activity is more prevalent in the spasms cases, the lower pre-treatment DFA exponents indicate that the activity is less correlated over long time scales. Thus, the stronger correlations seen after successful treatment may indicate that the brain has reestablished normal beta amplitude fluctuations associated with this stage of development.

There are several important limitations to the current study. Data collection was retrospective, which led to a variable amount of time between pre-treatment and post-treatment EEGs and an inability to precisely control the dataset lengths. The relatively small number of patients included in this study is an effect of the rarity of the disease and precluded comparative analysis of antiepileptic medication and etiology of spasms. Although the diverse etiology of patients is a limitation of the current study, the surprising consistency of the strength of temporal correlations across both focal and generalized etiologies promotes the use of DFA as a potential widespread diagnostic tool in this disease. Additionally, though others have reported differences in the strength of long-range temporal correlations as a function of age [96], we found no significant correlation between age and DFA exponent in the control patients in our study (Figure 2.15). We believe this is due to the narrow age distribution of the control patients (median age: 7, IQR 5.75-11.25 months). Lastly, we tested only one epileptic syndrome, so it remains unknown whether the change in the strength of long-range temporal correlations is specific to infantile spasms or is a general marker for differentiating neuropathologies from normal cortical function.

In our dataset, there were several outliers that may have impacted our results, and these correspond to some of the confounding factors known to affect successful treatment. For example, patient 18 responded to treatment, but had a much higher pre-treatment DFA exponent than post-treatment, a pattern that was different than all other responders in the dataset (see small black arrows in Figure 2.11). This patient, as well as three others, had a large time delay between spasms onset and the initiation of treatment (Table 2.1), a factor known to be associated with worse developmental outcomes [15].

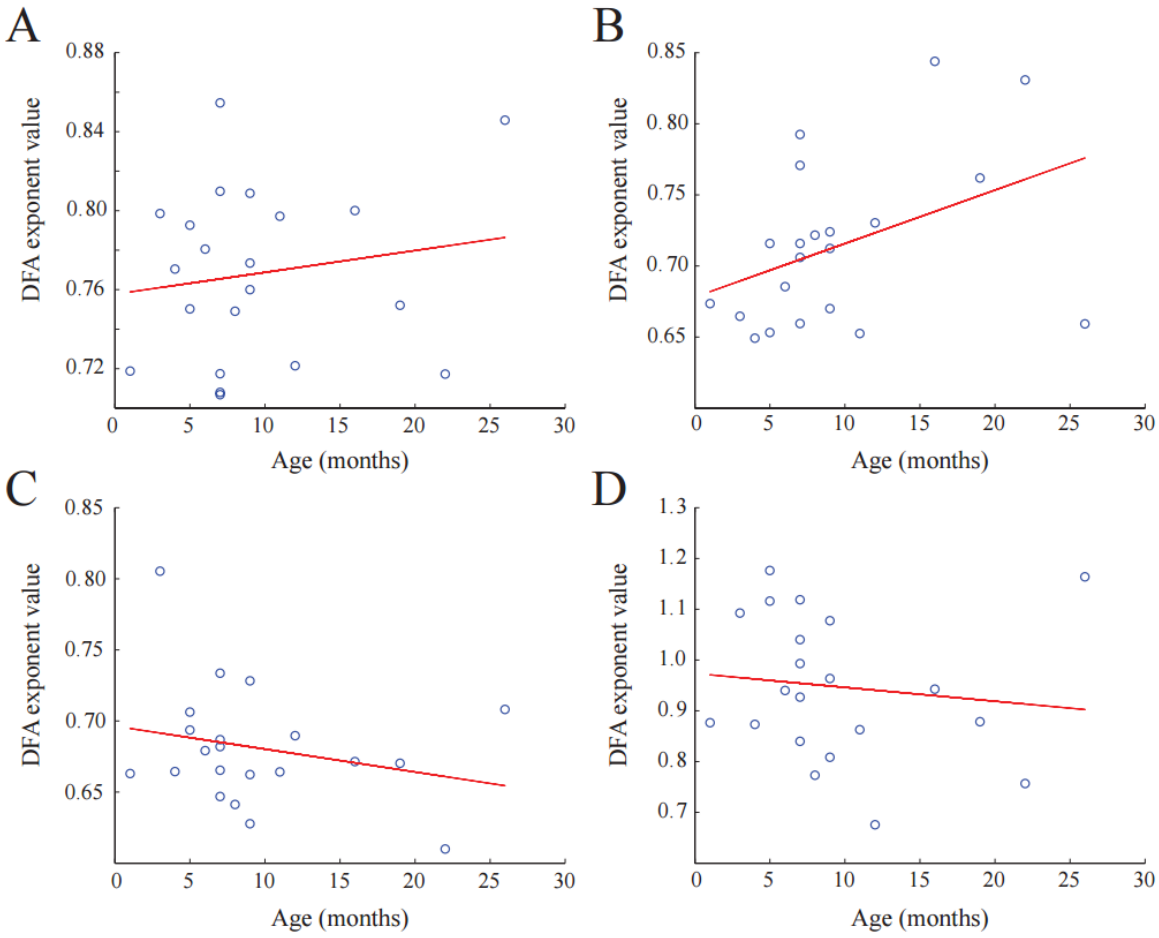

Figure 2.15 DFA exponent does not correlate with control subject age. Pearson correlations between the DFA exponent and subject age were not significant in the (A) delta band (p = 0.4911), (B) theta band (p=0.0644), (C) alpha band (p=0.2830), and (D) beta band (p=0.5971).

These limitations and gaps in knowledge necessitate further investigation into the effects of other clinical factors that confound the assessment of long-range temporal correlations in patients with infantile spasms. A prospective study with a much larger dataset will be required to assess how temporal structure is affected by factors such as therapy type and spasms etiology. As this study focused on analyzing the strength of temporal correlations in pre- and post-treatment EEG with respect to the presence of hypsarrhythmia and correlation with initial treatment

response, larger prospective studies may elucidate changes in the EEG temporal structure associated with specific epileptic encephalopathies as well as their relationship to long-term outcome.

CHAPTER 3

INFERENCE on LONG-RANGE TEMPORAL CORRELATIONS in HUMAN EEG DATA

3.1 Introduction

The strength of long-range temporal correlations in time series can be estimated by Detrended Fluctuation Analysis (DFA), a statistical method based on scaled windowed variance [109]. Although the technique originated to assess patterns in DNA structure [110], the utility of DFA has expanded to probe temporal structure in other physical systems such as daily temperature fluctuations [111], gait stride intervals [112], and heart rate variability [113]. Since the discovery of long-range temporal correlations in recordings from the human brain [92], neurophysiologists and clinicians have used DFA to analyze the temporal structure in neural data associated with sensorimotor function [114], [115], cognitive development [96], [116], [117], neurologic disease [91], [105], [106], brain stimulation [118], [119], and brain trauma [104], [120], [121].

DFA is one of several algorithms that statistically estimates the Hurst exponent (H), a scalar value that reflects the level of self-similarity in time series [122]–[125]. The measure directly relates to the rate of decay of the autocorrelation function (Figure 3.1) [94], [95]. When DFA is applied to a single segment of time series data, it returns one estimate of the Hurst exponent. Thus, in the context of studies with neural data, conclusions are often based on distributions of single DFA exponent values from groups of subjects [92], [96], [126]. This precludes within-subject comparisons between different conditions and statistical analysis of

changes in the DFA exponent over time. In this study, we present a statistically rigorous method to estimate the confidence interval for the DFA exponent of human EEG data. This technique enables us to track long-term EEG temporal structure changes in an infant and to compare treatment responses in subjects diagnosed with epilepsy.

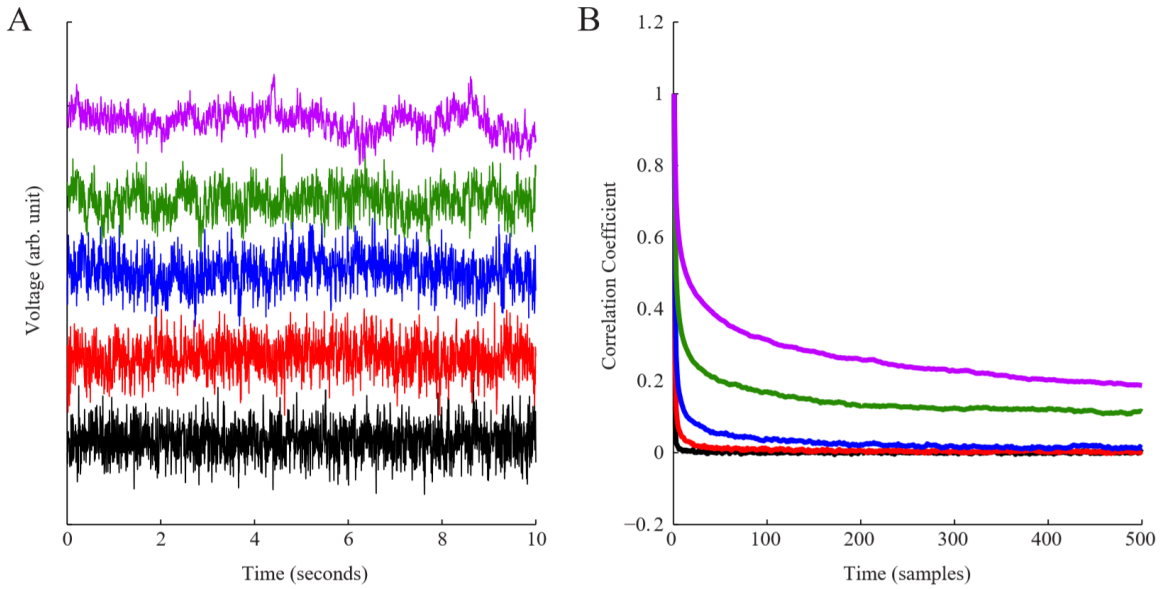

Figure 3.1 Relationship between simulated EEG time series and the signal autocorrelation. (A) Raw simulated EEG time series generated with H=0.55 (black), 0.65 (red), 0.75 (blue), 0.85 (green), and 0.95 (magenta). We highlight that the time series display larger migrations from the mean in more positively correlated signals. (B) Normalized autocorrelation of each time series.

Our method of statistical inference for DFA applied to neural data is based on the moving block bootstrap (MBB) [127], [128]. Bootstrapping and other Monte Carlo methods generate independently sampled data with similar statistics as the original signal. The MBB is a bootstrapping-based procedure that is applicable to signals with temporal autocorrelation (such as neural time series data) [129]. Using MBB we generate distributions of estimates of the Hurst exponent by randomly sampling from blocks of a time series (rather than singleton points, as in a classical bootstrapping technique), concatenating the blocks, and computing the test statistic over

the new time series [128]. This preserves the dependence structure of the time series [127]. Although MBB has been used to generate empirical distributions of DFA exponents in simulated and financial returns time series [130], the challenge of bootstrapping EEG data for analysis with DFA has not been addressed. The extension to brain signals, in particular EEG, is not trivial because of the nonstationary and nonlinear nature of the signals, the continuous transition of brain states, and the presence of artifacts in the data [131]–[134]. We show first through simulation that MBB can uncover statistically significant changes in the strength of long-range temporal correlations, and we discuss practical considerations for implementation such as the effect of varying epoch length and the introduction of discontinuities through bootstrapping and artifact rejection. We then show how these methods can be used in long-term EEG analyses to assess changes in brain state and in assessing response to treatment in subjects diagnosed with epilepsy.

3.2 Methods

3.2.1 Simulated Data Generation

We used simulated data to show performance of the DFA algorithm under various conditions that are common in neural time series processing and MBB. Simulated fractional Brownian motion (fBm) was created by integrating fractional Gaussian noise (fGn) that was generated with a given Hurst exponent (H) [135]. We used the contributed MATLAB function "ffgn" [136] to create a temporally correlated signal with H ranging from 0.50 to 0.99. The function generated exact paths of fractional Gaussian noise by means of circulant embedding for positively correlated signals ($0.5<H<1.0$) [137]. The number of data points in the generated

signal corresponded to the number of samples in twenty minutes of EEG data at a sampling rate of 200 Hz to approximately match standard clinical data collected from human subjects.

3.2.2 EEG Recording and Pre-processing

We retrospectively analyzed three human EEG datasets from infant subjects enrolled in two different studies at the Children's Hospital of Orange County (CHOC) to assess the utility of MBB and DFA. Both of these studies investigated a seizure type known as infantile spasms. These studies were approved by the CHOC Institutional Review Board.

In the first dataset, a board-certified pediatric epileptologist (DS) retrospectively identified 20-30 minute scalp EEG recordings from 21 normal infants aged 4-19 months (median 6.3 months). All 21 recordings were ultimately classified as normal. This dataset was used to demonstrate the methods and parameter choices for MBB-DFA (see Sections 3.2.4, 3.2.5, 3.3.2, and 3.3.3). We will refer to this dataset as the Control dataset.

The second dataset was comprised of a long-term (>24 hour) video-EEG recording of a 7-month old otherwise normal infant who was having events suspected to be seizures. This recording was also ultimately classified as normal by the same epileptologist (DS). We selected a data segment that included 126 minutes of wakefulness and 166 minutes of sleep, without regard to specific sleep stages. (See Sections 3.2.6 and 3.3.5). We will refer to this dataset as the Long-Term dataset.

Lastly, the third dataset consisted of recordings from two infants who were diagnosed with infantile spasms. These subjects were chosen to demonstrate changes in the DFA exponent distributions after treatment. Subject A was a 5.5-month-old infant whose epilepsy was treated successfully with adrenocorticotropic hormone (ACTH), a common therapy for the disease. We

selected 24.3 and 21.2 minutes of awake data from the pre-treatment and post-treatment recordings of this subject, respectively. The clipped segments were chosen because they were relatively free of artifacts. Successful treatment was defined as a cessation of seizures and resolution of an epileptiform EEG pattern known as hypsarrhythmia [70], [138]. Subject B was a 3.7-month-old infant who was treated unsuccessfully with vigabatrin, exhibiting persistent spasms and hypsarrhythmia after treatment initiation. This subject's pre- and post-treatment EEG included 20.4 and 23.4 minutes of awake data, respectively. We will call this two-subject dataset the IS Subject dataset.

All recordings consisted of nineteen scalp electrodes placed according to the international 10-20 system, sampled at 200 Hz with impedances below 5 kΩ. The same board certified epileptologist (DS) viewed the broadband bandpass-filtered data according to the clinical standard (1.0-40 Hz). Start and end times of high-amplitude muscle activity, eye blinks, subject movement, poor electrode contact, impedance checks, and photic stimulation were marked. We note that the visually marked artifactual time periods included a buffer on either side of the artifact to account for any signal spread due to the filtering done prior to removal. EEG data were re-referenced to a linked-ear montage and divided into narrow frequency bands using FIR filters for the delta (1-4 Hz, order = 400), theta (4-7 Hz, order = 100), alpha (8-12 Hz, order = 50), and beta (14-30 Hz, order = 29) frequency bands (Figure 3.2). After the data was filtered into the frequency band of interest, the time periods marked as artifact were removed from all channels. This procedure was followed whenever artifacts were removed from the data. Note that for some analyses (Section 3.2.4 and 3.2.5), some or all of the artifacts were purposely left in the data.

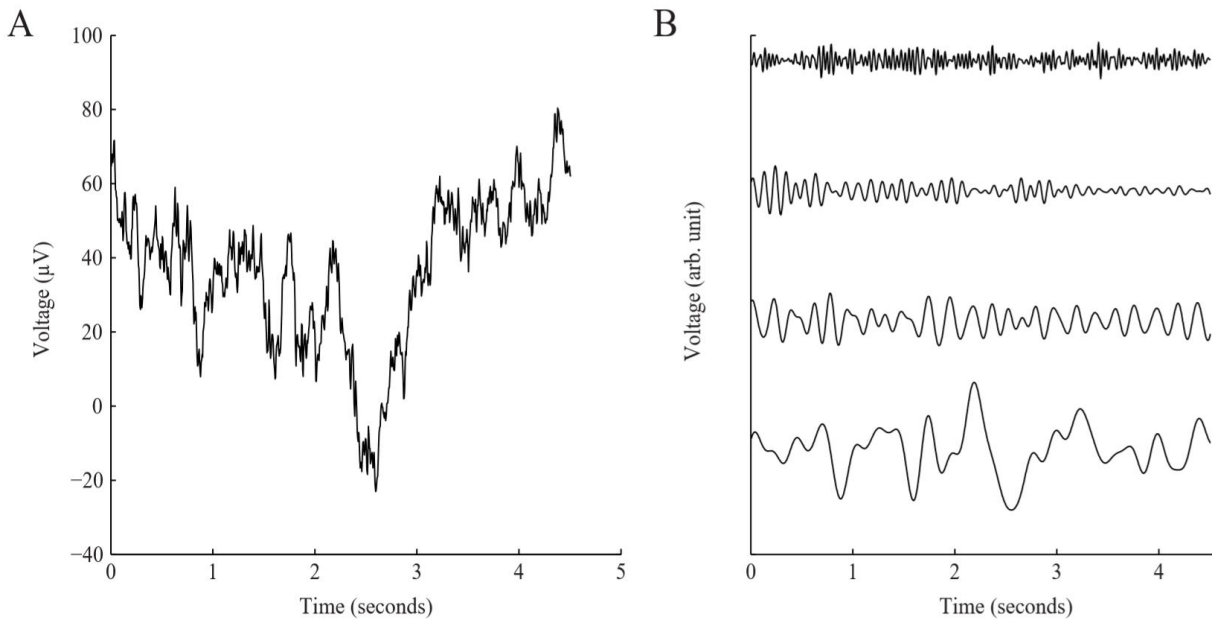

Figure 3.2 The effect of filtering on scalp EEG time series. (A) Raw scalp EEG time series from control subject. (B) EEG data filtered into the delta (1-4 Hz), theta (4-7 Hz), alpha (8-12 Hz), and beta (13-30 Hz) frequency bands, from bottom to top, respectively.

3.2.3 Detrended Fluctuation Analysis

Detrended Fluctuation Analysis was applied to both simulated and human scalp EEG data. We repeat the algorithm here for completeness; all steps are as originally described in Peng et al. and Hardstone et al. (and in Section 2.2.3.2 of this dissertation) except where indicated [99], [110]:

We define $\{y(t)\}$ to be the EEG time series with zero mean, and $\{h(t)\}$ to be the Hilbert transform of $\{y(t)\}$ where

$h(t) = \frac{1}{\pi}\, p.v. \int_{-\infty}^{\infty} \frac{y(\tau)}{t-\tau} d\tau.$ (1)

The magnitude of the Hilbert transform is

$x(t) = \|h(t)\|,$ (2)

representing the amplitude envelope. We define $\bar{x}$ to be the average $\frac{1}{k}\sum_{i=1}^{k} x(i)$ where k is the number of samples in the time series. The signal profile at time t is the integrated zero-mean envelope

$$u(t) = \sum_{i=1}^{t}[x(i) - \bar{x}]. \qquad (3)$$

Note that in the simulated data, the mean is subtracted from the fractional Gaussian noise and then integrated over time.

The signal profile $\{u(t)\}$ is divided into equally-sized windows with 50% overlap [99] (Figure 3.3A). We define the q^{th} window of size M to be the signal profile at time points $t_q + 1, t_q + 2, \ldots t_q + M$. In this window, u^q can be represented by a linear model $u^q(t) = \beta_0^q + \beta_1^q t$ where $t = t_q + 1, \ldots t_q + M$, where the estimates of the regression parameters denoted by $\hat{\beta}_0^q$ and $\hat{\beta}_1^q$ are obtained by the ordinary least squares criterion. The estimated trend is removed to form the residuals

$$R^q(t) = u^q(t) - \left[\hat{\beta}_0^q + \hat{\beta}_1^q t\right], \qquad (4)$$

for $t = t_q + 1, \ldots t_q + M$. One may estimate nonlinear trends in time t and hence the residual will be $u^q(t)$ minus the estimated nonlinear trend.

The standard deviation of $\{R^q(t)\}$ is computed for the q^{th} window of length M to be

$$SD_M(q) = \sqrt{\frac{\sum_{t=t_q+1}^{t_q+M}(R^q(t) - \bar{R}^q)^2}{M-1}} \qquad (5)$$

where $\bar{R}^q = \frac{1}{M}\sum_{t=t_q+1}^{t_q+M} R^q(t)$. Note that $\bar{R}^q$ theoretically equals zero because the intercept $\hat{\beta}_0^q$ is included in the linear model. For windows of size M, we denote the total number of windows to

be Q_M. The median of the standard deviations across all windows $q = 1, \dots, Q_M$ is computed to be $\overline{SD}_M = median_{q=1,\dots,Q_M}\{SD_M(q)\}$.

This process is performed for twenty logarithmically-spaced (base 10) window sizes $M =$ 1 second (200 samples) to $M = (\frac{1}{10} signal\ length)$. The slope of the scatterplot for $\log\{\overline{SD}_M\}$ as a function of $\log(M)$ is estimated using least squares (Figure 3.4). This sample slope is the DFA exponent, denoted α, and it serves as a direct estimate of the Hurst exponent (H).

Because DFA will return an exponent value even when the resultant loglog plot is not linear, we ensured the data was best described by a linear model using the model selection technique outlined in [139].

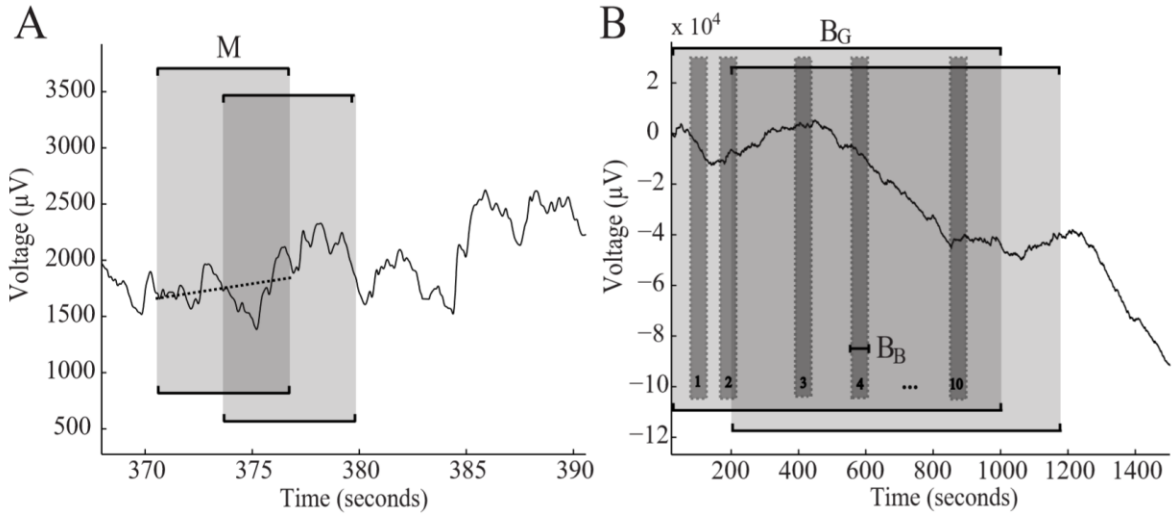

Figure 3.3 The signal profile (cumulative sum of the time series) divided into windows. (A) Windows used in DFA are of length M with 50% overlap. Within each window, the linear trend is removed (dotted line) and the standard deviation of the detrended signal is obtained. (B) Blocks of data describing the moving block bootstrap and analysis of long-term EEG recordings. The length of the bootstrap block is B_B (50 seconds) and the length of the global window is B_G (1000 seconds). Ten windows of length B_B are randomly sampled from a global window of length B_G to create block-bootstrapped time series. Global windows were shifted 200 seconds (after artifact removal) in the long-term recordings.

3.2.4 Signal Length Analysis

To conduct rigorous statistical analysis, it is necessary to quantify the uncertainty of α, which is the point estimate for H. To estimate the variation in the DFA exponent α when analyzing time series of different lengths, we examined the difference between α measured for a short window of data and α measured for the entire signal length. We simulated time series that were at least 2.4×10^5 samples in total, the equivalent of twenty minutes of data sampled at 200 Hz. We performed DFA on the entire signal length and labeled this value as the "true" DFA exponent ($\hat{\alpha}$). The signal was then divided into non-overlapping windows of one minute of data (1.2×10^4 samples), and the DFA exponent was calculated for each one-minute segment (α). We recorded the difference between α and $\hat{\alpha}$. This process was repeated for windows increasing in size by one minute up to ten minutes.

To demonstrate this effect in human EEG data, we analyzed the sleeping portions of the Control dataset before artifact removal. The artifacts were left in the data to minimize the number of discontinuities in the signal. The analysis included patients from this dataset whose sleeping portions of data exceeded 14 minutes in length (n=10 subjects). The iterative process described for simulated data was repeated for these data. The DFA exponent calculated for the entire EEG time series was labeled α_{full} and the exponents for the shorter segments (α) were compared with the α_{full} value.

3.2.5 The Effect of Discontinuities and Artifacts

Employing a moving block bootstrap will introduce discontinuities into the data because the process concatenates randomly sampled blocks of time series data (Figure 3.3, B_B) [127],

[140], [141]. We wanted to quantify the effect of discontinuities on the estimate of H using DFA. This question was also investigated by [98], but the study did not quantify the effect of discontinuities on the variance of the distribution of DFA exponents obtained. One of our main goals in this paper is to study this effect. To do this, we first generated simulated time series as before, effectively twenty minutes in length. The DFA exponent was calculated for this original signal ($\hat{\alpha}$). Discontinuities were introduced by randomly selecting one 50-second block of data from the time series, removing it from its original location, and adding it to the end of the time series, creating two discontinuities with one window translation. We chose a block length of 50 seconds to match the bootstrapping block length (B_B, Figure 3.3). This process was repeated for ten iterations of block translations. We measured the DFA exponent (α) for the new time series with each iteration and recorded the difference between α and $\hat{\alpha}$. The windows were sampled without replacement from the original signal, creating a total of twenty discontinuities in the new time series compared to the original.

We performed this test on the Control dataset. We recorded the difference between the DFA exponent measured for the original time series (α_{full}) and the exponent measured with each window translation (α). We analyzed patients from this dataset with at least 500 seconds of continuous EEG during wakefulness (n=13 subjects).

In addition to discontinuities introduced by the bootstrapping procedure, discontinuities also arise due to the removal of artifacts. This is a common and often necessary practice in analyzing human EEG data. To test the effect of artifact removal on the estimate of H, we first bandpass-filtered the data and removed all artifacts. We then measured the DFA exponent for each electrode in the Control dataset (α_{full_clean}). We compared this value to the DFA exponents

measured in bandpass-filtered data with a percentage of artifact time periods removed randomly (α). We chose different subsets of artifacts for twenty iterations, resulting in a distribution of α values for each percentage of artifacts removed. This process was repeated in increments of 10% of artifact time periods removed in all waking portions of the 21 subjects in all channels.

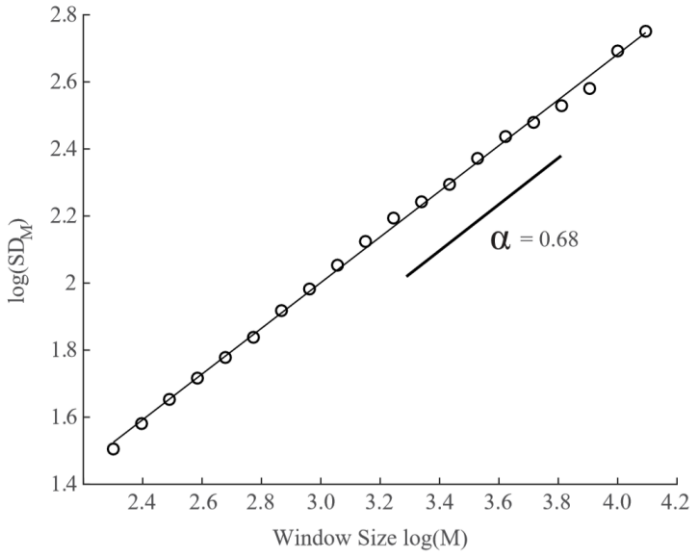

Figure 3.4 Example output of detrended fluctuation analysis (DFA). When the log of the median fluctuation (the standard deviation of the detrended signal profile) is plotted as a function of the log of the window size, a linear result may indicate power-law scaling in the time series. The slope of the line (α) is an estimate of H for the time series.

3.2.6 Bootstrap Analysis

We employed MBB-DFA by concatenating randomly selected blocks of data from the time series [127], [128], [140]. This method preserves the dependence structure in the time series by concatenating blocks of sufficient length to maintain correlation on a shorter time scale [141]. We built a bootstrap distribution to compare to the original α value in simulated data as follows. First, we calculated the DFA exponent for the original time series ($\hat{\alpha}$). Ten windows, each 50-seconds (1.0×10^4 samples) in length (B_B, Figure 3.3B), were randomly selected out of the 24

possible windows and concatenated to create a new time series that was 500 seconds long. DFA was performed on the new time series and the exponent (α) was calculated for 500 realizations. We then applied MBB to the Long-Term and IS Subject datasets. All recordings in these datasets exceeded 1000 seconds in length (twenty 50-second windows) (Figure 3.3B).

The DFA exponent and its confidence intervals were tracked over time in the Long-Term dataset. The time series was segmented into 79 overlapping windows, which were defined as "global" windows. Each global window of data was individually bootstrapped to calculate the distribution of DFA exponents (α) for that window. The global windows were 1000 seconds in length (B_G, Figure 3.3B), approximately matching the length of the bootstrapping simulations, and shifted with 80% overlap (shift=200 seconds, after artifact removal). In each global window, we randomly extracted ten 50-second segments of data (B_B, Figure 3.3B) and concatenated the segments to make a new 500-second signal as described above. We analyzed this signal with DFA, recorded α, and repeated this process to create a distribution of 500 values. The empirical distributions were obtained for all 79 global windows.

3.3 Results

3.3.1 Variance of DFA exponents in simulated data

We first measured the variation in the DFA algorithm output by generating simulated data with a known Hurst exponent (H) and recording the estimates of H, represented by the DFA exponent (α) over 500 realizations. The mean of the distribution of α values was very similar to the true exponent H used to simulate the data (Figure 3.5). The maximum standard deviation of the distributions was 0.024. Thus, the proposed estimator is approximately unbiased for the true

exponent H. Histograms of selected distributions showed little deviation from normality (Figure 3.5).

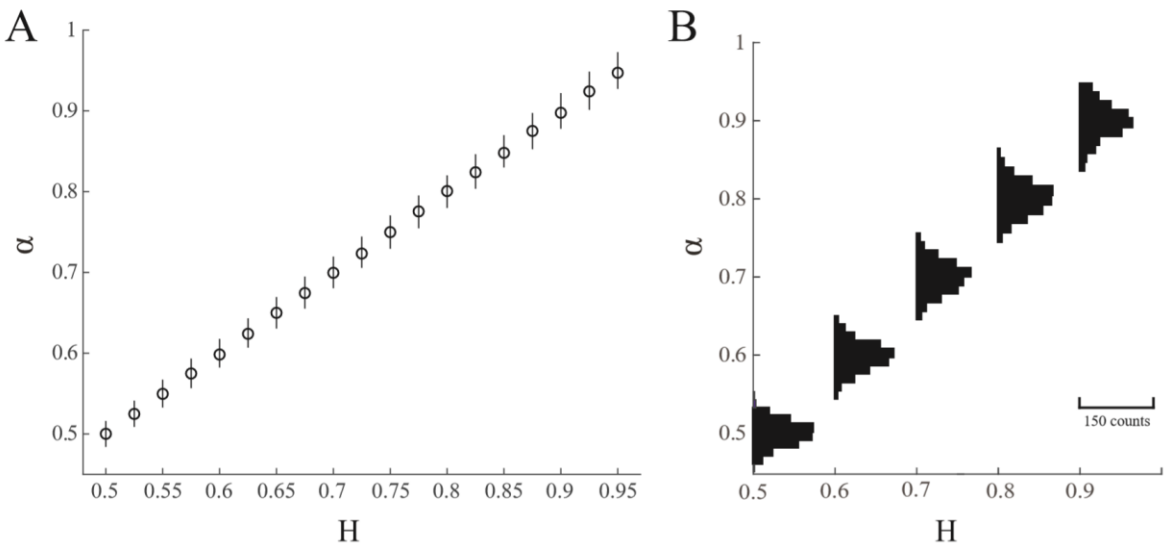

Figure 3.5 Comparison of the distribution of α values to the true H value used to create simulated data. (A) The circles indicate the mean of the distribution of α values and the line above and below indicate one standard deviation. (B) Histograms of selected distributions of α values as a function of H.

3.3.2 The variance of the DFA estimate decreases for longer signal lengths

There is greater uncertainty in DFA exponent estimation in shorter data segments because the smaller box sizes are typically fixed, and a smaller number of data points will fall into each box size. We tested this effect using simulated data with H ranging from 0.50 to 0.99. We recorded the difference between the α for a selected segment of the time series and $\hat{\alpha}$, and we aggregated the results from 50 independent realizations of simulated data (Figure 3.6A). The distributions indicate no trend in the median α value as a function of segment length, but the variance of the distribution is higher for shorter data segments than longer segments.

The Control EEG data show bias in α, with the largest effect in the lower frequency bands (Figure 3.6B). Similar to the simulation results (Figure 3.6A), the variance decreases with longer signal lengths. Though the EEG data interquartile range is only slightly larger than the simulated data, there are more outliers in the human EEG data. This is most likely due to the presence of artifacts.

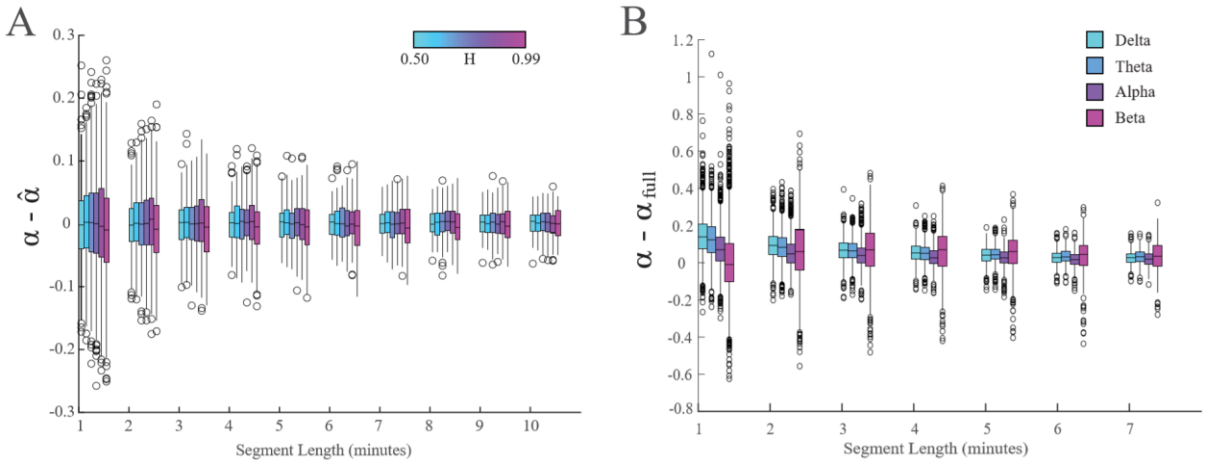

Figure 3.6 Boxplots showing the effect of data segment length on the DFA exponent. The horizontal black line denotes the median of the distribution and the bars indicate the interquartile range. (A) In simulated data, we varied both segment length and the value of H, which ranged from 0.50 to 0.99; boxplots for each value of H are placed adjacent to one another, in ascending order. The DFA exponent recorded for the signal segment is α, and the exponent recorded for the original 20-minute simulated data is $\hat{\alpha}$. (B) In the Control EEG dataset, we compared α for each segment length to the value measured for the full signal (α_{full}). The full signal consisted of the sleeping portions of the data from all channels for 10 of the 21 subjects.

3.3.3 Discontinuities and artifacts increase the variance of the DFA estimate

Bootstrapping and the removal of artifacts will introduce discontinuities into the time series. We examined the effect of such discontinuities on the variance of the DFA exponent. In simulated data with varying numbers of added discontinuities, we found no trend in the median $\alpha - \hat{\alpha}$ value for any value of H (Figure 3.7A). Here α represents the DFA exponent with added discontinuities and $\hat{\alpha}$ is the DFA exponent of the signal with no discontinuities. The standard

deviation of the distribution, however, increased with the number of added discontinuities. This increase in standard deviation was greater for more positively correlated signals (Figure 3.7B). In the Control subject EEG data, the introduction of discontinuities due to artifact removal had less effect on the variability of α than the presence of the artifacts (Figure 3.8). The addition of discontinuities caused slight increases in the median α value and the variance of the distribution (Figure 3.8A). This trend was present in all frequency bands; representative data from the theta frequency band is shown. We note that the variance of α in EEG data (Figure 3.8A) is only slightly bigger than the variance of α in simulated data (Figure 3.7). The presence of artifacts was associated with higher α values relative to data in which artifacts had been removed (α_{full_clean}) (Figure 3.8B). The bias of the distribution due to the presence of artifacts (Figure 3.8B) is larger than the bias solely due to discontinuities (Figure 3.8A). The α values from each permutation of artifact time periods sampled are shown in Figure 3.9 and the median of those values are shown in Figure 3.8B.

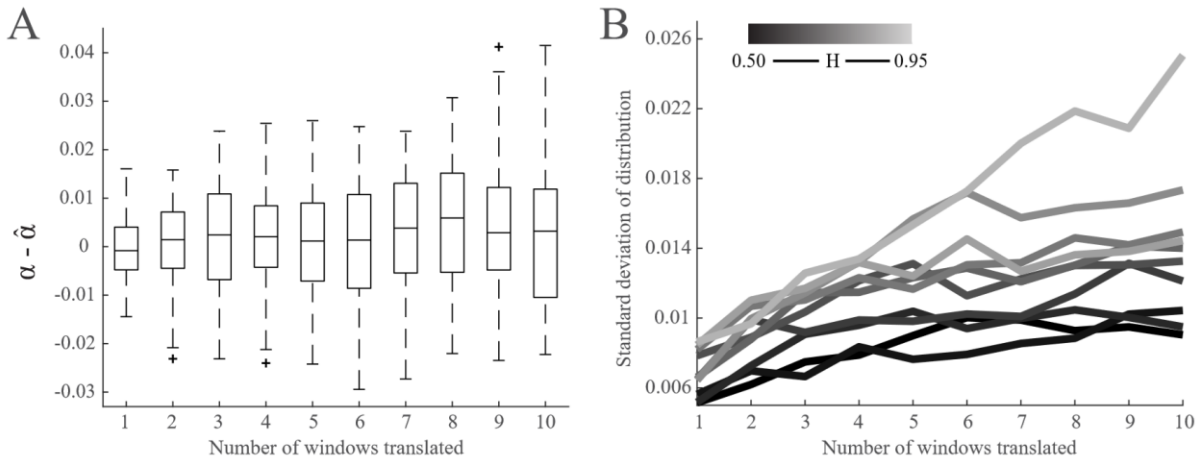

Figure 3.7 The effect of time series discontinuities on α. (A) Differences between α values measured for twenty-minute simulated time series with translated windows compared to the DFA exponent measured using the original twenty-minute signal ($\hat{\alpha}$). Signals were simulated with H=0.75. (B) Standard deviations of $\alpha - \hat{\alpha}$ distributions for varying values of H.

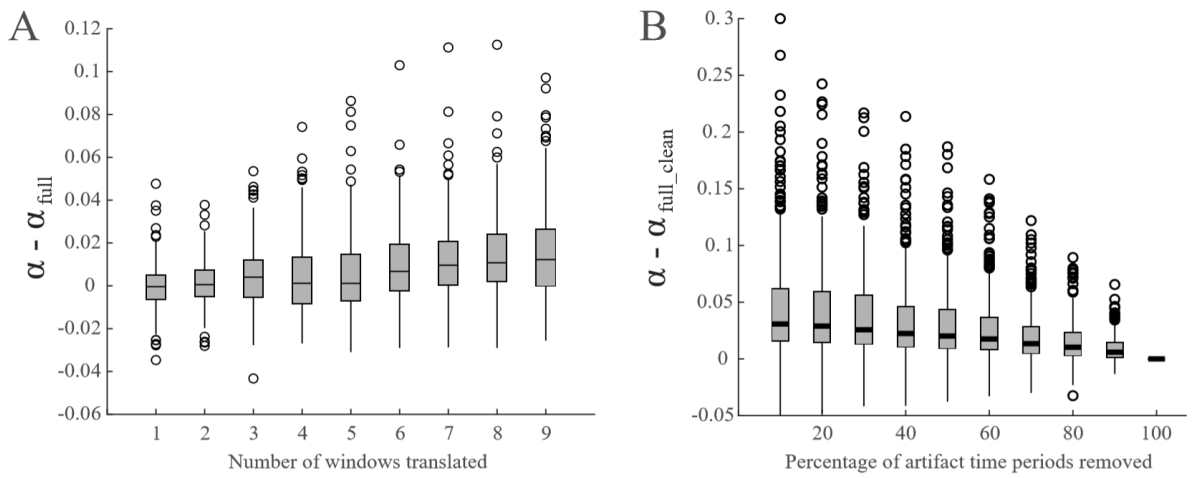

Figure 3.8 The effect of time series discontinuities and artifacts on α. (A) In the Control EEG dataset (n=13 subjects), we measured differences between α values for EEG time series with translated windows compared to the DFA exponent measured using the original continuous EEG signal (α_{full}). The median and interquartile range of the distribution increased as a function of the number of introduced discontinuities in the time series. (B) We also compared Control EEG data (n=21) with artifacts removed (α_{full_clean}) to data with only a subset of the artifact time periods removed. We randomly selected 10% of artifact time periods to be removed from the data for twenty iterations and recorded the median value for each channel. This was repeated for an increasing percentage of artifact time periods in 10% increments. Artifacts increase the estimate of α and bias the distribution more than discontinuities alone. Representative data is shown from the theta frequency band in both panels.

3.3.4 Bootstrapped distributions of DFA exponents in simulated data

Applying MBB to time series generates independently sampled realizations of the time series (correlated within a time series; independent across different time series realizations) upon which distributions of a test statistic can be derived. We generated simulated data, block-bootstrapped the signal, and measured α for 500 iterations. We tested simulated data with values of H ranging from 0.50 to 0.95, in increments of 0.05, using twenty realizations for each value of H (Figure 3.10). The median values of the bootstrapped α distributions for individual realizations varied from one another despite being generated with the same Hurst exponent (Figure 3.10A).

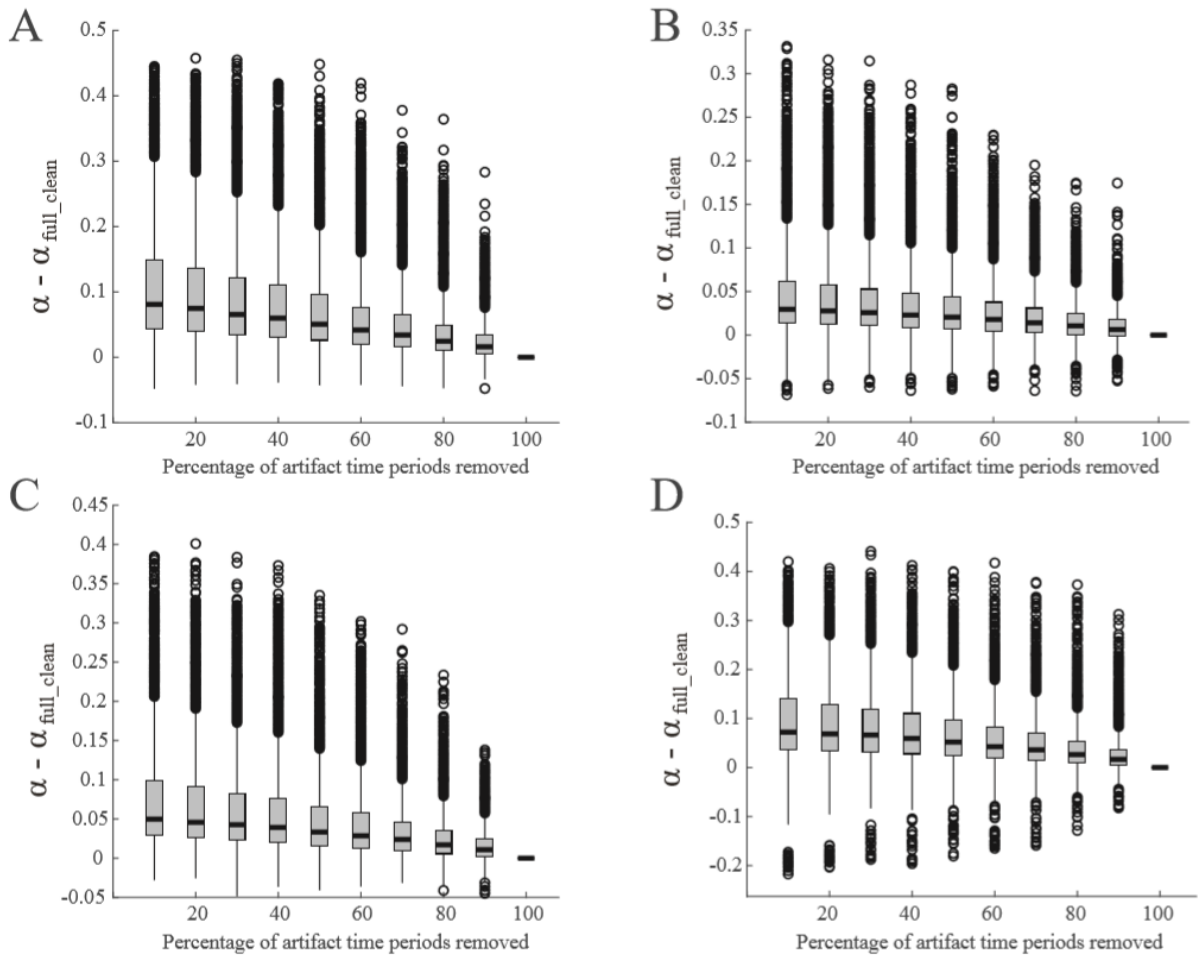

Figure 3.9 Effect of artifact removal for all twenty iterations in all channels for 21 subjects in the Control dataset. Deviations in DFA exponents are shown for the (A) delta, (B) theta, (C) alpha, and (D) beta frequency bands.

However, the variation in the median was comparable to the variation measured for independent simulated data realizations (Figure 3.5), so this variation was expected.

We also analyzed the distribution of exponent deviations, defined as the difference between the DFA exponent measured for the bootstrapped signal (α) and the DFA exponent measured for the original signal ($\hat{\alpha}$) (Figure 3.10B). When the DFA exponent deviations ($\alpha - \hat{\alpha}$) were aggregated over all twenty realizations of noise for all H values, the greatest differences occurred in the more strongly correlated signals (Figure 3.11). Distributions generated with Hurst

exponents of 0.9 and 0.95 had a positive bias of 0.012 and 0.023, respectively (Figure 3.11). The standard deviation of these distributions also increased as H increased.

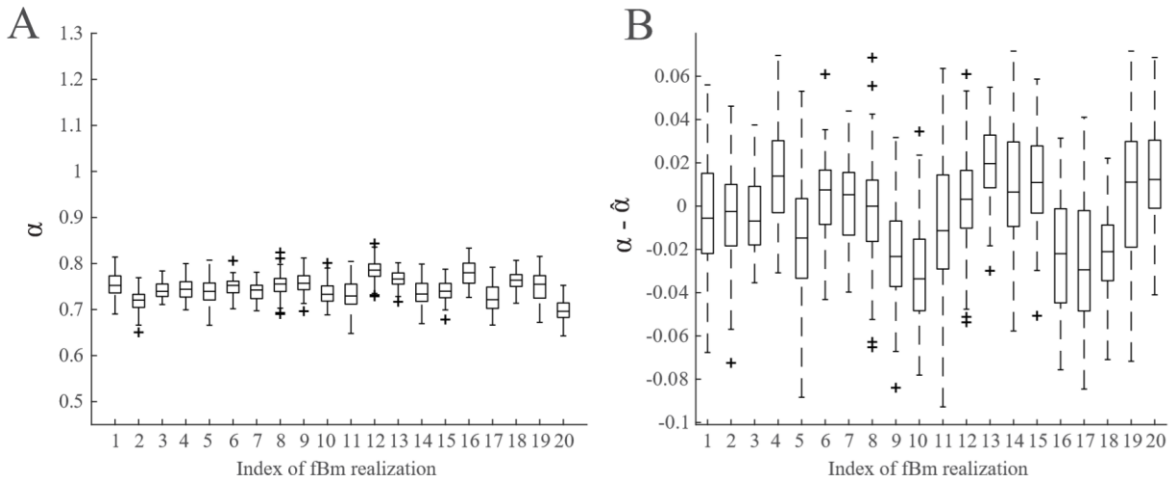

Figure 3.10 Applying DFA to iteratively bootstrapped time series generates a distribution of α values for the signal. (A) The distributions of α for 20 independent realizations of fBm generated with H = 0.75. (B) Deviations in DFA exponents ($\alpha - \hat{\alpha}$) for the data shown in (A).

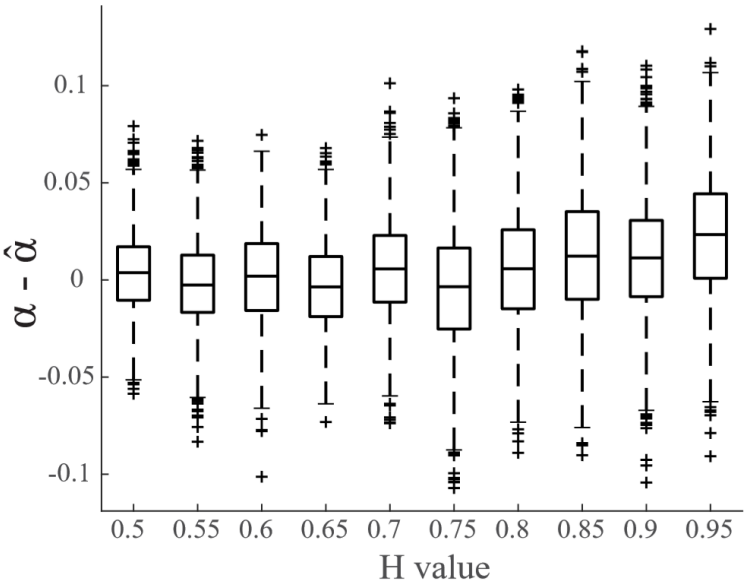

Figure 3.11 Deviations in DFA exponents ($\alpha - \hat{\alpha}$) over all realizations for tested H values.

3.3.5 DFA bootstrapping in long-term EEG data

We used MBB and DFA to measure the statistical significance of changes in α in the Long-Term dataset (Figure 3.12). This EEG dataset contained transitions in brain state over 292.1 minutes: the subject was awake at the beginning of the recording, fell asleep at minute 56, woke up at minute 79, and then fell asleep again at minute 149 for the rest of the recording. We found significant differences between α during waking and sleep in all frequency bands and in all channels except for channel Cz (changes in channels Fz, C3, C4, and F4 were only significant in the delta and theta bands).

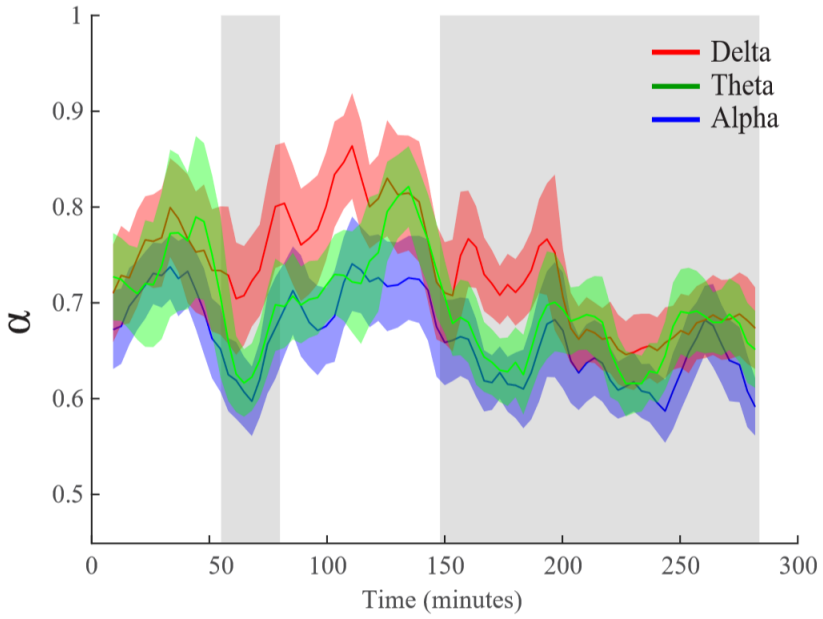

Figure 3.12 Bootstrapped distributions reveal differences between wake and sleep in a healthy human subject from channels O1 and O2. The averaged mean of the bootstrapped distribution is the dark solid line of the respective color for each frequency band. The translucent colored area around each distribution represents the 95% confidence interval. Periods of sleep are marked with a grey background.

3.3.6 DFA bootstrapping for within-subject comparison of pre- and post-treatment EEG data

Lastly, in the IS Subject dataset, we compared α before treatment and after treatment in the delta, theta, and alpha frequency bands (Figure 3.13). For Subject A (blue), in all frequency bands and all channels, there was a statistically significant increase in the strength of correlations after successful treatment (Figure 3.14) (Wilcoxon rank-sum, corrected via Benjamini-Hochberg procedure, adj. $p<0.05$). For Subject B (red), the distributions were significantly different in all channels except P3 in the delta band, O2 in the theta band, and P4, O1, and T3 in the alpha band (Wilcoxon rank-sum, corrected via Benjamini-Hochberg procedure, adj. $p<0.05$).

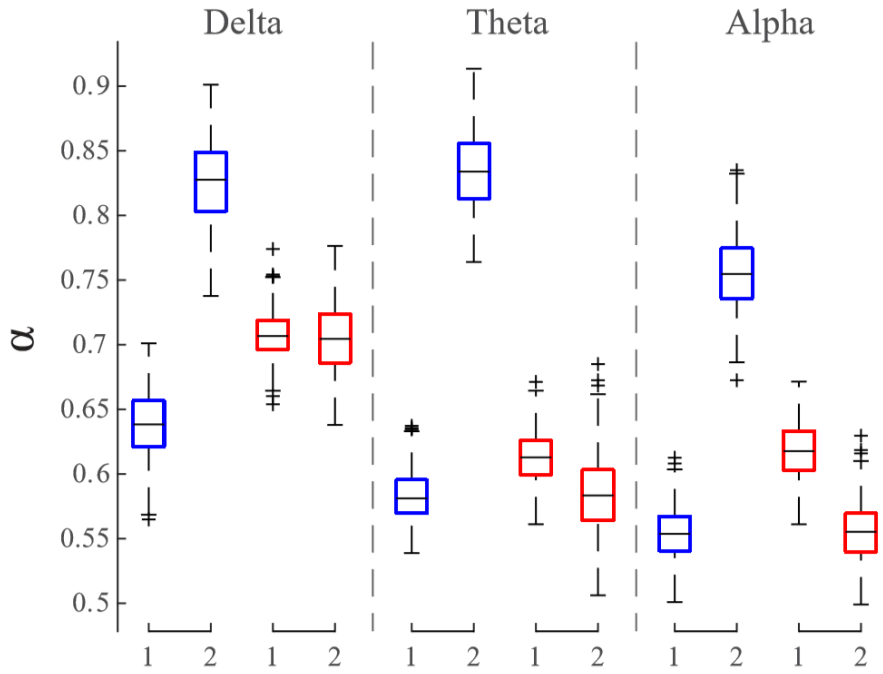

Figure 3.13 Bootstrapped distributions of α for pre- (denoted 1) and post-treatment (denoted 2) EEG data in subjects with infantile spasms. Blue boxplots represent Subject A, a subject that responded to treatment. Red boxplots represent Subject B, a subject that did not respond to treatment. Results are shown for all frequency bands in EEG channel P3. All channels are shown in Figure 3.14.

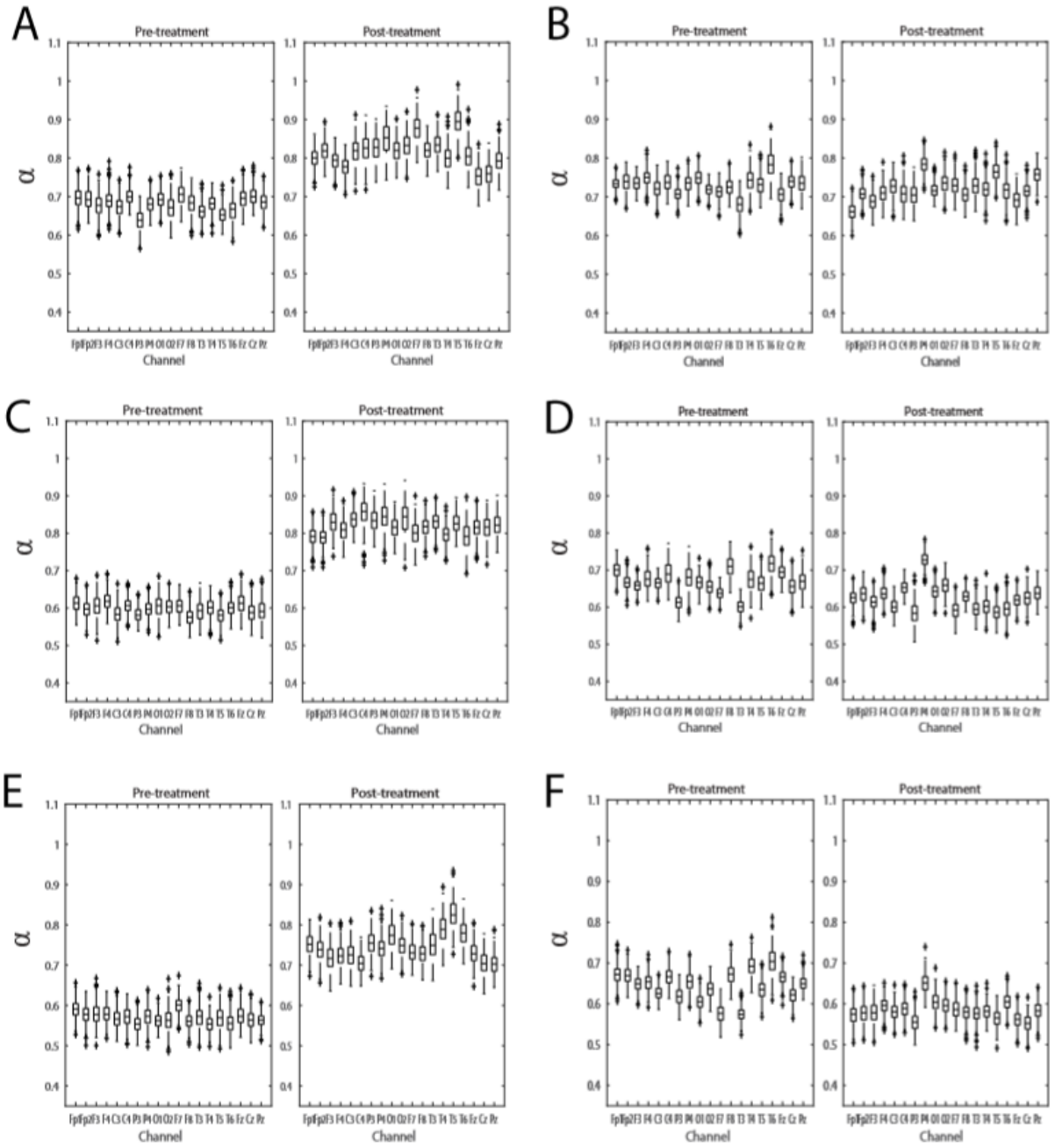

Figure 3.14 Distributions of α for all channels in pre- and post-treatment data from Subjects A and B. (a) Subject A, delta frequency band, (b) Subject B, delta frequency band, (c) Subject A, theta frequency band, (d) Subject B, theta frequency band, (e) Subject A, alpha frequency band, and (f) Subject B, alpha frequency band.

3.4 Discussion

When applying Detrended Fluctuation Analysis (DFA) to neural data, one major limitation is that there is no framework to examine the variation of the Hurst exponent estimator. Our proposed approach integrates the moving block bootstrap with DFA to produce statistically rigorous inferential results. Our approach enables the calculation of confidence intervals which give an indication of the uncertainty of the Hurst exponent estimate in neural data. We showed that the use of short data segments increases the variability of the DFA exponent (Figure 3.6), suggesting the use of longer segments of data whenever possible. We also confirmed previous findings that, in positively correlated signals, the introduction of discontinuities causes small increases in the measurement variance. In contrast, the presence of artifacts positively biases α. This effect can be mitigated by removal of artifactual segments, even though this introduces additional discontinuities (assuming enough data remains to obtain a robust estimate of the scaling properties). This allows techniques like DFA to be successfully applied to human neural data. When analyzing EEG data, MBB-DFA provided a time-varying measurement of α, and we found that there were significant differences between wake and sleep (Figure 3.12). For application to a clinical setting, we show that our method can be used to compare pre-treatment and post-treatment EEG data in subjects with infantile spasms (Figure 3.13). This demonstrates the potential impact of our approach, as single-subject comparisons were not possible with previously available methods.

3.4.1 Practical considerations for implementation of MBB and DFA on neural data

3.4.1.1 Selection of DFA window size

Although there are many ways to measure temporal dependence in neural time series [142]–[147], we chose to use DFA to estimate the Hurst parameter due to its widespread application in current neuroscience literature [92], [96], [104], [106], [121]. The method was originally developed to accurately estimate the Hurst exponent despite specific nonstationarities in the data, supporting its use as the preferred method to analyze temporal structure [99], [110], [148]. However, some groups have heavily criticized DFA in this regard in recent years, showing circumstances where certain nonstationarities and parameter selection greatly influenced the accuracy of the measure [100], [101]. For example, [100] showed that the resultant DFA plot will become nonlinear if the minimum window size is too small. Likewise, if window sizes are too long, the resultant plot may have "cross-over" points, requiring special analysis techniques [98], [102]. Additionally, certain nonstationarities such as periodicity and trends have been shown to reduce the accuracy of the algorithm [149], [150].

To address the issue of appropriately-sized windows for DFA (M, Figure 3.3A), we chose our smallest window size to be 1 second (200 samples) (Figure 3.4). This exceeds the window size in which nonlinearity in the DFA plot occurs [100]. We set our largest window size to 1/10 of the signal length [99]. Earlier comparison with the autocorrelation function of the amplitude envelope in these data showed that correlations were significant up to 100 seconds [151]. Our maximum window size was on the order of 120 seconds for both the simulated data and the longest control datasets.

3.4.1.2 Time series length

We showed that the variance of the Hurst exponent estimate was a function of the length of the time series being analyzed. While some DFA studies analyze segments of data that are

only several seconds long [104], [152], we showed that the most reliable estimates of $\hat{\alpha}$ are achieved for segments of data that were several minutes long (Figure 3.6). This is not surprising since longer time segments have more time points and hence will result in lower variances in the Hurst exponent estimator. We note that estimates of H using short time segments are not necessarily incorrect; they may simply be describing the temporal structure of the signal more locally and are more subject to variation. However, because the variance in the measure is greater with shorter segments of data, more subjects or trials may be necessary to demonstrate a significant result. These results also highlight the specific value of the MBB method. For example, we can compare the distribution of DFA exponents acquired by simply cutting the time series into smaller segments (Figure 3.6A) to the distribution of DFA exponents resulting from MBB (Figure 3.10B). The bootstrapped values were closer to the value for the original signal than those measured for shorter segments, showing that MBB provided a better estimate of the Hurst exponent without sacrificing statistical strength.

We found that the variation in $\alpha - \hat{\alpha}$ stabilized with segments of EEG data five to eight minutes long, defining a minimum length to ensure the best attainable estimate of the Hurst exponent. This result informed our decision to use global windows (B_G) of 1000 seconds: because employing a block-bootstrap involved calculating α for 500-second segments (8.33 minutes) of block shuffled data, this choice of global window size ensured that the bootstrapped data length still exceeded the minimum data length of five to eight minutes.

3.4.1.3 Parameters for moving block bootstrap

We chose a length of 50 seconds for B_B because a sufficient binomial coefficient was needed to perform 500 iterations of random block sampling. In the simulations, we randomly

sampled ten 50-second blocks of data from the 1200 seconds of data (24 blocks, each 50 seconds long). In the long-term datasets, we chose ten 50-second blocks of data from the 1000 seconds of data in the global window B_G (20 blocks, each 50 seconds long). These parameters resulted in binomial coefficients of 1961256 and 184756, respectively, exceeding the coefficients needed for 500 iterations of sampling ($_nC_k=\frac{n!}{k!(n-k)!}$). We note that the differences between DFA exponent distributions generated for 1200-second datasets and 1000-second datasets were negligible (data not shown).

3.4.1.4 Discontinuities and Artifacts

Lastly, we showed that discontinuities in the data cause a slight increase in the median value and variance of the distributions of DFA exponents in EEG data. An increase in the variability reduces the chances that two distributions will be significantly different from one other. Minimizing the number of discontinuities can reduce this effect, e.g. if two artifacts are separated by a small amount of time, removing them both along with the intervening data will introduce one discontinuity instead of two.

Artifact removal improves confidence in the DFA estimate because it removes data of non-neural origin, but the process introduces discontinuities into the data. We showed that the presence of artifacts increases the median value of the DFA exponent distribution (Figure 3.8B). The introduction of discontinuities due to artifact removal had less of an impact on the estimate than the presence of artifacts in the data (Figure 3.8A), substantiating the practice of removing artifacts prior to any DFA analysis. However, we must note that removing artifacts alters the temporal structure of the data. Ensuring enough data remains for robust estimates of the DFA

exponent is imperative. Alternative artifact rejection strategies like Independent Components Analysis may provide similar results while reducing the number of discontinuities in the time series [118].

Previous studies show that the DFA exponent is heavily affected by the introduction of discontinuities if the signals are anti-correlated ($0<H<0.5$) [98]. Chen et al. [2001] demonstrated that the estimate of the strength of correlations is skewed toward 0.5 when discontinuities are present in anti-correlated signals. However, our results coincided with their findings that the exponent estimation remains largely unchanged in the presence of discontinuities in positively-correlated signals [98]. In previous literature, neural signals have unanimously been described as positively correlated [92], [99].

3.4.2 Applications of MBB and DFA

We showed that MBB and DFA can be used to track changes in the temporal structure of the EEG in a healthy infant during a sleep-wake cycle (Figure 3.12). The time-varying distributions of DFA exponents showed the largest differences between wakefulness and sleep in the delta frequency band. The results shown here may mirror the work in [153], in which time-varying DFA exponents are measured via Kalman filtering and covariance calculation.

We additionally showed that these techniques could be used clinically to compare pre- and post-treatment data in two subjects with infantile spasms (Figure 3.13). The two subjects were chosen as examples to show the utility of the MBB-DFA method. In one subject, the change in α is large, while the other shows little change in α after treatment. Our previous work suggests that the larger increase in α in the responding subject may be due to changes in the neuronal network associated with treatment response. In that study, we showed that the DFA

exponent is statistically significantly lower in infantile spasms patients compared to healthy controls, and the value normalizes with successful treatment [91]. However, this effect on DFA exponent distributions calculated with MBB will need to be validated with a larger dataset.

Other groups have used DFA in clinical applications to investigate EEG changes when a patient experiences a stroke [104] and for neonatal background differentiation [121]. In an ECoG study in epilepsy patients, long-range temporal correlations measured with DFA were stronger when the electrodes were near the epileptogenic zone [105]. These studies show that DFA can provide useful information in analysis of group-wise statistics.

However, DFA has not often been used to describe within-subject changes. Although some groups have investigated properties of the DFA algorithm to assess local changes in the time series [154], these studies focus on assessing changes in temporal structure at the smallest time scales possible [121], [155]. In contrast, our study focused on filtering out local variations in the temporal structure to make conclusions about lasting, global changes in the strength of correlations in the time series, enabling tracking of slow changes in brain state or in response to treatment.

A moving-block bootstrap technique has been implemented alongside DFA before, but has not yet been applied to human neural data [130]. The variation of the DFA exponents in bootstrapped distributions of human data bore a strong resemblance to our results for simulated data. We hypothesize this is due to the long window sizes being analyzed: though we know brain activity is changing on a millisecond time scale, the average correlation strength is consistent when analyzed over hundreds of seconds. We hypothesize this to be crucial in the analysis of brain state changes, such as wake and sleep staging, as well as comparing pathological and healthy activity.

Assessing changes in the Hurst exponent over time has the potential for significant impact in the fields of cognition, brain stimulation, and medicine. This impact can be broadened further with the natural extension to a multivariate moving block bootstrap, enabling analysis of spatially-varying DFA exponents with confidence intervals. These methods can be broadly applied to longitudinal neurophysiological data, shedding light on cognitive processes and progression of mental and neurological diseases and their treatments. More specifically, when used as a measurement of the disease state in patients with epilepsy, an increase in the DFA exponent for a single patient over time can function as an objective biomarker of treatment response [91]. This could guide clinical practice, inform seizure medication selection, and ultimately lead to more effective and expeditious treatment. Similarly, the assessment of DFA exponents from single subjects over time could describe disease progression in Alzheimer's [156] or depression [157]. The ability to examine the statistical significance of within-subject differences allows for an expanded view of DFA and its use in human neural data.

CHAPTER 4

COMPUTATIONAL EEG BIOMARKERS of REFRACTORY INFANTILE SPASMS

4.1 Introduction

Although the presence of hypsarrhythmia is often used as a diagnostic criterion for IS, there is low inter-rater reliability for identification of the pattern [34], [35] and it is not a predictor of outcome [73]. Computational EEG biomarkers of IS that are independent of the presence of hypsarrhythmia would help address these challenges by providing tools for objective identification of the disease.

We investigated four computational EEG metrics that were assessed using a cohort of fifty patients treated for infantile spasms at the UCLA Mattel Children's Hospital. Because UCLA is a large referral center, this study included a much higher proportion of patients with refractory IS. We describe how the 1) amplitude, 2) power spectrum and spectral edge frequency (SEF), 3) Shannon entropy, 4) power-law scaling as measured with detrended fluctuation analysis (DFA), and 5) functional connectivity differ between IS patients and healthy control subjects of similar ages. We also compare changes in these metrics after successful and unsuccessful treatment. This work builds off of a previous pilot study [158] and is improved by the inclusion of more subjects, both sleep and awake EEG, multiple measurements per subject, and blinded calculation of computational metrics, making it the largest and most comprehensive study of its kind. Identification of objective EEG characteristics that describe the disease state may improve diagnostic accuracy, specifically in patients with long lead times that need

expedited treatment most. Additionally, assessment of these characteristics early in the treatment process may identify children that are not responding to treatment, allowing for timely transition to a new therapy.

4.2 Methods

4.2.1 Patient Data and Pre-processing

Using a clinical video-EEG database which includes all patients who underwent video-EEG monitoring at UCLA Mattel Children's Hospital between February 2014 and July 2018, we identified IS patients and controls as follows. Included IS patients fulfilled the following criteria: (1) epileptic spasms were observed on a "baseline" overnight video-EEG study, regardless of the presence or absence of hypsarrhythmia; (2) a second overnight video-EEG was performed within one month of the baseline video-EEG. Using a randomization algorithm, we selected 50 cases from those candidates who met the aforementioned criteria (Table 4.1). Two control groups were assembled. The first control group ("IS controls") consisted of children who (1) underwent overnight video-EEG to specifically evaluate for suspected infantile spasms, (2) exhibited a normal video-EEG, and (3) were deemed neurologically normal (i.e. no known or suspected neurological diagnosis as per clinical neurology notes). The second control group ("non-IS controls") consisted of children who (1) underwent overnight video EEG (not for evaluation of infantile spasms) and (2) were deemed neurologically normal (as above). Among candidate IS controls (first control group) we used a randomization algorithm to select 25 IS controls. Given that we also sought to identify controls across a pediatric age spectrum similar to the IS patients group, we included all non-IS controls up to the age of the oldest IS case, resulting in the addition of 12 subjects (total of n = 37 control subjects).

Two clips during wakefulness and two clips during sleep were extracted from the control subject recordings and both pre- and post-treatment recordings in IS patients. Each clip contained approximately 20-30 minutes of EEG data. We calculated each of the four metrics for both clips during wakefulness and during sleep and averaged the two awake metric values and two sleeping metric values for each patient to obtain one value for wakefulness and one value for sleep. All subsequent analysis was performed with the averaged values. We note that, for all patient groups, there was little variation in the metric values between clips for individual patients.

The four metrics were computed on each clip while the authors were blinded to the patient groups, clip numbers, and designation of wakefulness or sleep and pre- or post-treatment. After the computational analysis, the data were unblinded and grouped as follows: All data from the IS patients before treatment were designated as the PRE group (n=50 patients) and subjects from both the IS control group and the non-IS control group were combined into the CTRL group (n=37). After treatment, IS patients that responded to treatment (defined as a resolution or absence of hypsarrhythmia, cessation of spasms, and no clinical relapse over the next 28 days) were included in the responder (RESP) group (n=28 patients). The patients that did not meet one or more of these requirements after treatment were included in the non-responder (NONRESP) group (n=22 patients).

Time periods in the EEG containing artifact were marked using an automatic detection algorithm. The algorithm first broadband bandpass filtered the data (1.5-40 Hz, butterworth filters). The mean was subtracted from each channel, and the standard deviation was calculated from the zero-mean time series. Then time points where the absolute value of the voltage exceeded a threshold of 7.5 standard deviations above or below the mean value in any single

channel were marked. A buffer of 0.9 seconds was added to both sides of the marked extreme amplitude values to ensure that the entire artifact was marked. Data recorded during EEG impedance checks were also identified and marked. This method of artifact detection was comparable to visual detection of artifacts when assessed with the metrics described in this study, with an average of 91% concordance (Appendix A).

Data were re-referenced to a linked-ear montage for all analyses except functional connectivity, in which data were re-referenced to the common average. Data were sampled at 200 or 500 Hz with impedances below 5 kΩ. Data that were sampled at 500 Hz were downsampled to 200 Hz prior to spectral analysis. We broadband bandpass-filtered the re-referenced data from 0.5-55 Hz for the analysis of EEG amplitude, spectral edge frequency, and functional connectivity. We filtered the data into narrow frequency bands for calculation of DFA and Shannon entropy (delta band 1-4 Hz, theta band 4-7 Hz, alpha band 8-12 Hz, and beta band 14-30 Hz). Note that artifactual EEG epochs were identified using broadband filtered data, but the segments of data were removed after the band-specific filtering needed for each metric. In all cases, artifactual segments of data were excluded from all channels, even if the artifact occurred in a single channel.

4.2.2 Amplitude

Amplitude is an EEG feature closely monitored in IS, as hypsarrhythmia and other interictal patterns are often high amplitude (>200 μV), and diffuse slowing is a common feature in both ictal and interictal data [7], [8], [69]. Amplitude values were calculated using the range of the broadband filtered data in one second windows for each electrode. The variation of EEG amplitude across channels was visualized via topographic maps. We first calculated the median

amplitude values in each channel from each clip. We then constructed individual patient maps by calculating the average of the two median values from each channel. The group topographic maps were constructed from the median of the patient topographic maps within each group. The figures were generated using the MATLAB-based EEGLAB function topoplot(). To compare amplitude distributions across subjects, we calculated the empirical cumulative distribution function (CDF) for the Cz electrode in each dataset. Electrode Cz was chosen because it is minimally contaminated by artifact.

Table 4.1. Patient demographics, etiology, treatment, and response status.

Pt.#	M/F	Age Onset	Etiology	Leadtime /UKISS	AED	Pre Hyps	Resp	Other seizures
01	F	3.0	PMG	96.66/4	VGB		No	Yes
02	F	68.9	Dup15q	4.57/4	PRED		Yes	Yes
03	M	34.2	TSC	3.61/4	VGB		No	Yes
04	F	73.2	Sturge-Weber syndrome	2.30/4	PRED		No	Yes
05	M	9.8	ICH, SDH, TBI (NAT)	3.09/4	VGB		No	Yes
06	F	14.5	PMG	0.99/2	PRED		Yes	Yes
07	M	5.5	TSC	15.01/4	ACTH		No	No
08	F	3.9	Unknown	39.75/4	PRED		No	Yes
09	M	10.2	bilateral cortical malformations	0.59/2	PRED	Hyps	No	Yes
10	F	5.4	Unknown	0.56/2	VGB		No	No
11	M	3.0	TSC	2.40/4	PRED		No	No
12	M	9.0	FCD	15.44/4	PRED		No	No
13	F	0.0	HIE	11.83/4	PRED		Yes	Yes
14	F	7.6	Meningitis	0.00/0	PRED		Yes	Yes
15	M	0.1	PVL	7.89/4	PRED		Yes	No
16	M	12.9	HIE	5.98/4	ACTH		Yes	No
17	M	6.1	TSC	0.03/0	VGB		Yes	No
18	M	1.8	VAMP2	2.56/4	PRED	Hyps	No	No
19	M	33.0	47XYY	1.28/3	PRED		Yes	Yes
20	F	8.4	T21, FCD	2.07/4	PRED	Hyps	No	No
21	M	13.6	IVH	0.13/0	PRED	Hyps	Yes	No
22	F	8.5	Unknown	7.00/4	PRED		Yes	No
23	F	7.3	Lissencephaly/Pachygyria	0.69/2	PRED		Yes	No
24	F	3.1	HIE	2.17/4	PRED		Yes	Yes
25	F	3.4	CDKL5	12.88/4	PRED	Hyps	No	Yes
26	M	5.5	FCD	2.53/4	VGB		Yes	Yes
27	M	8.2	FCD	2.04/4	PRED		No	No
28	F	7.0	Unknown	4.17/4	PRED	Hyps	Yes	No
29	M	7.2	Unknown	0.56/4	ACTH		Yes	No

30	M	65.5	Unknown	2.46/4	PRED		Yes	No
31	M	20.4	Dup15q	0.23/0	PRED		No	No
32	M	17.2	FCD	6.67/4	ACTH		No	No
33	M	14.9	FCD	5.95/4	PRED		No	No
34	M	16.1	T21	1.22/3	PRED		Yes	No
35	M	3.0	Unknown	6.08/4	PRED		Yes	No
36	F	7.7	Unknown	0.00/0	PRED		Yes	No
37	F	24.4	HIE	0.00/0	PRED		Yes	Yes
38	M	8.0	Unknown	2.99/4	PRED	Hyps	No	Yes
39	F	6.0	Unknown	5.16/4	PRED		No	Yes
40	M	7.5	Unknown	2.89/4	ACTH		No	No
41	F	5.2	Unknown	0.00/0	PRED		No	No
42	F	1.0	ACC, PMG, PNH	19.78/4	VGB		No	No
43	M	8.0	HIE	0.10/0	VGB		Yes	Yes
44	F	4.8	TSC	0.66/2	VGB		Yes	No
45	M	7.1	HME	0.00/0	VGB	Hyps	Yes	Yes
46	F	31.0	T21	0.39/1	PRED		Yes	Yes
47	M	4.0	IVH	3.25/4	VGB, ACTH	Hyps	Yes	No
48	F	3.0	Aicardi	12.39/4	ACTH		Yes	No
49	F	4.5	FCD	0.03/0	PRED, VGB		Yes	No
50	M	5.1	TSC	0.13/0	PRED		Yes	No

Leadtime is defined as the time between spasm onset and diagnostic EEG. The UKISS score assigns a score of 0 for leadtimes to treatment that are 7 days or less, 1 for 8-14 days, 2 for 15 days to 1 month, 3 for 1-2 months, and 4 for >2 months [159].

4.2.3 Power Spectrum and Spectral Edge Frequency

For each channel, data were divided into 5-second epochs and the power spectrum was calculated via the fast Fourier transform. The mean power spectrum was obtained by averaging the power spectra over all epochs. We calculated the decibel change to elucidate pathological differences from physiological values. The dB change is defined as follows:

$$dBchange = 20\log_{10}\left(\frac{GROUP}{CONTROL}\right)$$

where $GROUP$ is the averaged power spectrum from the patient group of interest (PRE, RESP, or NONRESP) and $CONTROL$ is the averaged power spectrum from the CTRL group.

The spectral edge frequency (SEF) is defined as the frequency under which 95% of the power resides [160]. Topographic maps of the spectral edge frequency were created by calculating the SEF value for every channel for each patient. Group topographic maps show the median of the SEF values.

4.2.4 Entropy

Entropy is the amount of information contained in a signal, and it is conceptually related to the "disorder" or "disorganization" of the data. Shannon entropy is derived from information theory and depends only on the distribution of values in the data; it is independent from the temporal structure of the data. The Shannon entropy was calculated for every channel in each clip.

The Shannon entropy H is defined as follows [161]:

$$H(X) = -\sum_{i=1}^{n} p(x_i) \log_2 p(x_i)$$

where $p(x_i)$ is the probability of observing the i^{th} value of the bin series in data x, and n is the number of bins [162]. The entropy calculation has units of bits, and higher values indicate more stochastic behavior [90], [103], [163]–[165]. Entropy was calculated for every channel based on the entire EEG clip and then averaged to obtain a single entropy value per patient. Patient entropy values were compared across patient groups.

Because entropy measures the probability that a certain value will be present in the signal, the number of bins used in the calculation must be calculated for individual datasets. We calculated the optimal number of bins according to Freedman and Diaconis, 1981 [166] as described by Cohen, 2014 [162]:

$$nbins = \left\lceil \frac{\max(x) - \min(x)}{2Q_x n^{-\frac{1}{3}}} \right\rceil$$

where x is the signal being analyzed, Q_x is the interquartile range of the distribution of x, and n is the total number of data points [162]. We recorded the optimal bin number for every channel, then averaged over all channels to obtain an optimal bin number for every patient and averaged again over all patients to obtain an optimal bin number. This procedure was repeated for each frequency band.

4.2.5 Detrended Fluctuation Analysis

Detrended Fluctuation Analysis is a statistical estimation algorithm used to assess the strength of long-range temporal correlations in time series [99], [110], [167]. Specifically in neural time series, this temporal dependence occurs on the order of tens of seconds and is believed to reflect the brain's ability to control its neuronal synchrony [92]. Detrended Fluctuation Analysis (DFA) was implemented using the following algorithm, adapted from Peng at al. [110]and Hardstone et al. [99]:

We first extracted the amplitude envelope by calculating the magnitude of the Hilbert transform of the bandpass-filtered signal. The mean of the amplitude envelope was subtracted, and we computed the cumulative sum of the zero-mean signal. This signal was divided into equally-sized windows with 50% overlap. Within each window, we performed a linear fit of the data, subtracted the fit from the time series, and calculated the standard deviation of the detrended signal. After computing the standard deviations of the detrended signal for all windows of that size, we recorded the median standard deviation for that window size. This

process was repeated for logarithmically-spaced window sizes ranging from 1 second to 1/10 of the signal length. If the recording exceeded 1200 seconds in length, the maximum window size was set to 120 seconds.

We plotted the median standard deviations on a logarithmic scale against the log-spaced window sizes; a linear result indicates power-law scaling in the time series. The slope of this line, denoted α, is a direct estimation of the Hurst parameter and reflects the strength of the temporal correlations present in the time series [99]. The α value for positively correlated signals varies between 0.5 and 1.0.

We averaged α from all individual channels to obtain a single value for each recording. The intercept of the DFA plot (β) was calculated by extrapolating on the logarithmic plot to find the fluctuation value when window size equaled one sample, the value at which the logarithm of the window size equals zero [151]. Similar to the DFA exponent, we averaged β from all channels to obtain a single value for each patient.

We hypothesized that the post-treatment values for responder patients would be closer to the α and β values of control patients. To test this, we counted the number of pre-treatment and control data points that were within a given region surrounding the post-treatment α and β values. For each post-treatment data point positioned at (α_i, β_i), we identified all pre-treatment and control data points within an ellipse surrounding (α_i, β_i) with a semi-minor axis $r_x = 0.05$ and a semi-major axis $r_y = 0.2$. These radii were chosen to approximately match the ratio of the ranges of the two parameters. Let P_{IS} represent the number of PRE data points within the ellipse and let P_{CTRL} denote the number of CTRL data points within the ellipse. We calculated the "net value" within the ellipse, calculated as: $netVal = -P_{IS} + P_{CTRL}$. Thus, if the post-treatment data

point was more centered in the PRE data points, $netVal$ would be more negative. If the post-treatment value was closer to the CTRL data point cluster, the $netVal$ would be more positive. We hypothesized that the responder patients would have a more positive $netVal$ and P_{CTRL} after successful treatment than non-responder patients.

4.3 Results

4.3.1 High amplitude in ES

The EEG amplitude in channel Cz was significantly higher in the PRE group than the CTRL group in both wake and sleep (Wilcoxon rank-sum test, $p<0.05$). The difference between PRE and CTRL amplitude empirical CDFs was more pronounced during wakefulness than sleep (Figure 4.1). Topographic maps of EEG amplitude revealed that the highest amplitudes were situated frontally during wakefulness and more centrally during sleep in both the PRE and CTRL groups (Figure 4.2). The amplitude values were significantly higher in all channels in the PRE group than the CTRL group in wakefulness and sleep (Wilcoxon rank-sum, corrected via Benjamini-Hochberg procedure, adj. $p<0.05$).

Significantly higher amplitudes were observed in the post-treatment NONRESP group when compared to the RESP group in wakefulness and sleep (Wilcoxon rank-sum, $p<0.05$), and this was reflected in the empirical CDFs (Figure 4.3). The topographic maps revealed similar topographies in wake and sleep as the PRE and CTRL groups, with amplitude slightly higher frontally in wakefulness and centrally in sleep (Figure 4.4). The channel amplitudes were significantly higher in the NONRESP group than the RESP group in all channels in waking and sleep data (Figure 4.4) (Wilcoxon rank-sum, corrected via Benjamini-Hochberg procedure, adj. $p<0.05$).

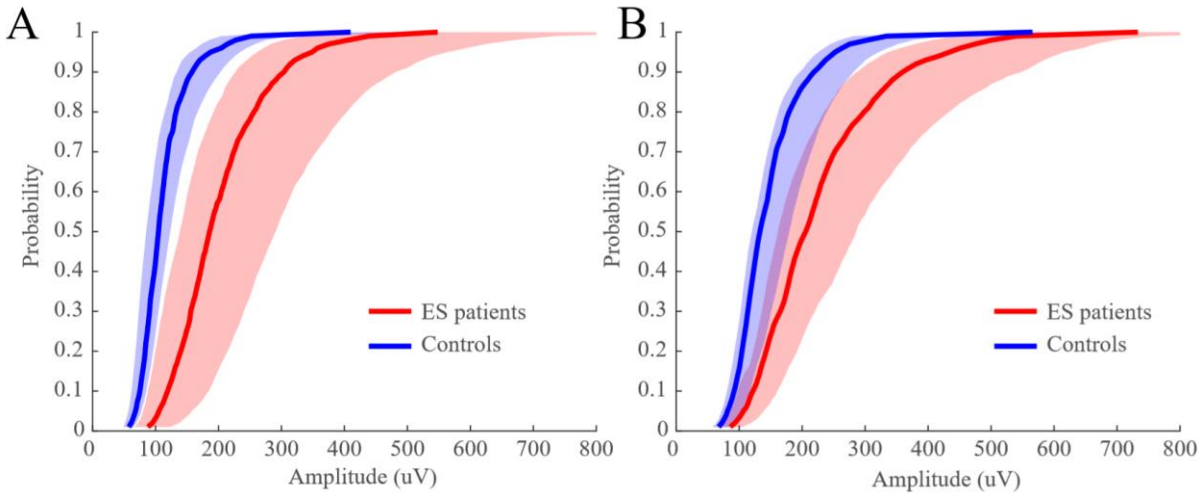

Figure 4.1 Empirical cumulative distribution functions from the Cz electrode in (A) waking data and (B) sleeping data from IS patients and control subjects. The solid line indicates the median of the group CDF values and the shaded region covers the interquartile range. Red represents the PRE group and blue represents the CTRL group.

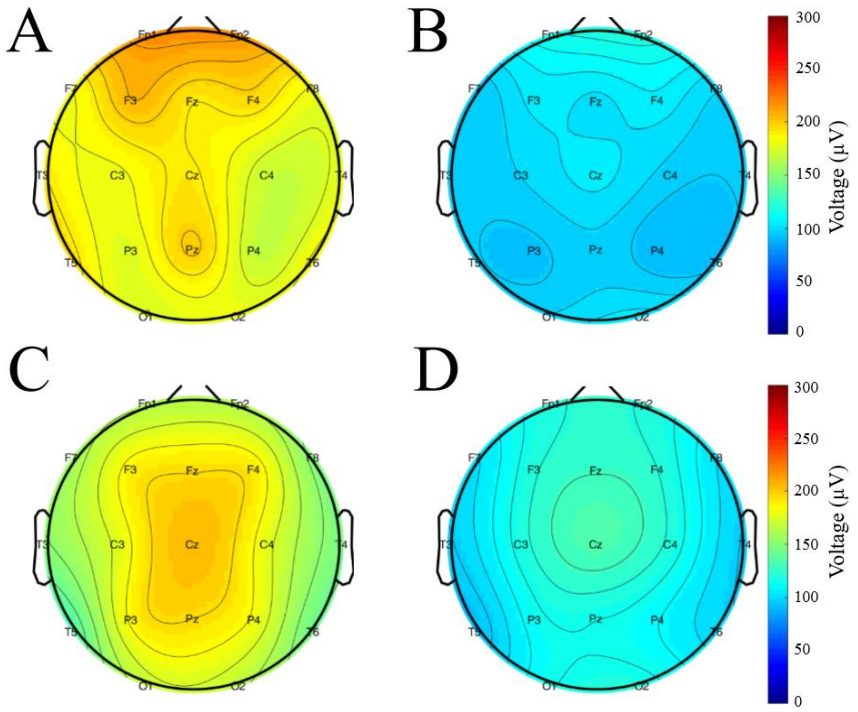

Figure 4.2 Topographic maps of EEG amplitude for (A) wake PRE patients, (B) wake CTRL subjects, (C) sleep PRE patients, and (D) sleep CTRL subjects. Median amplitude values were calculated for every patient in every channel, and the topographic maps show the median value of the group in each channel. Waking data exhibited higher amplitudes frontally while sleeping data exhibited higher amplitudes centrally.

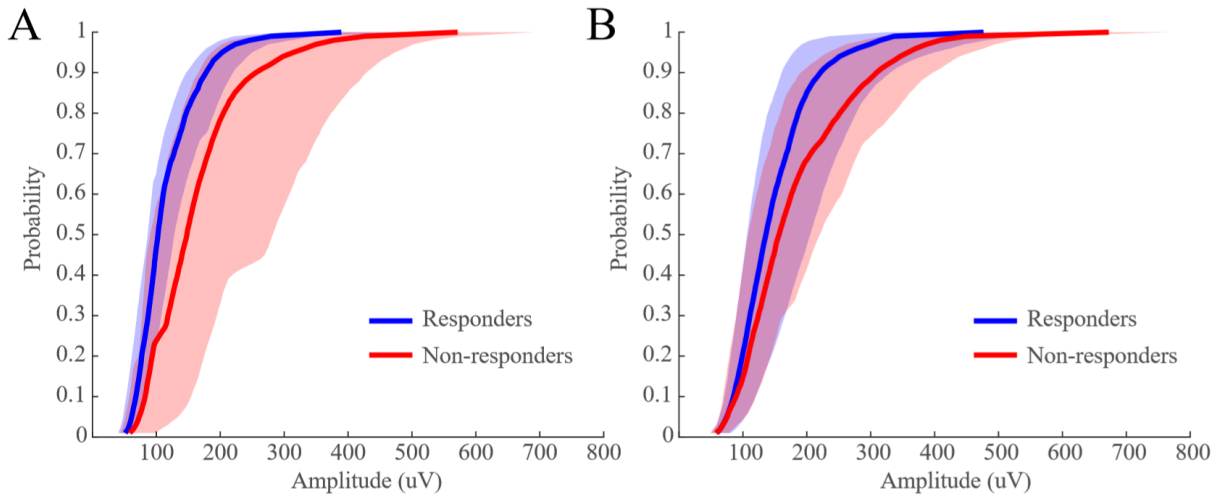

Figure 4.3 Empirical cumulative distribution functions from the Cz electrode in (A) waking data and (B) sleeping data in patients that did and did not respond to treatment. The solid line indicates the median of the group CDF values and the shaded region covers the interquartile range. Blue represents the RESP group and red represents the NONRESP group.

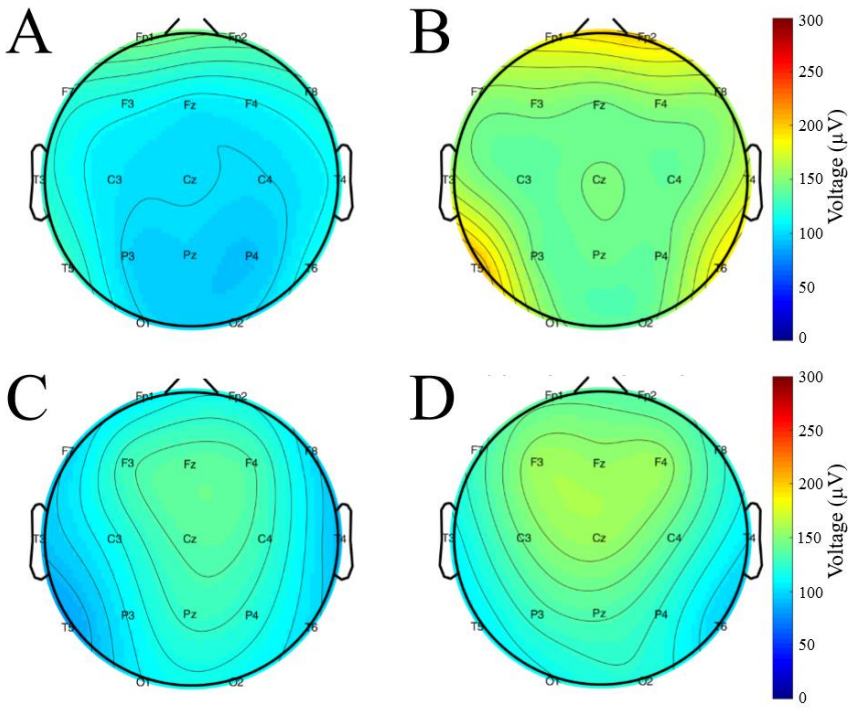

Figure 4.4 Topographic maps of EEG amplitude for (A) wake RESP patients, (B) wake NONRESP subjects, (C) sleep RESP patients, and (D) sleep NONRESP subjects.

4.3.2 Suppression in theta power corresponds with treatment response

During wakefulness, the PRE group exhibited higher power in the lower frequency bands when compared to CTRL, with power up to 10 dB higher in some channels (Figure 4.5A). In sleep, the power was greater for PRE than CTRL across all frequencies, although the increases in 4-5 Hz and 11-13 Hz power were not as large as in the other bands (Figure 4.5B). For comparison, the raw power spectra for PRE and CTRL are shown in Figure 4.6. When averaged for all patients in the group, the power spectra in both PRE and CTRL groups exhibit higher power in the delta frequency band but lower power in the alpha (8-12 Hz) and beta (13-30 Hz) bands during sleep when compared to wakefulness (Figure 4.6).

We compared the power spectra of the RESP and NONRESP groups to the CTRL group to assess how the power spectra changes in response to treatment (Figure 4.7). During wakefulness, both the RESP and NONRESP groups exhibited higher power in the delta and beta frequency bands and a suppression of power in the theta and low alpha bands (Figure 4.7A and Figure 4.7B). The suppression of theta was more pronounced in the RESP than NONRESP group, with differences as low as -4 dB (Figure 4.7A and Figure 4.7B). In the RESP group during sleep, the suppression of activity increased in magnitude and broadened in frequency, covering the entire theta and alpha frequency bands and part of the beta band, with values as low as a -8 dB change from CTRL data (Figure 4.7C and 4.7D). In contrast, the NONRESP group displayed higher power, reaching a 6 dB increase in almost all frequencies except for theta (Figure 4.7C and Figure 4.7D). These results are explained somewhat in the raw power spectra of RESP and NONRESP (Figure 4.8). RESP exhibited slightly higher power in the alpha and beta frequency bands than NONRESP during wakefulness (Figure 4.8A and Figure 4.8 B).

The spectral edge frequency (SEF) is defined as the frequency under which 95% of the power resides. Topographic maps revealed lower SEF values in the medial head regions in both sleep and awake EEG in all groups, and the SEF values were much lower in sleep than awake data (Figure 4.9 and Figure 4.10). The SEF values in the PRE group were significantly lower than the CTRL group in all channels in awake data, but the differences were not significant in sleep data in any channels (Figure 4.9) (Wilcoxon rank-sum, corrected via Benjamini-Hochberg procedure, adj. $p<0.05$). The differences in SEF values for the RESP and NONRESP groups were less pronounced, with no statistically significant differences in SEF values when comparing RESP and NONRESP (Figure 4.10) (Wilcoxon rank-sum, corrected via Benjamini-Hochberg procedure, adj. $p<0.05$).

4.3.3 High entropy in ES

Shannon entropy values were significantly higher in the PRE group than the CTRL group in the delta, theta and beta frequency bands in awake data, while only the delta band was significantly higher during sleep (Wilcoxon rank-sum test, corrected via Benjamini-Hochberg procedure, adj. $p<0.05$) (Figure 4.11). There were no significant differences between the RESP and NONRESP entropy values in awake data (Figure 4.12A). However, patients in the RESP group exhibited significantly higher entropy values than the NONRESP group in all bands in sleep (Figure 4.12B) (Wilcoxon rank-sum test, corrected via Benjamini-Hochberg procedure, adj. $p<0.05$).

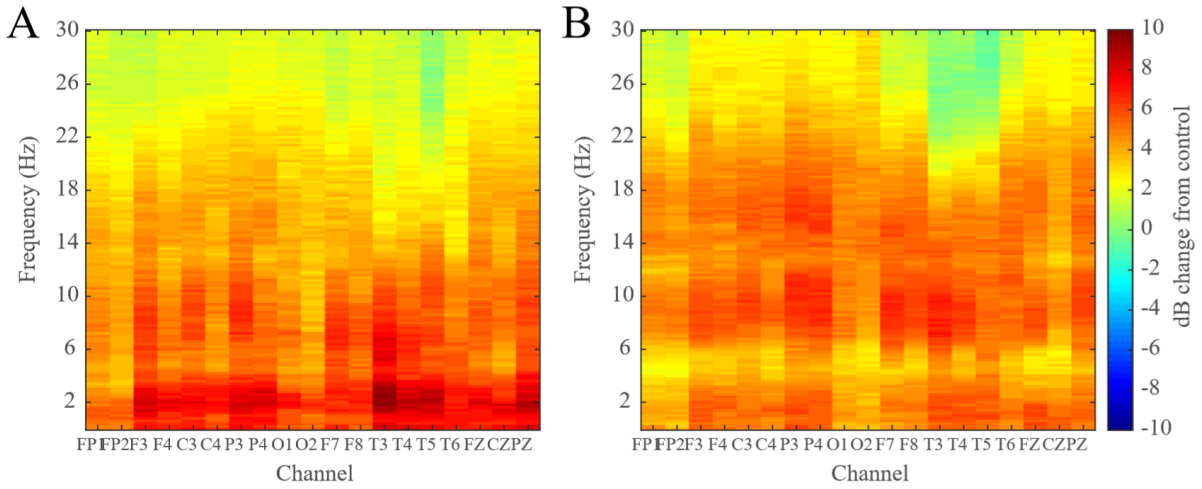

Figure 4.5 Power spectrum in PRE relative to the power spectrum of CTRL in (A) wakefulness and (B) sleep data. The EEG power is higher in IS patients in all frequency bands, with the largest increases occurring in the delta and alpha frequency bands during wakefulness and the alpha and beta frequency bands during sleep.

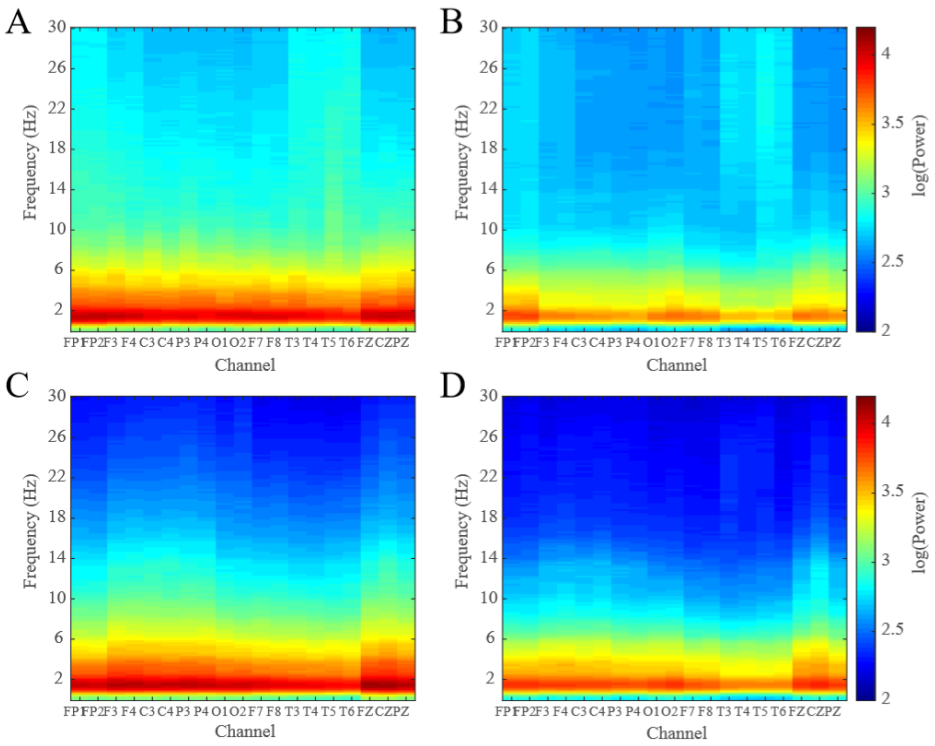

Figure 4.6 Log-transformed EEG power from 0-30 Hz in all channels for (A) wake PRE patients, (B) wake CTRL subjects, (C) sleep PRE patients, and (D) sleep CTRL subjects.

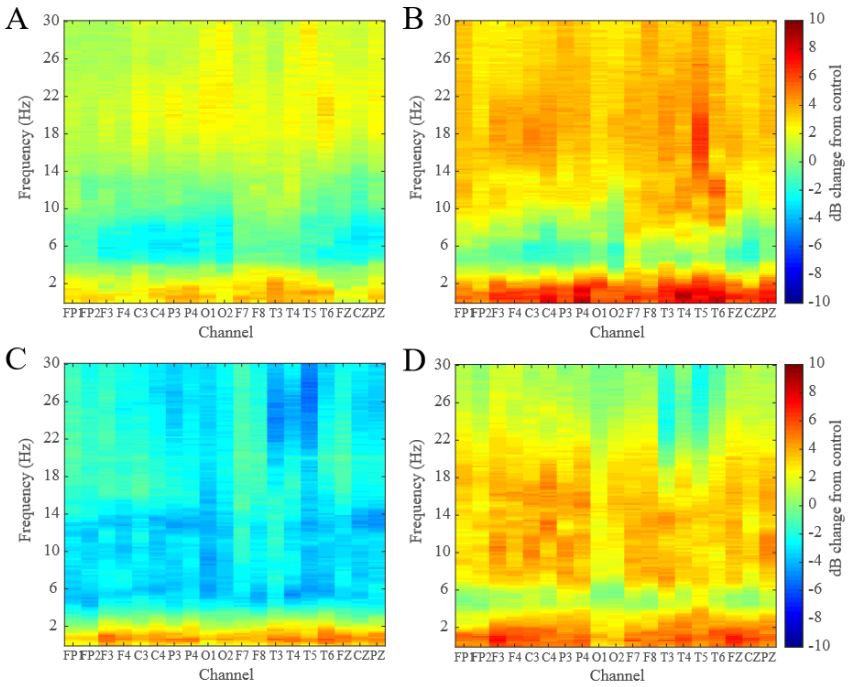

Figure 4.7 Power spectrum of RESP group and NONRESP group relative to control subjects. Plots show the decibel change of (A) wake RESP relative to waking controls, (B) wake NONRESP relative to waking controls, (C) sleeping RESP relative to sleeping controls, and (D) sleeping NONRESP relative to sleeping controls.

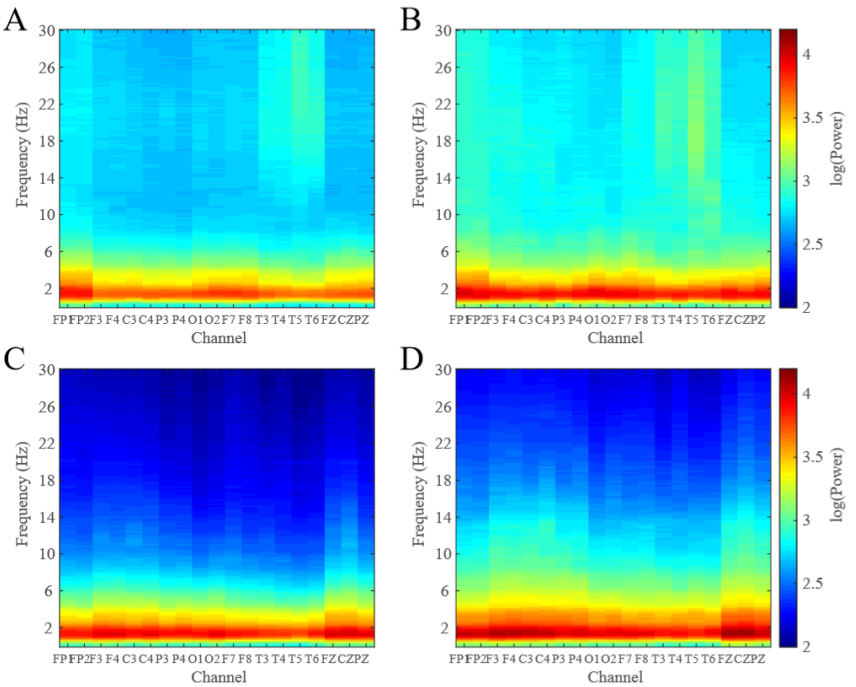

Figure 4.8 Log-transformed EEG power from 0-30 Hz in all channels for (A) wake RESP patients, (B) wake NONRESP patients, (C) sleep RESP patients, and (D) sleep NONRESP patients.

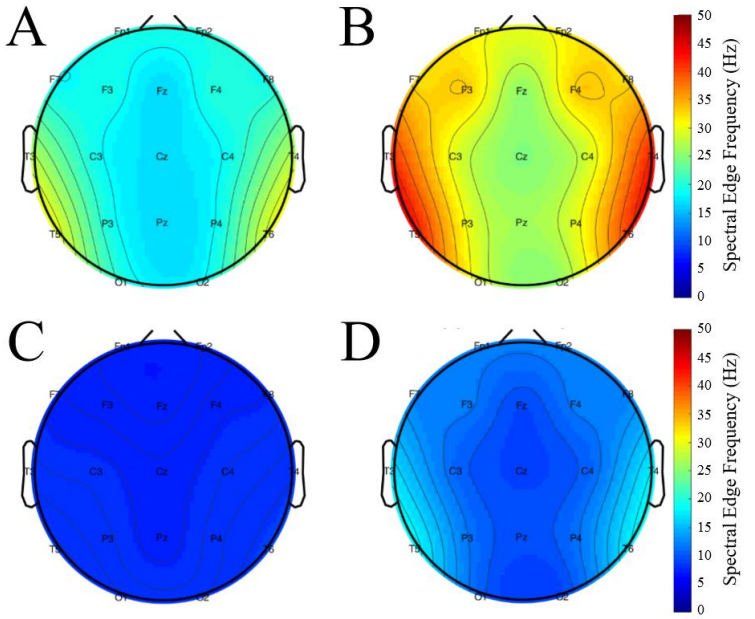

Figure 4.9 Topographic maps of the spectral edge frequency for (A) wake PRE patients, (B) wake CTRL patients, (C) sleep PRE patients, and (D) sleep CTRL patients. The SEF represents the frequency under which 95% of the power resides. Lower values indicate higher power in the lower frequency bands. The SEF is highest in the medial electrodes.

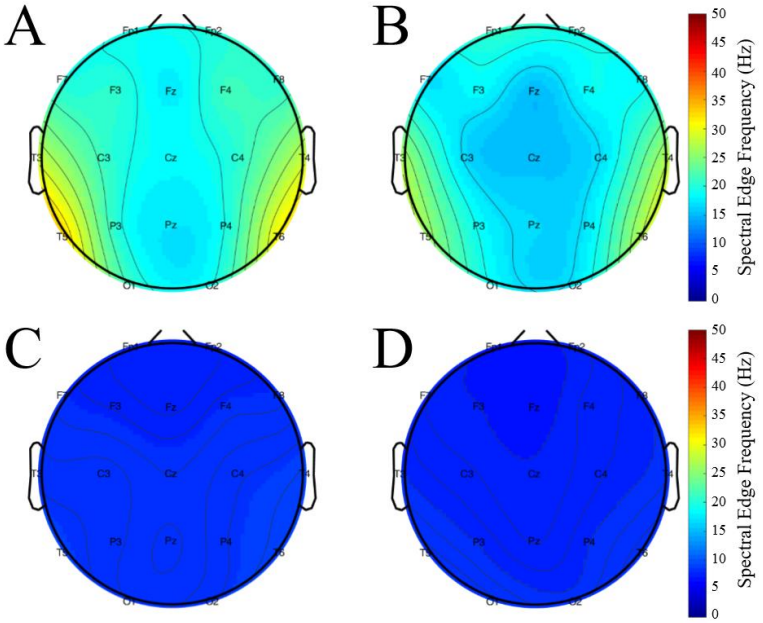

Figure 4.10 Topographic maps of the spectral edge frequency for (A) wake RESP patients, (B) wake NONRESP patients, (C) sleep RESP patients, and (D) sleep NONRESP patients.

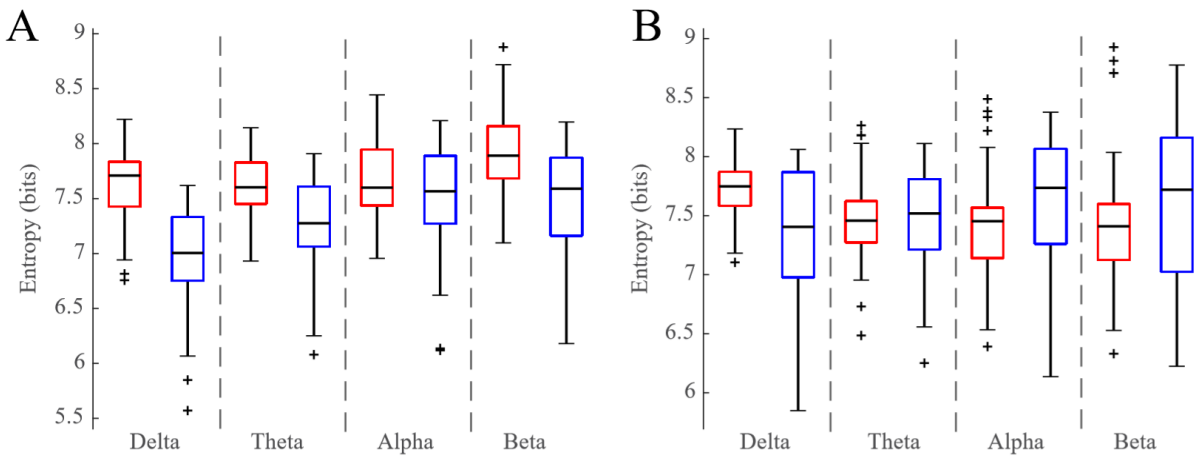

Figure 4.11 Boxplots of the mean Shannon entropy for pre-treatment IS patients (red) and control subjects (blue). Entropy was calculated in every channel and averaged for every patient. Boxplots of the mean entropy values are shown for (A) waking and (B) sleeping data. Entropy is significantly higher in IS in the delta, theta, and beta frequency band during wakefulness and higher in the delta band during sleep.

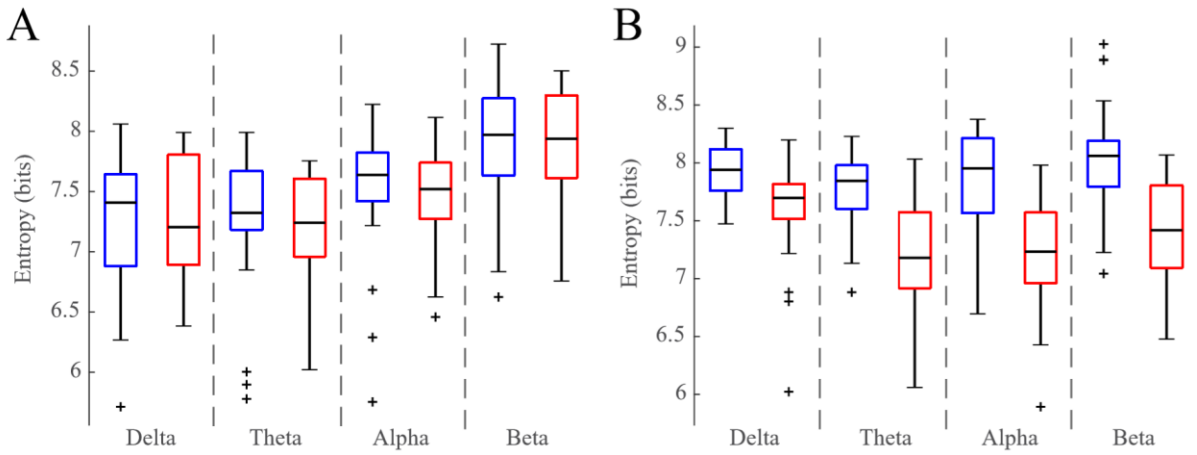

Figure 4.12 Boxplots of the mean post-treatment Shannon entropy for responding patients (blue) and nonresponding patients (red). Boxplots of the mean entropy values are shown for (A) waking and (B) sleeping data. Entropy in the RESP group is significantly higher in all frequency bands during sleep, and the median of the NONRESP group closely matches that of the CTRL group.

4.3.4 DFA differentiates responders and non-responders

We plotted the DFA intercept, β, against the DFA exponent, α for all groups (Figure 4.13 and Figure 4.14). The PRE group exhibited higher β values and slightly lower α values than the CTRL group in all frequency bands (Figure 4.13 and Figure 4.14). We used a logistic regression

classifier with five-fold cross-validation to test the accuracy of the model to new data (Table 4.2). The beta frequency band provided the highest sensitivity for classification of IS data during wakefulness (88%), and the alpha band had the highest sensitivity (86%) during sleep (Table 4.2). The highest specificity was achieved in the delta frequency band for awake data (89%) and alpha frequency band for sleep (89%) (Table 4.2).

TABLE 4.2. Mean sensitivity and specificity in logistic regression classification

	Delta		***Theta***		***Alpha***		***Beta***	
	Wake	**Sleep**	**Wake**	**Sleep**	**Wake**	**Sleep**	**Wake**	**Sleep**
Sensitivity	86%	82%	80%	82%	82%	86%	88%	78%
Specificity	89%	74%	80%	71%	86%	89%	74%	77%

We also investigated whether DFA revealed differences between the RESP and NONRESP groups after treatment. Arrows map the trajectory from pre-treatment values to post-treatment values (Figure 4.15). When the waking post-treatment values were compared with the waking PRE values and CTRL values, the RESP group exhibited significantly higher P_{CTRL} (total number of control data points within ellipse) than the NONRESP group in the delta and theta frequency band (Figure 4.16) (Wilcoxon rank-sum test, corrected via Benjamini-Hochberg procedure, adj. $p<0.05$). In sleep, the P_{CTRL} values were higher in the delta, theta, and alpha frequency bands in RESP when compared to NONRESP (Figure 4.16). The post-treatment $netVal$, defined as $(-P_{ES} + P_{CTRL})$, was significantly higher in the RESP group than the NONRESP group in the theta and beta frequency bands in wake data, while $netVal$ was significantly higher in the theta, alpha, and beta frequency bands in sleep (Wilcoxon rank-sum test, corrected via Benjamini-Hochberg procedure, adj. $p<0.05$). Histograms of the significant distributions are shown for reference (Figure 4.17).

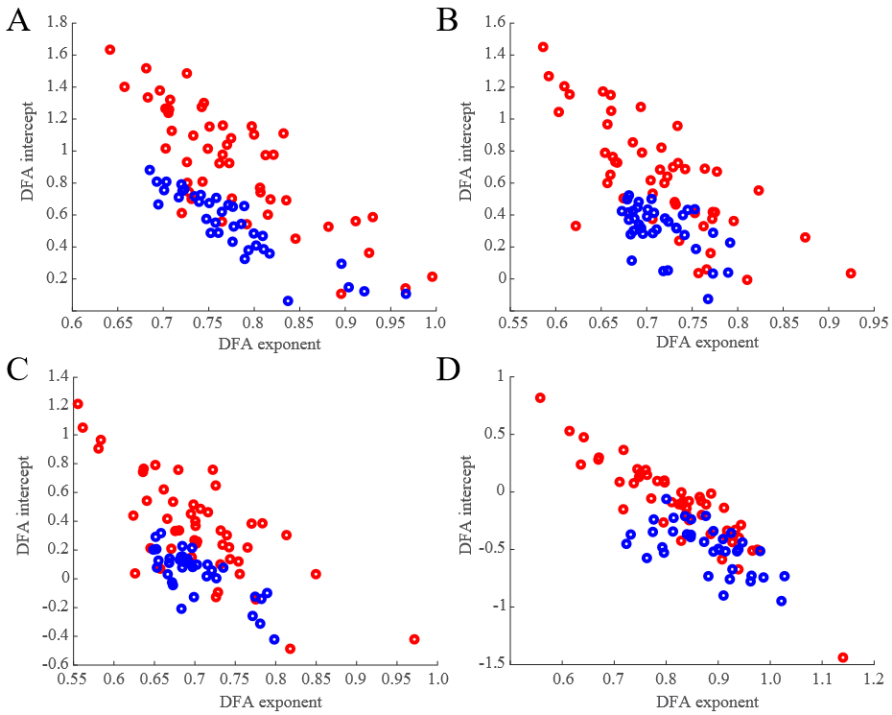

Figure 4.13 Scatterplots of DFA parameters for PRE (red) and CTRL (blue) during wakefulness. Points are plotted at (α_i, β_i) where α is the DFA exponent value and β is the DFA intercept value for patient i. Results are shown for the (A) delta, (B) theta, (C) alpha, and (D) beta frequency band.

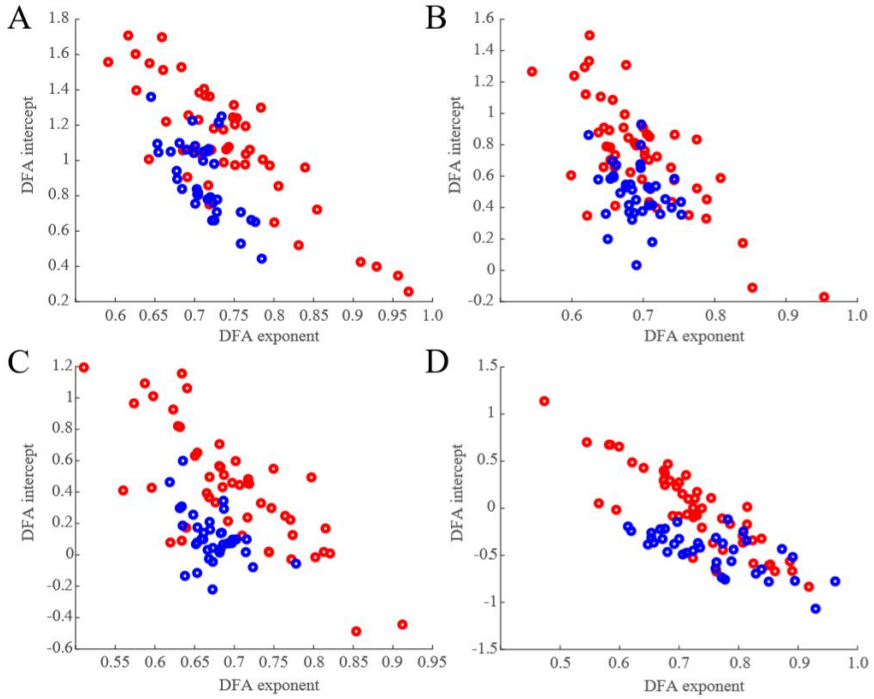

Figure 4.14 Scatterplots of DFA parameters for PRE (red) and CTRL (blue) during sleep. Results are shown for the (A) delta, (B) theta, (C) alpha, and (D) beta frequency band.

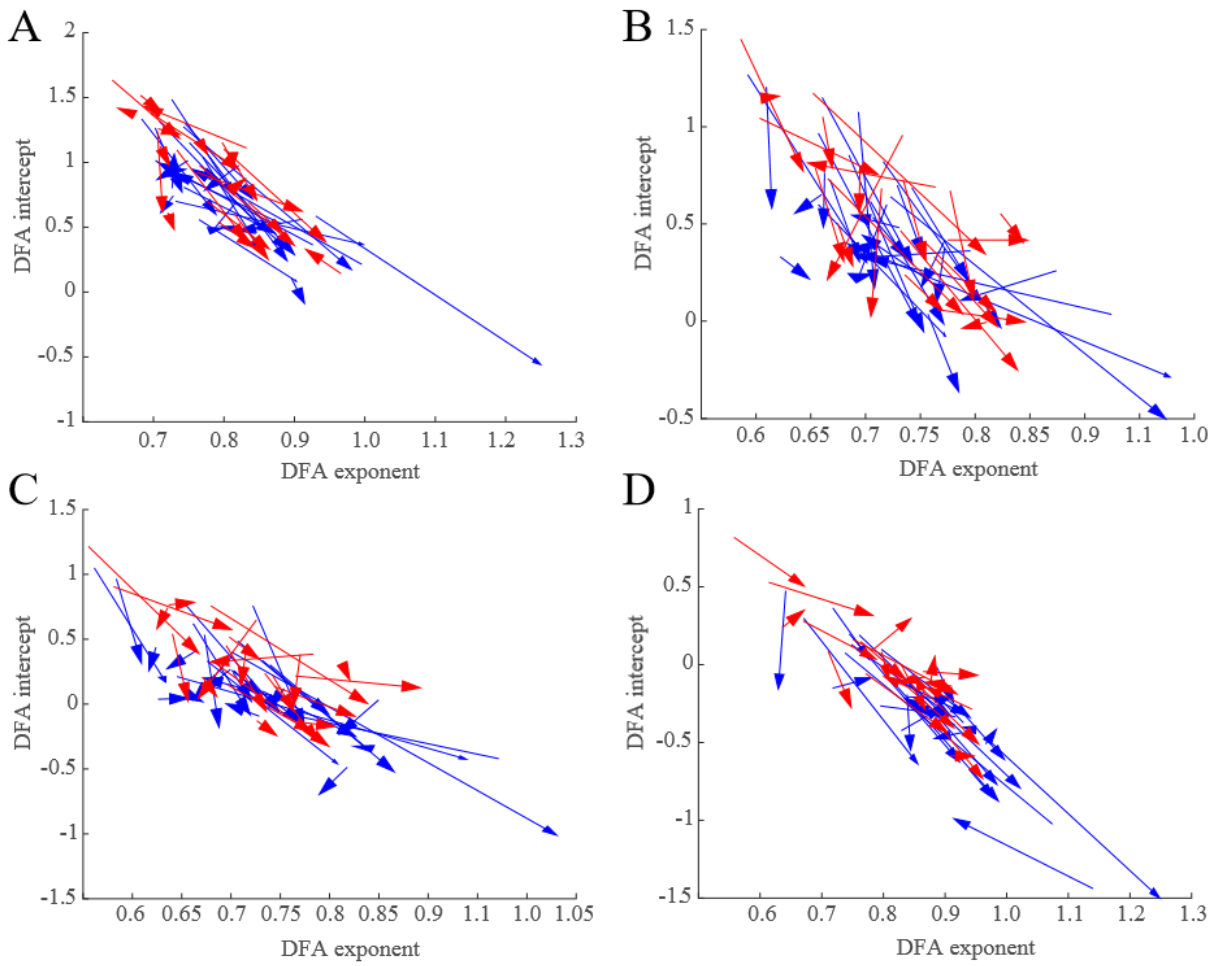

Figure 4.15 DFA response vectors for RESP (blue) and NONRESP (red) during wakefulness. The tail of the arrow corresponds to the pre-treatment DFA parameter values $(\alpha_{PRE_i}, \beta_{PRE_i})$ and the tip of the arrow corresponds to the post-treatment DFA parameter values $(\alpha_{POST_i}, \beta_{POST_i})$ for patient i. Results are shown for the (A) delta, (B) theta, (C) alpha, and (D) beta frequency band.

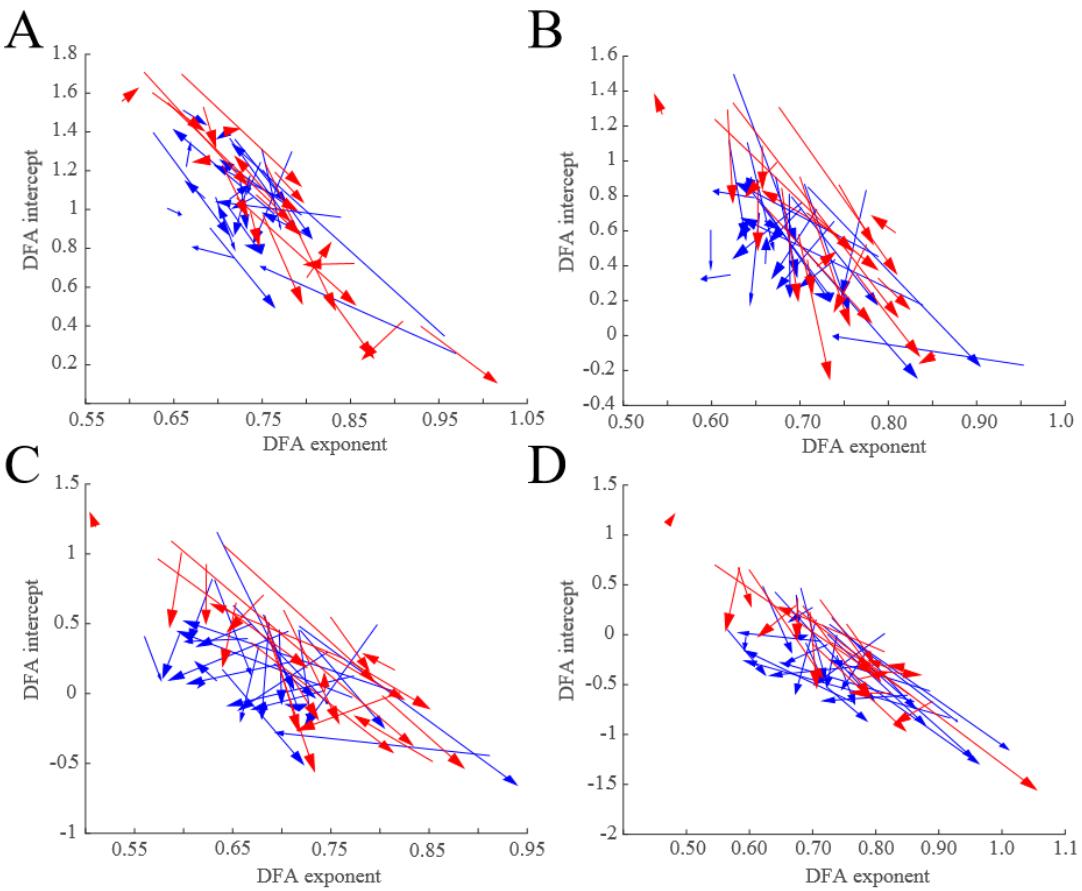

Figure 4.16 DFA response vectors for RESP (blue) and NONRESP (red) during sleep. Results are shown for the (A) delta, (B) theta, (C) alpha, and (D) beta frequency band.

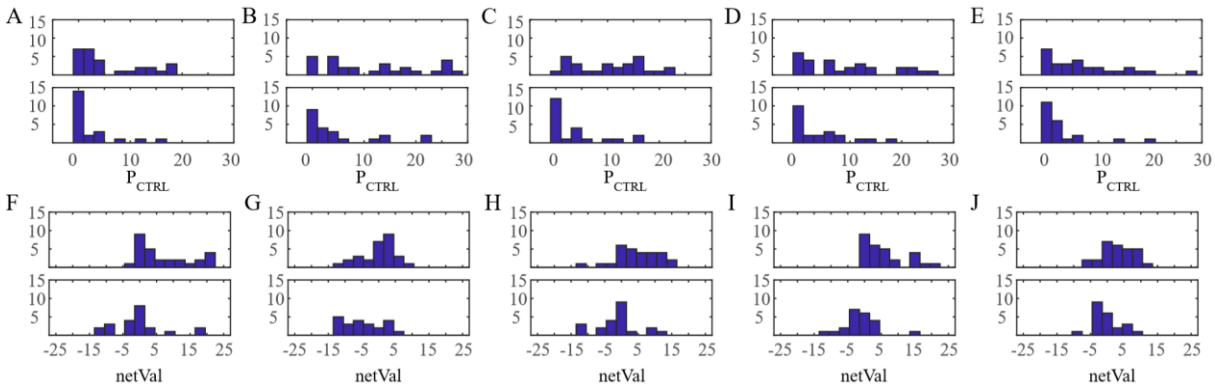

Figure 4.17 Histograms of significantly different P_{CTRL} and $netVal$ values between RESP (top panel of each subplot) and NONRESP (bottom panel of each subplot). Subplots A-E show histograms of significantly different P_{CTRL} distributions, while F-J show all significantly different $netVal$ distributions. (A) Wake delta band, (B) Wake theta band, (C) Sleep delta band, (D) Sleep theta band, (E) Sleep alpha band, (F) Wake theta band, (G) Wake beta band, (H) Sleep theta band, (I) Sleep alpha band, and (J) Sleep beta band.

4.4 Discussion

We quantitatively analyzed EEG in a large cohort of infantile spasms patients and identified several computational EEG markers that differ significantly between infantile spasms patients and control subjects. Several of these metrics reflected a response to treatment despite the refractory nature of the spasms in a large proportion of the patients.

We previously reported amplitude and spectral characteristics in a cohort of new-onset IS patients [168]. In that study, we retrospectively identified 21 IS patients treated at the Children's Hospital of Orange County with varying etiologies, but all patients were of a similar age range (median 6.3, IQR 5.2-8.1 months) and most presented with hypsarrhythmia on the pre-treatment EEG [168]. In contrast to that study, this cohort of IS patients is much larger, was collected from the UCLA Mattel Children's Hospital, includes multiple clips of both awake and sleep EEG, and includes patients from a wider age range (median 11.5, IQR 7.7-20.8 months). Additionally, the metrics were calculated by authors (BAL, DWS, and RJS) who were blinded to the patient groups. Despite these differences in the patient cohort, the amplitude and spectral results were astonishingly consistent [168]. Thus, the differences we have reported in this study are not likely due to the presence of hypsarrhythmia and may have value as general biomarkers of infantile spasms. For example, amplitude is an EEG feature that is often unusually high in IS [8], [42], [69]. Hypsarrhythmia is a high-amplitude pattern, and diffuse slowing is a common feature in both ictal and interictal data [7]. Only eight of the fifty patients in this cohort presented with hypsarrhythmia on the pre-treatment EEG; however, the amplitude characteristics closely match those seen in our previous study [168].

Consistent with the EEG finding of high amplitudes in IS, the EEG power of IS patients was significantly higher than control subjects, especially in the lower frequency bands. This

corroborates the clinical findings of diffuse slowing in the pre-treatment EEG [7]. We noted a unique suppression of activity in the theta frequency band that is present in both responders and non-responders, however the effect is stronger in the responders. In our previous study, patients were most commonly treated with ACTH, unless the specific etiology indicated a different therapy (such as vigabatrin for a primary IS etiology of tuberous sclerosis complex [46], [169], [170]). Vigabatrin and prednisolone were the first-line treatment for patients in this cohort, and we find similar suppression effects on the oscillations in the theta frequency band for all patients, whether they were treated with ACTH, vigabatrin, or prednisolone. Therefore, this suppression of power does not appear to be caused by a specific medication, and it may be an effect of changes in neuronal activity due to treatment response. Whether this effect is seen with all treatments and whether this suppression may have predictive power should be a subject of further study.

Although we only analyzed frequencies up to 30 Hz in this study, it has been noted that fast activity (14-50 Hz) may play an important role in IS [171], [172]. Consistent with prior studies, we found that IS patients exhibit higher power in the faster frequency bands during sleep, and patients that responded to treatment exhibited a suppression of this fast activity during sleep after successful treatment. Even higher frequency ranges (40-150 Hz) may have relevance in IS [173], but the sampling rate of our data precluded this analysis.

Shannon entropy has been reported to be lower in epilepsy patients than healthy subjects. From a nonlinear dynamics perspective, this is because epileptic data often exhibits a lower dimension than control data, as healthy data is more stochastic in nature [103], [163]–[165]. Specifically in IS, it was found that hypsarrhythmia exhibited lower dimension and lower entropy than healthy control data, but the time series was not as nonlinear as seizure data [90]. In

contrast, we found that the entropy values in the delta, theta, and beta band were higher in pre-treatment IS patients than control patients in waking data. Although this corroborates clinical descriptions of a "disorganized" background in the pre-treatment EEG pattern in IS, it contrasts with prior studies of entropy in epilepsy. Further, we found that patients that responded to treatment exhibited higher entropy values than non-responding patients in sleep.

We used detrended fluctuation analysis to compare the temporal structure of the EEG data for IS and control subjects, specifically by measuring power-law scaling and long-range temporal correlations. We previously showed that long-range temporal correlations were weaker in new onset infantile spasms patients when compared with controls, and that the DFA exponent values normalized with successful treatment [91]. We also reported that classification of IS data and control data using a support vector machine achieved up to 90% accuracy in the delta frequency band when the DFA exponent, α, and DFA intercept, β, were used as parameters [91]. We investigated whether these trends were reproducible in this larger cohort of IS patients, which had a higher proportion of refractory cases and longer delays between diagnosis and treatment. As in our previous study, when we plotted the α and β for the PRE and CTRL groups, we noted that the DFA exponent and DFA intercept were negatively correlated with each other. Interestingly, this correlation is not artificial; different features of the signal influence the DFA exponent and intercept independently. The DFA intercept is logarithmically correlated to the variation in amplitude of the signal, whereas the DFA exponent is unaffected by this feature [91]. We performed a five-fold cross validation of a logistic regression model to test its performance in classifying new data. Classification of PRE and CTRL waking data reached 88% sensitivity in the beta frequency band, and classification of PRE and CTRL sleeping data reached 86% in the

alpha frequency band. Specificity was highest in the delta band during wakefulness and in the alpha band during sleep, both achieving 89% specificity.

We analyzed the post-treatment location ($\alpha_{POST_i}, \beta_{POST_i}$) of responders and non-responders in the DFA parameter space and assessed whether that point was closer to the cluster of control patient data points or pre-treatment IS patient data points. The P_{CTRL} and $netVal$ were significantly higher for responder patients in various frequency bands, including theta, during sleeping and wakefulness (Figure 4.17). This indicates that the temporal structure of responder EEG data was more similar to control subjects than pre-treatment spasms patients. Specifically for the theta band results, this could be related to the post-treatment theta suppression revealed in the power spectrum analysis, further supporting that this is an effect of neuronal activity changes in response to treatment. However, a prospective study would be required to test this effect.

The consistency of the results for IS patients across wide ranges of ages, etiologies, and severity (new onset vs. refractory) indicate that these characteristics of the EEG may be specific to infantile spasms. As lead time is one of the most predictive prognostic factors in these children, stable metrics that quantify disease burden despite long lead times are incredibly important diagnostically. Further, we show that these metrics reflect response to treatment, suggesting they may be used in clinical treatment assessment. We believe these metrics, in conjunction with other clinical tools, may benefit clinicians in their diagnostic and treatment decision-making.

CHAPTER 5

TEMPORALLY-EVOLVING FUNCTIONAL CONNECTIVITY NETWORKS in INFANTILE SPASMS

5.1 Functional connectivity networks in infantile spasms

5.1.1 Introduction

The brain is an incredibly complex, nonlinear dynamic system. Some estimate this system to be a network of around 10^{10} neurons, with each neuron communicating with around 10^4 other neurons [174]. From the level of scalp EEG, these communicating potentials are detected from synchronous, summed activity of large groups of neurons. Functional connectivity is defined as temporally coherent interactions between these groups of neurons, whether or not they are directly anatomically connected [175], [176].

Epilepsy has come to be understood as a disorder of pathological brain networks [177], which can be assessed using computational measures of functional connectivity [178]. However, such studies are relatively rare in the pediatric epilepsy population. One study of EEG-based functional networks in newly diagnosed childhood epilepsies reported a loss of network integration in focal epilepsies in the delta frequency band [179]. However, they also noted that generalized epilepsies overall maintained their functional connectivity structure, sparing the degradation of the network that was disrupted in focal epilepsies [179]. In Lennox-Gastaut syndrome, an EEG-fMRI study showed persistently abnormal functional networks and hypothesized the lack of functional integration influenced the cognitive deficits associated with the disease [180].

Studies in infantile spasms support the theory that very different mechanisms underlie hypsarrhythmia and spasms in comparison to other childhood epilepsies. Our previous work revealed stronger EEG-based functional connections in infantile spasms than in controls when measured with cross-correlation [80]. That study also showed that the network structure is more integrated, with more long-range connections than control subjects [80]. This is consistent with previous findings using EEG coherence in patients with IS, in which stronger connectivity was found in long-range connections and weaker connectivity at short electrode distances [81]. A dual EEG-fMRI study implicated deeper anatomical structures in the generation of hypsarrhythmia by correlating the slow wave activity to the hemodynamic responses in the putamen and brainstem. They further correlated the multi-focal independent spikes to the BOLD oscillations on the cerebral cortex, revealing the upstream and downstream pathological events that generate these abnormal EEG patterns [84]. A study of directed coherence as a measure of functional connectivity found that the occipital lobe was the source of high amplitude delta power in patient with IS [85]. They correlated their connectivity findings with EEG-fMRI data from the same cohort of patients to reveal similar pathological pathways of aberrant activity from the brainstem and putamen and thalamus [84], [85].

We investigated whether functional connectivity measured with cross-correlation in a cohort of IS patients with a high proportion of refractory cases corroborated previous findings in new-onset patients [80]. This study included a large number of subjects, both awake and sleep EEG data, and multiple clips per subject. Consistency between the networks in these two groups could imply that functional connectivity networks are a robust marker of disease.

5.1.2 Methods

5.1.2.1 EEG data collection and pre-processing

EEG data from IS patients and control subjects were retrospectively identified and clipped as described in Section 4.2.1.

Two clips during wakefulness and two clips during sleep were extracted from the control subject recordings and both pre- and post-treatment recordings in IS patients. Each clip contained approximately 20-30 minutes of EEG data. We calculated functional connectivity for both clips during wakefulness and during sleep and averaged the two awake matrices and two sleep matrices for each patient to obtain one matrix for wakefulness and one matrix for sleep.

Connectivity was computed on each clip while the authors (BAL, DWS, RJS) were blinded to the patient groups, clip numbers, and designation of wakefulness or sleep and pre- or post-treatment. After the computational analysis, the data were unblinded and grouped as follows: All data from the IS patients before treatment were designated as the PRE group (n=50 patients) and subjects from both the IS control group and the non-IS control group were combined into the CTRL group (n=37). After treatment, IS patients that responded to treatment (defined as a resolution or absence of hypsarrhythmia, cessation of spasms, and no clinical relapse over the next 28 days) were included in the responder (RESP) group (n=28 patients). The patients that did not meet one or more of these requirements after treatment were included in the non-responder (NONRESP) group (n=22 patients).

Time periods in the EEG containing artifact were marked using an automatic detection algorithm (see Appendix A). The algorithm first broadband bandpass filtered the data (1.5-40 Hz, butterworth filters). The mean was subtracted from each channel, and the standard deviation was calculated from the zero-mean time series. Then time points where the absolute value of the voltage exceeded a threshold of 7.5 standard deviations above or below the mean value in any

single channel were marked. A buffer of 0.9 seconds was added to both sides of the marked extreme amplitude values to ensure that the entire artifact was marked. Data recorded during EEG impedance checks were also identified and marked. This method of artifact detection was comparable to visual detection of artifacts when assessed with the metrics described in this study, with an average of 91% concordance.

Data were sampled at 200 or 500 Hz, with impedances below 5 kΩ, and re-referenced to the common average. We broadband bandpass-filtered the re-referenced data from 0.5-55 Hz. Artifactual segments of data were excluded from all channels, even if the artifact occurred in a single channel.

5.1.2.2 Functional connectivity

Functional connectivity measures the correlation between electrophysiological signals in two different brain regions. We calculated functional connectivity networks via cross-correlation using the method developed by Kramer et al. [181] and Chu et al. [176] and previously applied to IS EEG data in [80]. The algorithm is briefly described below:

Data were divided into one-second epochs and normalized to have zero-mean and unit variance. We calculated the cross-correlation between every pair of channels within the window and identified the time lag associated with the maximum of the absolute value of the cross-correlation. Windows in which the cross-correlation value was maximal at zero time lag were removed to control for volume conduction [176]. A partial correlation with the common-average reference time series was performed to test whether the reference induced the correlation measured between the channels [80]. If the difference between the partial correlation, accounting for the reference, and the correlation value between the channels was greater than 0.25, the epoch

was removed from further analysis. Z-values were calculated by dividing the Fisher-transformed correlation coefficient value by the estimated standard deviation, taking the autocorrelation of each channel epoch into account [176], [181]. The z-values were compared to a baseline distribution created via permutation resampling. Permutation resampling was performed by selecting 1000 one-second epochs of data from the time series that were at least one second away from the epoch of interest and calculating the correlation between the channel of interest to all other channels in the new epoch [182]. The standardized correlation values from all iterations were sorted and the threshold of significance was defined as the value corresponding to the 95^{th} percentile of the distribution for each electrode pair. For each epoch, correlation values between channel pairs that exceeded this threshold value were deemed to be a significant connection. The overall connection strength between two channels is calculated as the fraction of time series epochs in which there was a significant connection between them.

Statistical tests were performed on the distributions of channel pair connections. A Wilcoxon rank-sum test identified whether distributions of connections for each channel pair were significantly different between PRE and CTRL groups or RESP and NONRESP groups. P-values were corrected via the Benjamini-Hochberg procedure to adjust for multiple comparisons.

5.1.3 Results

Overall, the strength of EEG-based functional connections was higher during sleep than wakefulness. The PRE group exhibited significantly stronger connections than the CTRL group in 125 of the 171 possible connections (73.1%) during wakefulness, and in 133 of the 171 possible connections (77.8%) during sleep (Figure 5.1) (one-tailed Wilcoxon rank-sum test, corrected via Benjamini-Hochberg procedure, adj. $p<0.05$). Specifically, cross-hemispheric long-

range connections were present in the PRE group during wakefulness that were absent in the CTRL group (Figure 5.1).

After treatment, the RESP functional connectivity map decreased in strength more than the NONRESP group and more closely resembled the CTRL group (Figure 5.2). However, when we analyzed the group distributions, only 2 electrode pair connections were significantly different between the RESP and NONRESP group in the sleep data and none were significantly different in the waking data (one-tailed Wilcoxon rank-sum test, corrected via Benjamini-Hochberg procedure, adj. $p<0.05$).

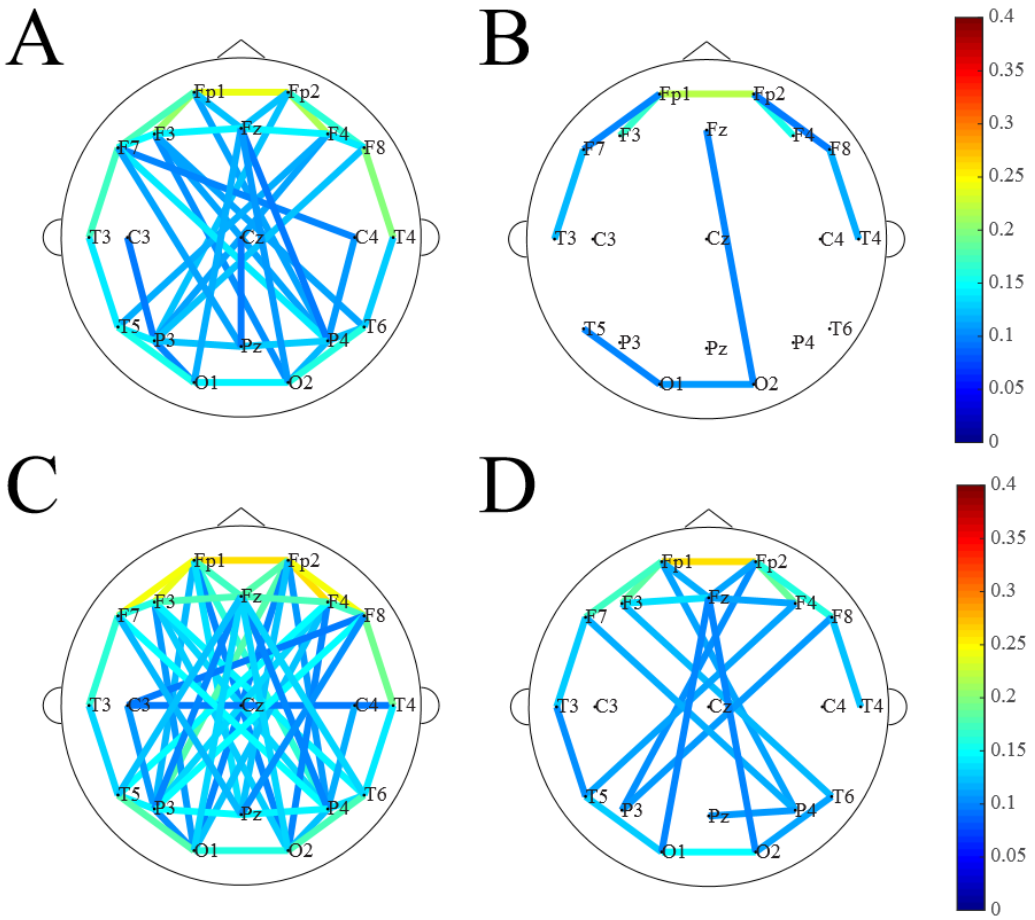

Figure 5.1 Functional connectivity maps for (A) wake PRE group, (B) wake CTRL group, (C) sleep PRE group, (D) sleep CTRL group. Functional connectivity was assessed in one-second epochs, and overall connection strength is calculated as the proportion of significant one-second epochs in the recording. For visualization, graph edges are displayed if the connection strength between two electrodes exceeded 0.1.

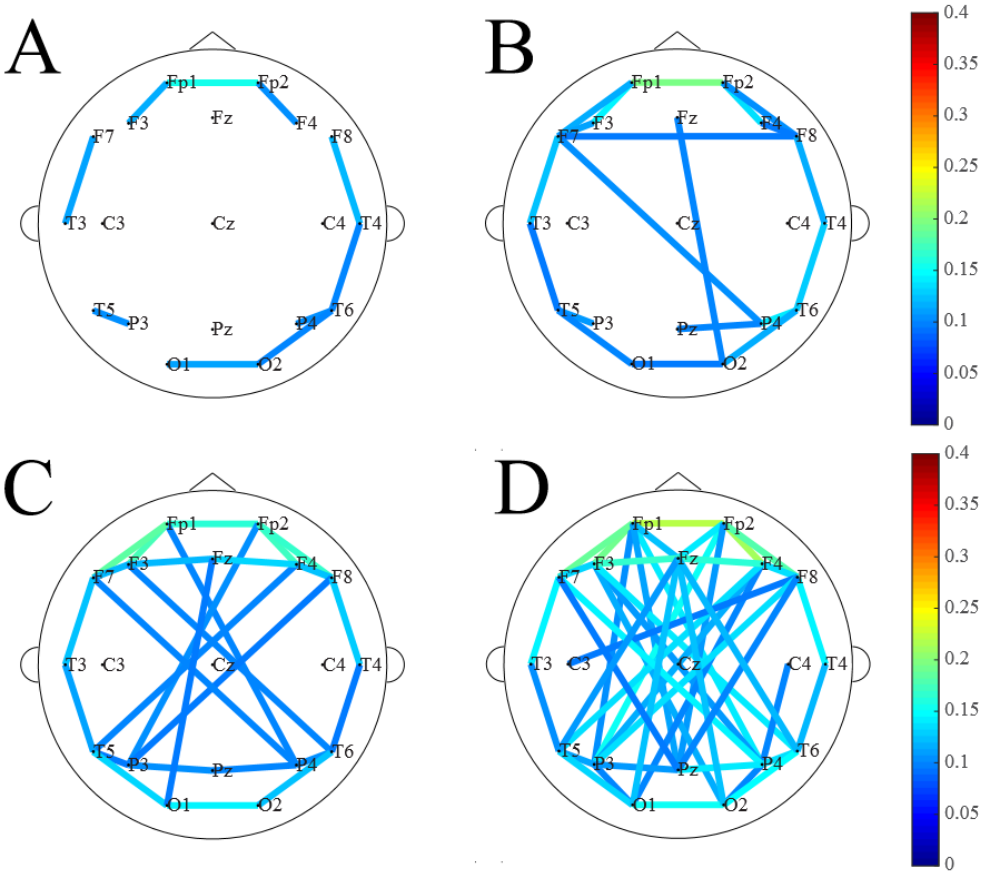

Figure 5.2 Functional connectivity maps for (A) wake RESP group, (B) wake NONRESP group, (C) sleep RESP group, (D) sleep NONRESP group. For visualization, graph edges are displayed if the connection strength between two electrodes exceeded 0.1.

5.1.4 Discussion

The EEG patterns in IS have been hypothesized to be sub-cortically driven [80], which motivated our analysis of functional connectivity. Indeed, studies with SPECT [82], PET [83], fMRI [84], and source localization [85] found that subcortical-cortical interactions may play a role in the development of IS [82]. This would also explain how generalized abnormal EEG patterns are observed despite focal etiologies. We assessed functional connectivity with cross-correlation, which has been shown to reveal stable, patient-specific networks in healthy subjects [176] as well as IS patients [80]. Previously, long-range, cross-hemispheric connections were

observed in IS patients both with coherence [81] and cross-correlation [80]. We found that functional connectivity network strengths were higher in IS in most channel pairs, and we observed more long-range cross-hemispheric connections in IS when compared with controls, corroborating previous work [80], [81]. After treatment, the mean connectivity maps were stronger for non-responding patients when compared with responders, but this was not significant when we assessed the group distributions. Across all subject groups, the functional connections were stronger during sleep than wakefulness.

5.2 Temporal changes in functional connectivity in infantile spasms

5.2.1 Introduction

In Section 5.1, we showed that functional connectivity networks reflect disease burden and change in response to treatment over the course of two to four weeks. However, the time course of this change during the treatment period is unknown. Because such computational measures can detect subtle EEG changes that may not be visually apparent, we hypothesized that the strength and structure of the functional networks may provide an early biomarker of treatment response. To test this, we must first understand normal physiological changes in these networks. The brain's connectivity network is individualized and stable over periods of hundreds of seconds [80], [176], but also changes drastically with falling asleep and waking up in the context of the 24-hour circadian rhythm [183] (Figure 5.1 and 5.2). Mapping these changes will enable us to separate normal physiological changes from those associated with a response to treatment, and this could advance treatment assessment and even predict treatment outcome in these high-risk patients.

To address this question, we prospectively recorded EEG data from a large cohort of infants, each with long-term video EEG monitoring over 24 hours in length. The cohort included some patients diagnosed with infantile spasms and some that were neurologically normal. We calculated metrics of functional connectivity, namely the network strength and stability, to assess how these characteristics evolve over the course of hours and days.

5.2.2 Methods

5.2.2.1 Patient recruitment and EEG recording

We identified and recruited patients as follows: First, we ensured that patients meeting inclusion criteria whose parent(s)/guardian(s) enrolled them in the study continued to receive the standard of care for new onset infantile spasms. At CHOC, the standard work-up for newly diagnosed infantile spasms includes inpatient consultations from neurology, metabolics, and genetics, long-term video EEG monitoring to capture their events of concern (suspected seizures) and characterize their baseline EEG activity, laboratory testing (blood, urine, and sometimes CSF), neuroimaging (typically MRI with and without contrast, though sometimes CT is utilized), and occasionally a diagnostic lumbar puncture. ACTH is the first line treatment for patients with infantile spasms at CHOC, and this medication is started immediately upon diagnosis while the order for outpatient treatment is processed. The patient remains in the hospital for roughly two days in order for (1) their parent(s)/guardian(s) to learn how to give intramuscular injections to administer the medication, (2) their initial laboratory testing to be completed, and (3) their home supply of ACTH to be delivered. During this time period, patients who were enrolled in our study continued to have long-term video EEG monitoring performed until at least 48 hours after treatment initiation or until they were discharged from the hospital, whichever came first. EEG electrodes were continually assessed by the EEG techs per routine care.

The specifics of the recording setup were as follows: when a patient was placed on long-term video EEG monitoring with concern for infantile spasms, their parent(s)/guardian(s) were approached to consider the patient's enrollment in this study. If they provided informed consent, the patient's EEG was recorded concurrently by two separate systems: (1) the standard clinical setup used at CHOC for long-term EEG monitoring, and (2) a secondary research system that recorded the same data to a research computer that was disconnected from the CHOC server and recorded at a much higher sampling rate than the clinical machines (5,000 Hz vs 1,000 Hz).

If the initial EEG recording led to a diagnosis of infantile spasms, the research video EEG recording continued for at least 48 hours following initiation of treatment with ACTH, regardless of the status of the clinical video EEG recording. If the patient was ready to be discharged from the hospital before the 48 hours elapsed, the research recording was stopped, as it could not delay the patient's discharge. The recording was also stopped if necessary for a medical indication. Clinical data pertinent to the study was obtained by a study investigator. Patients diagnosed with infantile spasms who were enrolled in this study repeated long-term video EEG monitoring approximately 2 weeks following treatment initiation to evaluate their treatment response as part of their standard care. At that time, their repeat video EEG and follow-up clinical data were collected. Further follow-up data collection occurred at 3, 12, and 24 months following study enrollment.

If the patient was not diagnosed with infantile spasms, the research video EEG recording continued as long as the clinical video EEG recording was running. Clinical data was collected at the time of enrollment. After this data collection and video EEG recording were completed, no further follow-up data was directly collected from the patient/parent(s)/guardian(s). Additional data was collected retrospectively from the electronic medical record at 3, 12, and 24 months after enrollment.

Patients were subdivided into 1) IS patients, which were those diagnosed and treated for IS, 2) diseased controls who were not diagnosed with IS but were confirmed to have other seizures/neurological abnormalities, and 3) healthy controls, which were subjects who did not receive a diagnosis of IS and had no discernable neurological abnormalities or developmental delay. In total, we recorded long-term EEG from 13 IS patients, 17 diseased controls, and 27 healthy controls. The number of datasets analyzed in each group is described in Section 5.2.2.3.

5.2.2.2 EEG Pre-processing

The low sampling rate EEG recordings were used for this analysis of functional connectivity. Artifactual time periods were identified with an automatic artifact detector as described in Section 5.1.2.1 (see also Appendix A). Data were sampled at 200 Hz with impedances below 5 kΩ and were re-referenced offline to the common average. A broadband bandpass-filter was applied to the re-referenced data (0.5-55Hz). Signal epochs that were identified as artifactual were removed after filtering.

5.2.2.3 Time-varying functional connectivity measurement

Connectivity was calculated in one-second epochs as described in Section 5.1.2.2. Let p represent the number of EEG channels used in the calculation. Then the output of the connectivity calculation is a binary matrix of dimension $p \times p$ for each epoch, where the element at position (i, j, k) represents the connection between electrode i and electrode j in epoch k. This element is assigned a value of 1 if the connection is significant and a value of 0 if the connection is not significant (see Section 5.1.2.2 for significance testing). To assess time-varying changes in the functional connections, we averaged the binary $p \times p$ matrices across a window of 300 successive epochs, and the window was shifted over time with 90% overlap (i.e. 30-second shift). Let Q_{avg} represent the $p \times p$ matrix averaged from a 300-second window. The value in position (i, j) of Q_{avg} indicates the proportion of epochs in which the connection between channel i and channel j was significant, e.g. a value of 0.3 indicates that channel i and channel j were significantly correlated in 30% of the epochs. We chose a window size of 300 seconds

because networks were shown to be stable over this amount of time in two separate studies [80], [176].

5.2.2.4 Network separation into two states

In order to describe how functional connectivity networks evolve over time and between brain states, we needed to separate awake data from sleep data. The analysis of such a young patient population added an interesting element to this study, as the infants fell asleep and woke up on shorter time scales than adults, and their sleep/wake cycles did not follow circadian rhythms as closely as adults.

We separated the networks into two states by performing principle component analysis (PCA) on the functional connectivity profiles over time. We calculated Q_{avg} in 300-second windows with 90% overlap (i.e. 30-second shift), as described in Section 5.2.2.3. Q_{avg} was a symmetric matrix of dimension $p \times p$. Let n represent the number of successive windowed epochs. We first made a column vector of all independent channel connections in Q_{avg} (171 channel pair connections in total) and then concatenated n successive columns. The connectivity values were normalized to zero mean across time by calculating the mean of each column and subtracting it from each value in that column. We then subtracted the mean of each row from each value, so that the distribution of connections for each channel pair were zero-mean. Next, we calculated the standard deviation of each column and divided each value in the column by this value, so the matrix had unit variance in time. We performed PCA on the normalized functional connectivity time series to ascertain principle components, or latent features, that described the most variance in the data. We then calculated the time course of the first principle

component, which represents the relative weight assigned to that component as a function of time. We often found that the time course of the first principle component would oscillate between two values (Figure 5.3), theoretically representing two different brain states. To characterize this, we fit a two-component gaussian mixture model (GMM) to the principle component time series to determine gaussian parameters for these two states (Figure 5.3).

To verify that the data was best described by a two-state model, we calculated the percentage of overlapping area between the normalized probability distribution functions (PDF) of the two distributions. If the percentage of overlapping area was too high (>20%), we discarded the dataset due to insufficient confidence in the separation of states. For all other datasets, we assumed that the distribution of the first principle component was bimodal in nature and accurately modeled by two states.

The threshold to separate the states was defined as the intersection of the two probability density functions (PDFs) of the GMM distributions. To avoid finding intersections at the tails of the distributions, we calculated the PDF ratio and identified the index where this ratio was closest to 1:

$$thresholdIndex = \min\left(abs\left(\frac{PDF_1}{PDF_2} - 1\right)\right)$$

The principle component value assigned to this index became the threshold to distinguish between the two states.

We hypothesized that the two states would correspond to wakefulness and sleep. Thus, we visually classified sections of EEG data from each of the GMM distributions to label one as awake and the other as sleep.

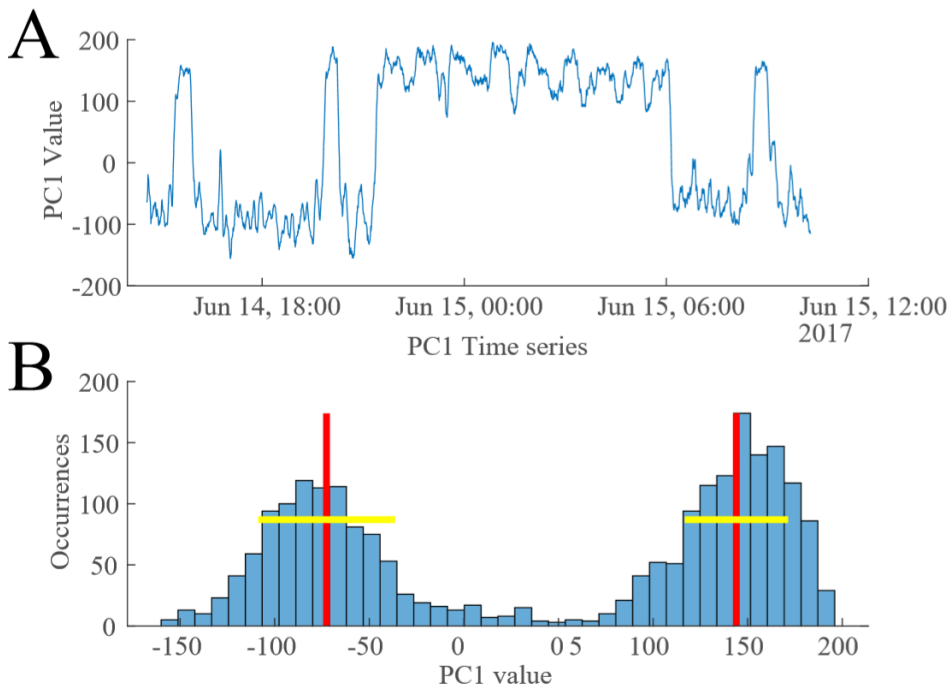

Figure 5.3 Time course of the first principal component (PC1), reflecting how much weight is assigned to the first principal component in the functional connectivity time series. (A) PC1 oscillates between two states, as reflected in (B) the histogram of PC1 values. A two-component Gaussian mixture model was derived from these values and used to classify the two states.

We validated the correspondence of these two states to sleep and wakefulness using data from two control patients and one infantile spasms patient for whom we had visually-marked sleep stages. In the infantile spasms patient, the PCA/GMM classification correctly identified awake data with a sensitivity of 92% and a specificity of 86%. The accuracy was 89%. In the control patients, the average sensitivity for awake data was 87.8%, and sensitivity of sleep data was 99.3%. An example plot of visually-determined sleep stages versus the PCA/GMM automatic classifications is shown in Figure 5.4. These results confirm that the two states extracted via principle component analysis corresponded to wakefulness and sleep. We performed all further analyses on sleep and awake states after classification with this method.

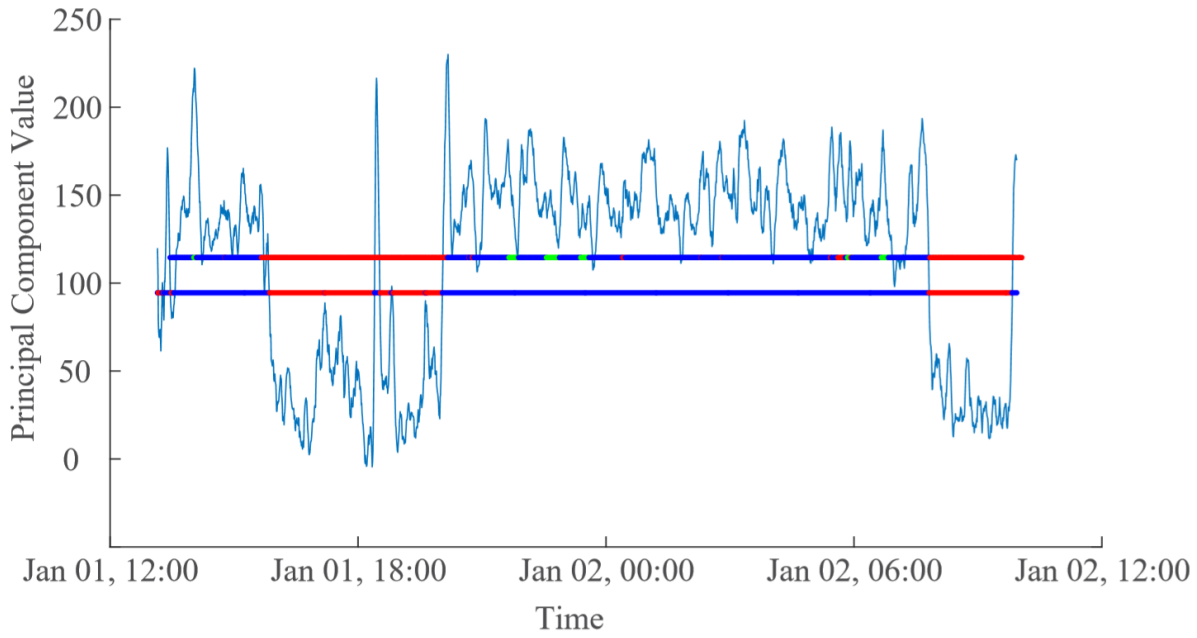

Figure 5.4 Automatic classification of two states from the time series of the first principal component matches visually-classified sleep stages with over 95% accuracy. The top horizontal line is colored to indicate the sleep state. Red indicates the patient is awake, blue is non-REM sleep, and green is REM sleep. The bottom horizontal line reflects the automatic classification of sleep states, with red representing wakefulness and blue representing sleep. For sensitivity, specificity, and accuracy calculations, REM was classified as sleep.

After exclusion of datasets due to insufficient separation of sleep and wakefulness, there remained 35 IS patient datasets, 19 diseased control datasets, and 22 healthy control datasets. We note that the IS patients and diseased controls each had multiple EEG recordings, collected for diagnosis, treatment assessment, and follow-up, so the number of unique subjects is lower than the number of datasets provided above.

5.2.2.5 Sum of strong connections calculation

We analyzed the changes in functional connectivity strength over time. To calculate the overall strength of the network, we summed the number of connections within Q_{avg} that exceeded a threshold of 0.1 (significantly connected in over 10% of all epochs). We chose this

method because the mean and median connection values tend to be skewed by the large number of weak connections with strengths at chance levels [80].

5.2.2.6 Circadian rhythm variation calculation

We assessed how the strength of the functional connectivity networks varied as a function of the time of day. We calculated the sum of the strong connections for each Q_{avg} (as described in Section 5.2.2.5) and recorded the summed strength as a function of the time of day according to the starting datetime of each 300-second epoch. For visualization, the mean of all subject connection strengths for each datetime point was plotted as a function of the time of day.

5.2.2.7 Calculation of network stability

We assessed stability of the connectivity networks by performing 2-dimensional correlations between independent averaged connectivity networks. For a given window size M and dataset length of N seconds, the binary one-second $p \times p$ matrices were averaged in each sequential set of M epochs to created N/M independent measurements of averaged connectivity values. For each window size M, a 2-D correlation was calculated between all independent measurements with the MATLAB function "corr2()". M ranged from 10 seconds to 200 seconds, and the mean and standard deviation of the 2-D correlation coefficient values were plotted as a function of M.

5.2.3 Results

5.2.3.1 Higher connection strengths in sleep EEG data

We first compared the network strengths during sleep and wakefulness in IS patients, diseased controls, and healthy controls (Figure 5.5). In all three groups, sleep data exhibited stronger connectivity than awake data (Wilcoxon rank-sum test, $p<0.05$). Network strengths for sleep and wakefulness were most stratified in the healthy controls and least separated in the IS patients; however, the differences were statistically significantly different in all patient groups (Wilcoxon rank-sum test, $p<0.05$) (Figure 5.5). Additionally, the distributions of strength values for IS patients were statistically significantly higher than diseased controls and healthy controls during both sleep and wakefulness (Wilcoxon rank-sum test, $p<0.05$).

5.2.3.2 Circadian rhythms affect sleeping and waking connectivity strengths

After we verified that the functional connectivity network strengths were significantly different between awake and sleep data, we investigated whether the time of day affected the network strength, i.e. does a sleep period at 2:00 AM have different network strength than a sleep period during a nap at 2:00 PM?

We calculated the network strength as the sum of strong (>0.1) connections in Q_{avg} for each patient dataset, recorded the network strength value as a function of the time of day at which Q_{avg} began, and averaged these values across all patient datasets. In all patient groups, the awake networks had lower mean network strengths (Figure 5.6 A-C) than the sleep networks (Figure 5.6 D-F), corroborating the results from Section 5.2.3.1. However, we note that both awake and sleep data also show higher connectivity strengths during the night (10:00 PM (20:00) to 8:00AM) and lower connectivity strengths during the day (8:00 AM to 8:00 PM (20:00)) (Figure 5.6). This circadian effect was most disrupted in the IS cases and the diseased controls (Figure 5.6A, B, D, and E).

5.2.3.3 Stronger network stability in sleep and in IS patients

We assessed the temporal stability of the networks by computing the 2-D correlation between connectivity networks averaged over a fixed window size within a given sleep/wake stage. For each patient dataset, we iterated this process for window sizes ranging from 10 to 200 seconds. We then plotted the mean correlation coefficient of the group as a function of the window size (Figure 5.7).

Functional connectivity networks measured during sleep exhibited higher network stability than awake data in all patient groups (Figure 5.7). There was greater separation between sleeping and waking network stability in the diseased and healthy controls than the IS patients (Figure 5.7). There was no overlap in the 95% confidence intervals for the mean of the two distributions beyond a window size of 20 seconds for all groups.

Additionally, IS patients exhibited stronger network stability than both healthy and diseased controls in awake data, as the 95% confidence intervals for these groups do not overlap (Figure 5.8A). The network stability was similar for healthy and diseased controls during wakefulness (Figure 5.8A). The sleep network stability was similar for all groups, with no significant differences detected (Figure 5.8B).

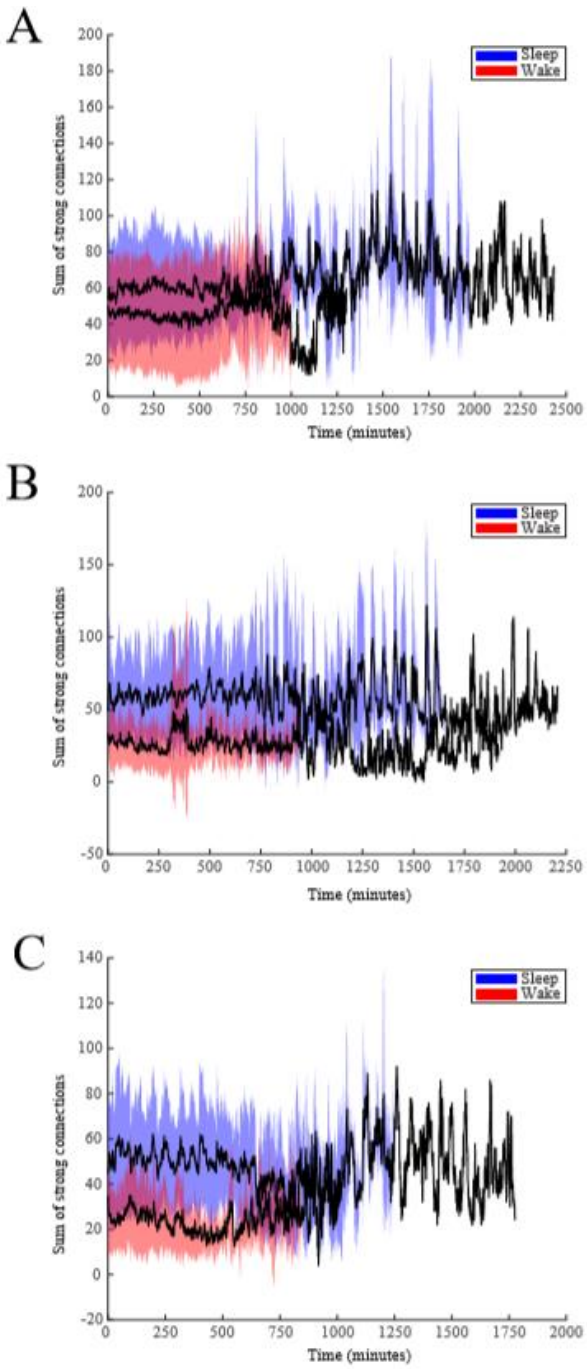

Figure 5.5 Connection strength over time for awake and sleep data for (A) IS patients, (B) diseased controls, and (C) healthy controls. Periods of wakefulness or sleep that were at least ten minutes in duration were concatenated and the strength was assessed across the concatenated time series. The black line represents the mean of the patient distribution and the shaded area represents one standard deviation.

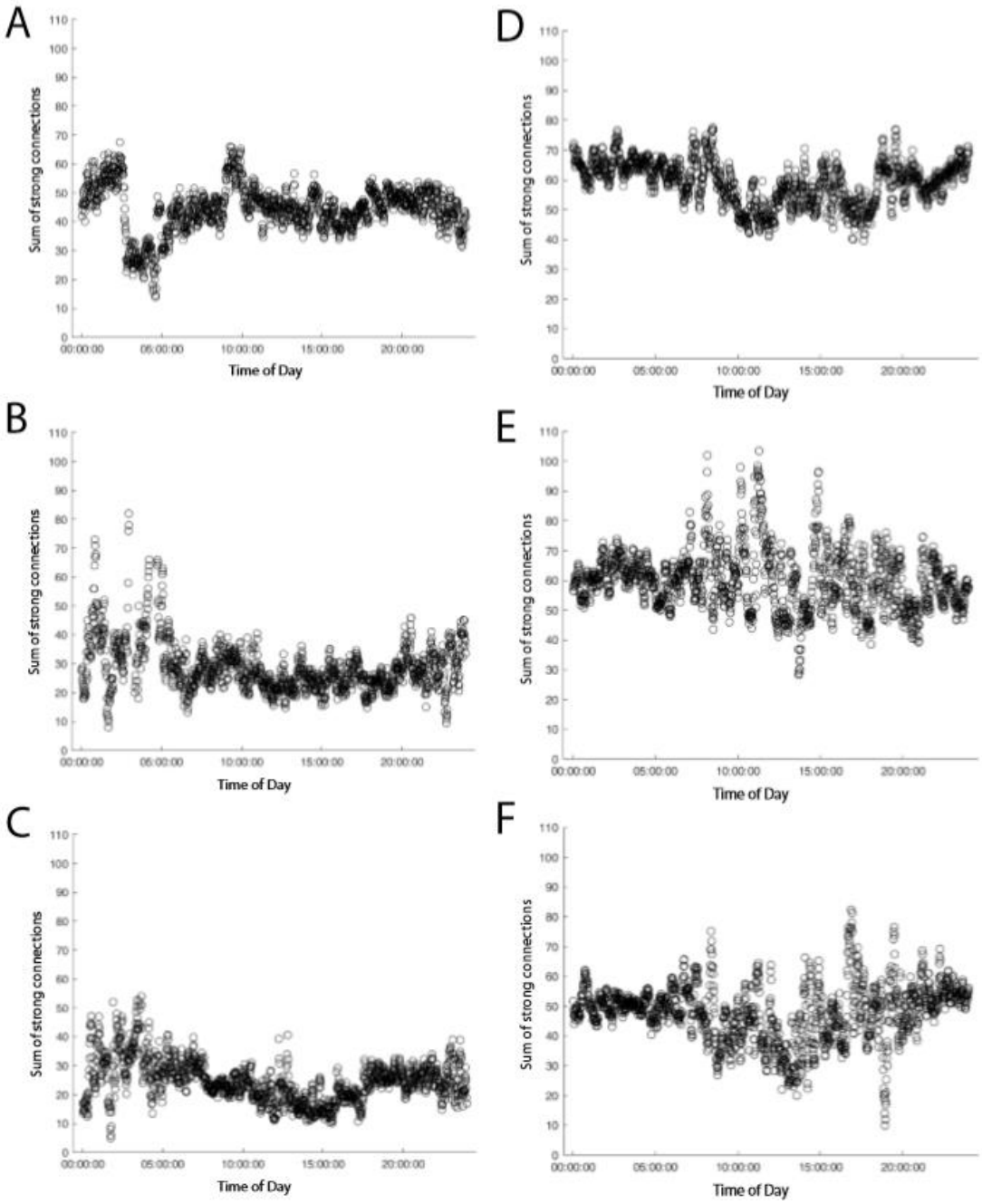

Figure 5.6 Circadian changes in connection strength. We separated the data into sleep and awake data via the automatic separation method. We calculated the network strength in each dataset and recorded it against the starting datetime of each 300-second epoch. The mean of all network strengths is plotted as a function of the datetime for (A) awake periods in IS patients, (B) awake periods in diseased controls, (C) awake periods in healthy controls, (D) sleep periods in IS patients, (E) sleep periods in diseased controls, and (F) sleep periods in healthy controls.

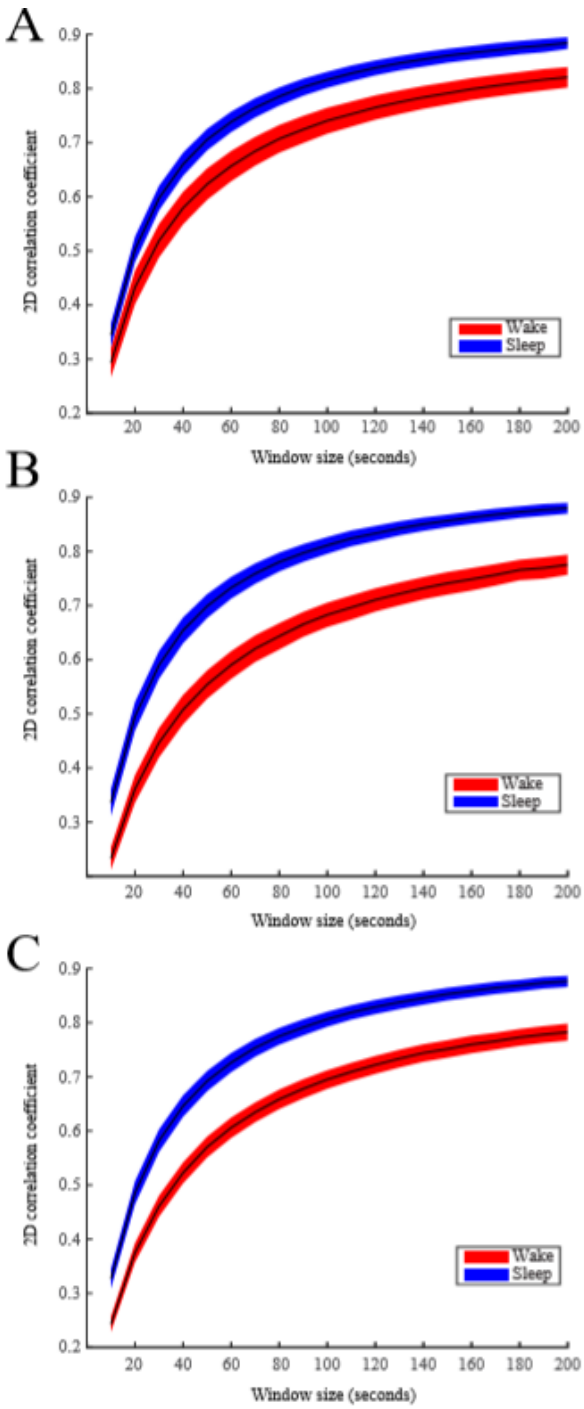

Figure 5.7 Network stability as a function of window size (M, see Section 5.2.2.7). We concatenated all awake and sleep data identified via the PCA/GMM automated classification and computed the network stability for each dataset. The black line shows the mean of the group correlation coefficients and the shaded area represents the 95% confidence interval for the mean. Results are shown for (A) IS patients, (B) diseased controls, and (C) healthy controls.

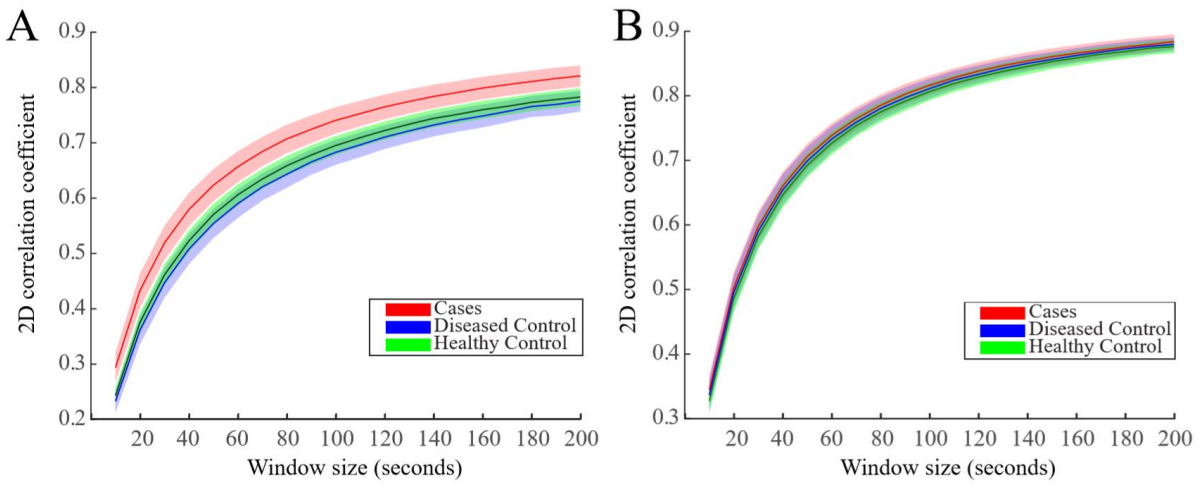

Figure 5.8 Network stability as a function of window size in (A) wakefulness and (B) sleep. The solid line shows the mean of the group correlation coefficients and the shaded area represents the 95% confidence interval for the mean.

5.2.4 Discussion

Here we have identified EEG-based functional connectivity properties that significantly differed between IS patients, diseased controls, and healthy controls as a function of sleep stage over a 24-hour period. We first found that functional connections are stronger in sleep than wakefulness, corroborating our findings in the refractory patient cohort (Figure 5.5, see also Figure 5.1 and 5.2). On the group level, the mean values remained fairly constant over time (Figure 5.5); however analysis of individual datasets would need to be performed to address stationarity of the connectivity strength within a specific waking or sleeping period. Additionally, consistent with our findings in the refractory patient cohort, the strength of the networks in IS cases was higher than both the diseased and healthy controls (Figure 5.5).

Evaluating the strength of the functional connectivity network for patients with IS may have clinical value. It has been shown in previous work that the pre-treatment functional connectivity network measured with cross-correlation may predict successful treatment

outcomes [80]. In that cohort (described in Section 2.1.2.1) six out of eleven patients that responded to therapy exhibited extremely strong functional connections pre-treatment, while non-responders did not show elevated pre-treatment connection strengths [80]. These data suggest that the pathologically strong connections seen in these cohorts of IS patients may indicate a receptivity to drug intervention [80], however a larger prospective study is needed to confirm this.

We also showed that, although sleep generally exhibited higher connection strengths than wakefulness, the time of day simultaneously modulated the strength of the functional connections. Nighttime was typically associated with stronger connections, even when the child was awake and vice versa. Similar long-term periodicities have been reported in several recent studies. One study using functional connectivity network changes to predict the onset of seizures found that the physiological functional network changes far outweighed the changes associated with seizure onset, but that seizure onset was phase-locked with some of these physiological periodicities [183]–[185]. The oscillations had periods of 3.4, 5.6, 12, and 24 hours [183]. In intracranial EEG, it was shown that functional networks were assortative before seizure onset and switch to dissortative during the seizure, but they also reported 24-hour periodicities in the assortativity factor [186], indicating that the pathophysiological activity was modifying the network in a process-specific way [186]. Studies of network centrality [187], clustering coefficient [188], and average shortest path length [188] all find that daily rhythms dominate network dynamics in long-term functional connectivity measurements. In our study, an expanded analysis of graph theory metrics may further elucidate some of the circadian changes seen in our dataset.

It is important to note that our finding of a disrupted circadian rhythm in IS patients coincides with literature on infantile spasms. Clinical studies note that sleep/wake cycles, and specifically slow wave sleep, are often disrupted IS [189], [190]. The spasms themselves can also often be triggered by drowsiness, N1 sleep, REM sleep, or upon arousal [8], suggesting a circadian component to ictal time periods.

Lastly, although the visual appearance of the EEG in infantile spasms is described as "chaotic" and "disorganized" [11], we find that these networks are more stable than those of healthy age-matched controls (Figure 5.7 and 5.8). This suggests that the pathological substrates facilitating the abnormal EEG patterns and hyper-connectivity are robust, implying network properties could be used in therapeutic assessment. In future work, we plan to test the hypothesis that these network changes can provide a patient-specific and early biomarker of treatment response.

REFERENCES

[1] S. L. Moshé, E. Perucca, P. Ryvlin, and T. Tomson, "Epilepsy: new advances," *Lancet*, vol. 385, pp. 884–898, 2015.

[2] R. S. Fisher *et al.*, "ILAE Official Report: A practical clinical definition of epilepsy," *Epilepsia*, vol. 55, no. 4, pp. 475–482, 2014.

[3] S. Khan and R. Al Baradie, "Epileptic Encephalopathies: An Overview," *Epilepsy Res. Treat.*, vol. 2012, pp. 1–8, 2012.

[4] J. Engel and International League Against Epilepsy (ILAE), "A proposed diagnostic scheme for people with epileptic seizures and with epilepsy: report of the ILAE Task Force on Classification and Terminology.," *Epilepsia*, vol. 42, no. 6, pp. 796–803, 2001.

[5] R. S. Fisher *et al.*, "Operational classification of seizure types by the International League Against Epilepsy: position paper of the ILAE Commission for Classification and Terminology," *Zeitschrift fur Epileptol.*, vol. 31, no. 4, pp. 272–281, 2018.

[6] G. L. Westbrook, "Seizures and Epilepsy," in *Principles of Neural Science*, 5th ed., E. R. Kandel, J. H. Schwartz, T. M. Jessell, S. A. Siegelbaum, and A. J. Hudspeth, Eds. The McGraw-Hill Companies, Inc., 2013, pp. 1116–1139.

[7] A. Nehlig, A. Coppola, and S. Moshe, *Epileptic Syndromes in Infancy, Childhood, and Adolescence*, 5th ed. Montrouge, France: John Libbey Eurotext, 2012.

[8] P. Pavone, P. Striano, R. Falsaperla, L. Pavone, and M. Ruggieri, "Infantile spasms syndrome, West syndrome and related phenotypes: What we know in 2013," *Brain Dev.*, vol. 36, no. 9, pp. 739–751, 2013.

[9] J. M. Pellock *et al.*, "Infantile spasms: A U.S. consensus report," *Epilepsia*, vol. 51, no. 10, pp. 2175–2189, 2010.

[10] R. A. Hrachovy and J. D. Frost, "Infantile Epileptic Encephalopathy with Hypsarrhythmia (Infantile spasms/West syndrome).," *J. Clin. Neurophysiol.*, vol. 20, no. 6, pp. 408–425, 2003.

[11] E. L. Gibbs, M. M. Fleming, and F. A. Gibbs, "Diagnosis and Prognosis of Hypsarrhythmia and Infantile Spasms," *Pediatrics*, vol. 13, no. 1, pp. 66–73, 1953.

[12] A. T. Berg *et al.*, "Revised terminology and concepts for organization of seizures and epilepsies: Report of the ILAE Commission on Classification and Terminology, 2005-2009," *Epilepsia*, vol. 51, no. 4, pp. 676–685, 2010.

[13] K. Staley, "Molecular mechanisms of epilepsy," *Nat. Neurosci.*, vol. 18, no. 3, pp. 367–372, 2015.

[14] A. J. Hani, H. M. Mikati, and M. A. Mikati, "Genetics of Pediatric Epilepsy," *Pediatr. Clin. North Am.*, vol. 62, no. 3, pp. 703–722, 2015.

[15] R. S. Riikonen, "Favourable prognostic factors with infantile spasms," *Eur. J. Paediatr. Neurol.*, vol. 14, no. 1, pp. 13–18, 2010.

[16] W. D. Shields, "Infantile spasms: little seizures, BIG consequences.," *Epilepsy Curr.*, vol. 6, no. 3, pp. 63–9, 2006.

[17] J. P. Osborne *et al.*, "The underlying etiology of infantile spasms (West syndrome): Information from the United Kingdom Infantile Spasms Study (UKISS) on contemporary causes and their classification," *Epilepsia*, vol. 51, no. 10, pp. 2168–2174, 2010.

[18] L. Pavone, F. Mollica, G. Incorpora, and G. Pampiglione, "Infantile spasms syndrome in monozygotic twins," *Arch. Dis. Child.*, vol. 55, pp. 870–872, 1980.

[19] K. Hemminki, X. Li, S.-E. Johansson, K. Sundquist, and J. Sundquist, "Familial Risks for Epilepsy among Siblings Based on Hospitalizations in Sweden," *Neuroepidemiology*, vol. 27, no. 2, pp. 67–73, 2006.

[20] K. M. Fiest *et al.*, "Prevalence and incidence of epilepsy: A systematic review and meta-analysis of international studies," *Neurology*, vol. 88, pp. 296–303, 2017.

[21] J. M. Wilmshurst, R. C. Ibekwe, and F. J. K. O'Callaghan, "Epileptic spasms — 175 years on: Trying to teach an old dog new tricks," *Seizure*, vol. 44, pp. 81–86, 2017.
[22] E. Gaily, M. Lommi, R. Lapatto, and A. E. Lehesjoki, "Incidence and outcome of epilepsy syndromes with onset in the first year of life: A retrospective population-based study," *Epilepsia*, vol. 57, no. 10, pp. 1594–1601, 2016.
[23] M. R. Keezer, S. M. Sisodiya, and J. W. Sander, "Comorbidities of epilepsy: current concepts and future perspectives," *Lancet Neurol.*, vol. 15, no. 1, pp. 106–115, 2016.
[24] J. F. Téllez-Zenteno, L. H. Ronquillo, and S. Wiebe, "Sudden unexpected death in epilepsy: Evidence-based analysis of incidence and risk factors," *Epilepsy Res.*, vol. 65, no. 1–2, pp. 101–115, 2005.
[25] M. I. Lossius *et al.*, "Comorbidity and Childhood Epilepsy: A Nationwide Registry Study," *Pediatrics*, vol. 138, no. 3, pp. e20160921–e20160921, 2016.
[26] A. Pitkänen *et al.*, "Advances in the development of biomarkers for epilepsy," *Lancet Neurol.*, vol. 15, no. 8, pp. 843–856, 2016.
[27] A. Bragin, J. Engel, C. L. Wilson, I. Fried, and G. W. Mathern, "Hippocampal and entorhinal cortex high-frequency oscillations (100-500 Hz) in human epileptic brain and in kainic acid-treated rats with chronic seizures," *Epilepsia*, vol. 40, no. 2, pp. 127–137, 1999.
[28] L. P. Andrade-Valenca, F. Dubeau, F. Mari, R. Zelmann, and J. Gotman, "Interictal scalp fast oscillations as a marker of the seizure onset zone," *Neurology*, vol. 77, pp. 524–531, 2011.
[29] J. Wang *et al.*, "Circulating microRNAs are promising novel biomarkers for drug-resistant epilepsy," *Sci. Rep.*, vol. 5, pp. 1–10, 2015.
[30] J. Wang *et al.*, "Genome-wide circulating microRNA expression profiling indicates biomarkers for epilepsy," *Sci. Rep.*, vol. 5, 2015.
[31] A. Labate *et al.*, "White matter abnormalities differentiate severe from benign temporal lobe epilepsy," *Epilepsia*, vol. 56, no. 7, pp. 1109–1116, 2015.
[32] S. Auvin *et al.*, "Diagnosis delay in West syndrome: misdiagnosis and consequences," *Eur. J. Pediatr.*, vol. 171, no. 11, pp. 1695–1701, 2012.
[33] L. Fusco and F. Vigevano, "Ictal Clinical Electroencephalographic Findings of Spasms in West Syndrome," *Epilepsia*, vol. 34, no. 4, pp. 671–678, 1993.
[34] S. A. Hussain *et al.*, "Hypsarrhythmia assessment exhibits poor interrater reliability: A threat to clinical trial validity," *Epilepsia*, vol. 56, no. 1, pp. 77–81, 2015.
[35] J. R. Mytinger *et al.*, "Improving the inter-rater agreement of hypsarrhythmia using a simplified EEG grading scale for children with infantile spasms," *Epilepsy Res.*, vol. 116, pp. 93–98, 2015.
[36] E. Perucca, "An Introduction to Antiepileptic Drugs," *Epilepsia*, vol. 46, no. 4, pp. 31–37, 2005.
[37] B. C. Jobst and G. D. Cascino, "Resective Epilepsy Surgery for Drug-Resistant Focal Epilepsy: A Review," *JAMA*, vol. 313, no. 3, pp. 285–293, 2015.
[38] A. Mehdizadeh, M. Barzegar, S. Negargar, A. Yahyavi, and S. Raeisi, "The current and emerging therapeutic approaches in drug-resistant epilepsy management," *Acta Neurol. Belg.*, 2019.
[39] S. Wiebe, W. T. Blume, J. P. Girvin, and M. Eliasziw, "a Randomized, Controlled Trial of Surgery," *N. Engl. J. Med.*, vol. 345, no. 5, pp. 311–318, 2001.
[40] W. H. Theodore and R. Fisher, *Operative Neuromodulation*. 2007.
[41] F. Vigevano and M. R. Cilio, "Vigabatrin versus ACTH as first-line treatment for infantile spasms: a randomized, prospective study.," *Epilepsia*, vol. 38, no. 12, pp. 1270–1274, 1997.
[42] F. Stamps, E. Gibbs, I. Rosenthal, and F. Gibbs, "Treatment of Hypsarrhythmia with ACTH," *J.A.M.A.*, vol. 171, no. 4, pp. 116–119, 1959.
[43] K. G. Knupp *et al.*, "Response to Treatment in a Prospective National Infantile Spasms Cohort," *Ann. Neurol.*, vol. 49, no. 2, pp. 475–484, 2016.
[44] R. Riikonen and M. Donner, "ACTH therapy in infantile spasms: side effects.," *Arch. Dis. Child.*, vol. 55, no. 9, pp. 664–672, 1980.

[45] C. Y. Go *et al.*, "Evidence-based guideline update: Medical treatment of infantile spasms," *Am. Acad. Neurol.*, vol. 78, pp. 1974–1980, 2012.
[46] C. Chiron, C. Dumas, I. Jambaqué, J. Mumford, and O. Dulac, "Randomized trial comparing vigabatrin and hydrocortisone in infantile spasms due to tuberous sclerosis," *Epilepsy Res.*, vol. 26, no. 2, pp. 389–395, 1997.
[47] A. L. Lux *et al.*, "The United Kingdom Infantile Spasms Study (UKISS) comparing hormone treatment with vigabatrin on developmental and epilepsy outcomes to age 14 months: A multicentre randomised trial," *Lancet Neurol.*, vol. 4, no. 11, pp. 712–717, 2005.
[48] L. S. Gold *et al.*, "Healthcare Costs and Resource Utilization in Patients with Infantile Spasms Treated with H.P. Acthar Gel®," *Adv. Ther.*, vol. 33, no. 8, pp. 1293–1304, 2016.
[49] B. E., F. B., B. M., D. C. P., and G. L., "A review of the costs of managing childhood epilepsy," *Pharmacoeconomics*, vol. 23, no. 1, pp. 27–45, 2005.
[50] A. Argumosa and J. L. Herranz, "El coste economico de la epilepsia infantil en Espana," *Rev Neurol*, vol. 30, pp. 104–8, 2000.
[51] H. Rantala and T. Putkonen, "Occurrence, outcome, and prognostic factors of infantile spasms and Lennox-Gastaut syndrome," *Epilepsia*, vol. 40, no. 3, pp. 286–289, 1999.
[52] W. C. Sue, M. A. Mikati, and U. Kramer, "Hypsarrhythmia: Frequency and variant patterns and correlation with etiology and outcome," *Neurology*, vol. 48, no. 1, pp. 197–203, 1997.
[53] B. P. Mohamed, R. C. Scott, N. Desai, P. Gutta, and S. Patil, "Seizure outcome in infantile spasms-A retrospective study," *Epilepsia*, vol. 52, no. 4, pp. 746–752, 2011.
[54] S. Kivity, P. Lerman, R. Ariel, Y. Danziger, M. Mimouni, and S. Shinnar, "Long-term Cognitive Outcomes of a Cohort of Children with Cryptogenic Infantile Spasms Treated with High-dose Adrenocorticotropic Hormone," *Epilepsia*, vol. 45, no. 3, pp. 255–262, 2004.
[55] R. Riikonen, "Long-term outcome of patients with West syndrome," *Brain Dev.*, vol. 23, no. 7, pp. 683–687, 2001.
[56] E. Friedman and G. Pampiglione, "Prognostic implications of electroencephalographic findings of hypsarrhythmia in first year of life.," *Br. Med. J.*, vol. 4, no. 5783, pp. 323–325, 1971.
[57] F. H. Lopes Da Silva, "EEG: Origin and Measurement," in *EEG-fMRI*, 2009, pp. 19–39.
[58] N. Schaul, "The Fundamental Neural Mechanisms of EEG," *Electroencephalogr. Clin. Neurophysiol.*, vol. 106, no. October 1997, pp. 101–7, 1998.
[59] A. F. Jackson and D. J. Bolger, "The neurophysiological bases of EEG and EEG measurement: A review for the rest of us," *Psychophysiology*, vol. 51, no. 11, pp. 1061–1071, 2014.
[60] A. J. Rowan and E. Tolunsky, *Primer of EEG with a Mini-Atlas*. 2003.
[61] B. J. Fisch, *Fisch and Spehlmann's EEG Primer: Basic Principles of Digital and Analog EEG*, 3rd ed. Oxford, UK: Elsevier Ltd, 1999.
[62] P. Laoprasert, *Atlas of Pediatric EEG*, 1st ed. The McGraw-Hill Companies, Inc., 2011.
[63] J. M. Stern, *Atlas of EEG Patterns*, 2nd ed. Philadelphia, PA: Lippincott Williams & Wilkins, 2005.
[64] K. Kobayashi, T. Akiyama, M. Oka, F. Endoh, and H. Yoshinaga, "Fast (40-150Hz) oscillations are associated with positive slow waves in the ictal EEGs of epileptic spasms in West syndrome," *Brain Dev.*, vol. 38, no. 10, pp. 909–914, 2016.
[65] K. Kobayashi, T. Akiyama, M. Oka, F. Endoh, and H. Yoshinaga, "A storm of fast (40-150Hz) oscillations during hypsarrhythmia in West syndrome," *Ann. Neurol.*, vol. 77, no. 1, pp. 58–67, 2015.
[66] J. Y. Wu, S. Koh, R. Sankar, and G. W. Mathern, "Paroxysmal fast activity: An interictal scalp EEG marker of epileptogenesis in children," *Epilepsy Res.*, vol. 82, no. 1, pp. 99–106, 2008.
[67] R. H. Caraballo *et al.*, "Epileptic spasms in clusters with focal EEG paroxysms: A study of 12 patients," *Seizure*, vol. 35, no. 1, pp. 88–92, 2016.
[68] E. Gaily, E. Liukkonen, R. Paetau, M. Rekola, and M.-L. Granström, "Infantile spasms: diagnosis

and assessment of treatment response by video-EEG," *Dev. Med. Child Neurol.*, vol. 43, no. 10, pp. 658–667, 2010.
[69] R. A. Hrachovy, J. D. Frost, and P. Kellaway, "Hypsarrhythmia: variations on the theme," *Epilepsia*, vol. 25, no. 3, pp. 317–325, 1984.
[70] A. L. Lux and J. P. Osborne, "A proposal for case definitions and outcome measures in studies of infantile spasms and West syndrome: Consensus statement of the West Delphi Group," *Epilepsia*, vol. 45, no. 11, pp. 1416–1428, 2004.
[71] R. Sehgal, S. Gulati, S. Sapra, M. Tripathi, R. M. Pandey, and M. Kabra, "Prognostic Utility of Clinical Epilepsy Severity Score Versus Pretreatment Hypsarrhythmia Scoring in Children With West Syndrome.," *Clin. EEG Neurosci.*, vol. 48, no. 4, pp. 280–287, 2017.
[72] A. Altunel, A. Sever, and E. Ö. Altunel, "Hypsarrhythmia paroxysm index: A tool for early prediction of infantile spasms," *Epilepsy Res.*, vol. 111, pp. 54–60, 2015.
[73] S. T. Demarest *et al.*, "The impact of hypsarrhythmia on infantile spasms treatment response: Observational cohort study from the National Infantile Spasms Consortium," *Epilepsia*, vol. 58, no. 12, pp. 2098–2103, 2017.
[74] R. H. Caraballo *et al.*, "Infantile spams without hypsarrhythmia: A study of 16 cases," *Seizure*, vol. 20, no. 3, pp. 197–202, 2011.
[75] R. H. Caraballo *et al.*, "Epileptic spasms in clusters without hypsarrhythmia in infancy," *Epileptic Disord.*, vol. 5, no. 2, pp. 109–113, 2003.
[76] K. Yamada *et al.*, "Predictive value of EEG findings at control of epileptic spasms for seizure relapse in patients with West syndrome," *Seizure*, vol. 23, no. 9, pp. 703–707, 2014.
[77] Y. Hayashi, H. Yoshinaga, T. Akiyama, F. Endoh, Y. Ohtsuka, and K. Kobayashi, "Predictive factors for relapse of epileptic spasms after adrenocorticotropic hormone therapy in West syndrome," *Brain Dev.*, vol. 38, no. 1, pp. 32–39, 2016.
[78] Y. J. Lee, G. M. Yeon, Y. M. Kim, and S. O. Nam, "Relationship between initial electroencephalographic characteristics and seizure outcomes in children with non-lesional West syndrome," *Epilepsy Res.*, vol. 110, pp. 49–54, 2015.
[79] F. Endoh, H. Yoshinaga, K. Kobayashi, and Y. Ohtsuka, "Electroencephalographic changes before the onset of symptomatic West syndrome," *Brain Dev.*, vol. 29, no. 10, pp. 630–638, 2007.
[80] D. W. Shrey, O. Kim McManus, R. Rajaraman, H. Ombao, S. A. Hussain, and B. A. Lopour, "Strength and stability of EEG functional connectivity predict treatment response in infants with epileptic spasms," *Clin. Neurophysiol.*, vol. 129, no. 10, pp. 2137–2148, 2018.
[81] S. A. Burroughs, R. P. Morse, S. H. Mott, and G. L. Holmes, "Brain connectivity in West syndrome," *Seizure Eur. J. Epilepsy*, vol. 23, no. 7, pp. 576–579, 2014.
[82] C. Chiron *et al.*, "Study of Regional Cerebral Blood Flow in West Syndrome," *Epilepsia*, vol. 34, no. 4, pp. 707–715, 1993.
[83] H. T. Chugani, D. A. Shewmon, R. Sankar, B. C. Chen, and M. E. Phelps, "Infantile spasms: II. Lenticular nuceli and brain stem activation on positron emission tomography," *Ann. Neurol.*, vol. 31, no. 2, pp. 212–219, 1992.
[84] M. Siniatchkin *et al.*, "Different neuronal networks are associated with spikes and slow activity in hypsarrhythmia," *Epilepsia*, vol. 48, no. 12, pp. 2312–2321, 2007.
[85] N. Japaridze *et al.*, "Neuronal networks in west syndrome as revealed by source analysis and renormalized partial directed coherence," *Brain Topogr.*, vol. 26, no. 1, pp. 157–170, 2013.
[86] Z. R. Primec, J. Stare, and D. Neubauer, "The risk of lower mental outcome in infantile spasms increases after three weeks of hypsarrhythmia duration," *Epilepsia*, vol. 47, no. 12, pp. 2202–2205, 2006.
[87] A. Delorme and S. Makeig, "EEGLAB: an open source toolbox for analysis of single-trial EEG dynamics," *J. Neurosci. Methods*, vol. 134, pp. 9–21, 2004.
[88] R. Grandchamp and A. Delorme, "Single-trial normalization for event-related spectral

decomposition reduces sensitivity to noisy trials," *Front. Psychol.*, vol. 2, no. SEP, pp. 1–14, 2011.
[89] S. Traitruengsakul, L. E. Seltzer, A. R. Paciorkowski, and B. Ghoraani, "Developing a novel epileptic discharge localization algorithm for electroencephalogram infantile spasms during hypsarrhythmia," *Med. Biol. Eng. Comput.*, vol. 55, no. 9, pp. 1659–1668, 2017.
[90] M. J. A. M. Van Putten and C. J. Stam, "Is the EEG really 'chaotic' in hypsarrhythmia?," *IEEE Eng. Med. Biol. Mag.*, vol. 20, no. 5, pp. 72–79, 2001.
[91] R. J. Smith, A. Sugijoto, N. Rismanchi, S. A. Hussain, D. W. Shrey, and B. A. Lopour, "Long-Range Temporal Correlations Reflect Treatment Response in the Electroencephalogram of Patients with Infantile Spasms," *Brain Topogr.*, vol. 30, no. 6, pp. 810–821, 2017.
[92] K. Linkenkaer-Hansen, V. V Nikouline, J. M. Palva, and R. J. Ilmoniemi, "Long-range temporal correlations and scaling behavior in human brain oscillations," *J. Neurosci.*, vol. 21, no. 4, pp. 1370–1377, 2001.
[93] T. Stadnitski, "Measuring fractality," *Front. Physiol.*, vol. 3, no. 127, pp. 1–13, 2012.
[94] A. Babloyantz and A. Destexhe, "Low-dimensional chaos in an instance of epilepsy," *Neurobiology*, vol. 83, no. 10, pp. 3513–3517, 1986.
[95] A. Liu, J. S. Hahn, G. P. Heldt, and R. W. Coen, "Detection of neonatal seizures through computerized EEG analysis," *Electroencephalogr. Clin. Neurophysiol.*, vol. 82, no. 1, pp. 30–37, 1992.
[96] D. J. A. Smit *et al.*, "Scale-free modulation of resting-state neuronal oscillations reflects prolonged brain maturation in humans," *J. Neurosci.*, vol. 31, no. 37, pp. 13128–13136, 2011.
[97] J. W. Kantelhardt, E. Koscielny-Bunde, H. H. . Rego, S. Havlin, and A. Bunde, "Detecting long-range correlations with detrended fluctuation analysis," *Phys. A Stat. Mech. its Appl.*, vol. 295, no. 3–4, pp. 441–454, 2001.
[98] Z. Chen, P. C. Ivanov, K. Hu, and H. E. Stanley, "Effect of nonstationarities on detrended fluctuation analysis," *Phys. Rev. E*, vol. 65, no. 4, 2002.
[99] R. Hardstone *et al.*, "Detrended fluctuation analysis: A scale-free view on neuronal oscillations," *Front. Physiol.*, vol. 3, no. 450, pp. 75–87, 2012.
[100] R. M. Bryce and K. B. Sprague, "Revisiting detrended fluctuation analysis.," *Sci. Rep.*, vol. 2, p. 315, 2012.
[101] J. M. Bardet and I. Kammoun, "Asymptotic Properties of the Detrended Fluctuation Analysis of Long Range Dependent Processes," *IEEE Trans. Inf. Theor.*, vol. 54, no. 5, pp. 2041–2052, 2008.
[102] T. C. Ferree and R. C. Hwa, "Power-law scaling in human EEG: relation to Fourier power spectrum," *Neurocomputing*, vol. 52–54, no. 1, pp. 755–761, 2003.
[103] N. Kannathal, J. Chee, K. Er, K. Lim, and O. H. Tat, "Chaotic Analysis of Epileptic EEG Signals," in *The 15th International Conference on Biomedical Engineering*, 2014, vol. IFMBE Proc, pp. 652–654.
[104] R. C. Hwa and T. C. Ferree, "Stroke detection based on the scaling properties of human EEG," in *Physica A: Statistical Mechanics and its Applications*, 2004, vol. 338, no. 1–2, pp. 246–254.
[105] S. Monto, S. Vanhatalo, M. D. Holmes, and J. M. Palva, "Epileptogenic neocortical networks are revealed by abnormal temporal dynamics in seizure-free subdural EEG," *Cereb. Cortex*, vol. 17, no. 6, pp. 1386–1393, 2007.
[106] L. M. Parish, G. A. Worrell, S. D. Cranstoun, S. M. Stead, P. Pennell, and B. Litt, "Long-range temporal correlations in epileptogenic and non-epileptogenic human hippocampus," *Neuroscience*, vol. 125, no. 4, pp. 1069–1076, 2004.
[107] J. S. Ebersole and T. A. Pedley, *Current Practice of Clinical Electroencephalography*, 3rd ed. Lippincott Williams & Wilkins, 2003.
[108] H. Hooshmand, R. Morganroth, and C. Corredor, "Significance of focal and lateralized beta activity in the EEG," *Clin. Electroencephalogr.*, vol. 11, no. 3, pp. 140–144, 1980.
[109] M. J. Cannon, D. B. Percival, D. C. Caccia, G. M. Raymond, and J. B. Bassingthwaighte,

"Evaluating scaled windowed variance methods for estimating the Hurst coefficient of time series.," *Physica A*, vol. 241, no. 3–4, pp. 606–626, 1997.
[110] C. K. Peng, S. V. Buldyrev, S. Havlin, M. Simons, H. E. Stanley, and A. L. Goldberger, "Mosaic organization of DNA nucleotides," *Phys. Rev. E*, vol. 49, no. 2, pp. 1685–1689, 1994.
[111] P. Talkner and R. O. Weber, "Power spectrum and detrended fluctuation analysis: Application to daily temperatures," *Phys. Rev. E*, vol. 62, no. 1, pp. 150–160, 2000.
[112] A. Schaefer, J. S. Brach, S. Perera, and E. Sejdić, "A comparative analysis of spectral exponent estimation techniques for 1/f processes with applications to the analysis of stride interval time series," *J. Neurosci. Methods*, vol. 222, pp. 118–130, 2014.
[113] K. Willson and D. P. Francis, "A direct analytical demonstration of the essential equivalence of detrended fluctuation analysis and spectral analysis of RR interval variability," *Physiol. Meas.*, vol. 24, no. 1, pp. N1–N7, 2003.
[114] K. Linkenkaer-Hansen, V. V Nikulin, J. M. Palva, K. Kaila, and R. J. Ilmoniemi, "Stimulus-induced change in long-range temporal correlations and scaling behaviour of sensorimotor oscillations," *Eur. J. Neurosci.*, vol. 19, no. 1, pp. 203–211, 2004.
[115] W. Samek, D. A. J. Blythe, G. Curio, K. R. Müller, B. Blankertz, and V. V. Nikulin, "Multiscale temporal neural dynamics predict performance in a complex sensorimotor task," *Neuroimage*, vol. 141, no. 1, pp. 291–303, 2016.
[116] V. V. Nikulin and T. Brismar, "Long-range temporal correlations in alpha and beta oscillations: Effect of arousal level and test-retest reliability," *Clin. Neurophysiol.*, vol. 115, no. 8, pp. 1896–1908, 2004.
[117] C. Hartley *et al.*, "Long-range temporal correlations in the EEG bursts of human preterm babies," *PLoS One*, vol. 7, no. 2, pp. 1–10, 2012.
[118] T. Fedele, E. Blagovechtchenski, M. Nazarova, Z. Iscan, V. Moiseeva, and V. V. Nikulin, "Long-Range Temporal Correlations in the amplitude of alpha oscillations predict and reflect strength of intracortical facilitation: Combined TMS and EEG study," *Neuroscience*, vol. 331, pp. 109–119, 2016.
[119] M. Herrojo Ruiz, S. Bin Hong, H. Hennig, E. AltenmÃ¼ller, and A. A. KÃ¼hn, "Long-range correlation properties in timing of skilled piano performance: the influence of auditory feedback and deep brain stimulation," *Front. Psychol.*, vol. 5, no. September, pp. 1–13, 2014.
[120] R. L. Burr, C. J. Kirkness, and P. H. Mitchell, "Detrended fluctuation analysis of intracranial pressure predicts outcome following traumatic brain injury," *IEEE Trans. Biomed. Eng.*, vol. 55, no. 11, pp. 2509–2518, 2008.
[121] V. Matic *et al.*, "Objective differentiation of neonatal EEG background grades using detrended fluctuation analysis," *Front. Hum. Neurosci.*, vol. 9, no. 189, pp. 1–14, 2015.
[122] H. E. Hurst, "Long-term storage capacity of reservoirs," *Trans. Am. Soc. Civ. Eng.*, vol. 116, no. 770, 1951.
[123] B. B. Mandelbrot and J. R. Wallis, "Some long-run properties of geophysical records," *Water Resour. Res.*, vol. 5, no. 2, pp. 321–340, 1969.
[124] J. B. Bassingthwaighte and G. M. Raymond, "Evaluating rescaled ranged analysis for time series.," *Ann. Biomed. Eng.*, vol. 22, no. 4, pp. 432–444, 1994.
[125] J. B. Bassingthwaighte and G. M. Raymond, "Evaluation of the dispersional analysis method for fractal time series," *Ann. Biomed. Eng.*, vol. 23, no. 4, pp. 491–505, 1995.
[126] K. Linkenkaer-Hansen *et al.*, "Genetic Contributions to Long-Range Temporal Correlations in Ongoing Oscillations," *J. Neurosci.*, vol. 27, no. 50, pp. 13882–13889, 2007.
[127] R. Y. Liu and K. Singh, "Moving Blocks Jackknife and Bootstrap Capture Weak Dependence," in *Exploring the Limits of the Bootstrap*, R. LePage and L. Billard, Eds. New York: Wiley, 1992, pp. 225–248.
[128] H. R. Kunsch, "The Jackknife and the Bootstrap for General Stationary Observations," *Ann. Stat.*,

vol. 17, no. 3, pp. 1217–1241, 1989.
[129] P. Bühlmann, “Bootstraps for Time Series,” *Stat. Sci.*, vol. 17, no. 1, pp. 52–72, 2002.
[130] P. Grau-Carles, “Bootstrap testing for detrended fluctuation analysis,” *Phys. A Stat. Mech. its Appl.*, vol. 360, no. 1, pp. 89–98, 2006.
[131] I. Cribben, R. Haraldsdottir, L. Y. Atlas, T. D. Wager, and M. A. Lindquist, “Dynamic connectivity regression: Determining state-related changes in brain connectivity,” *Neuroimage*, vol. 61, no. 4, pp. 907–920, 2012.
[132] I. Cribben and Y. Yu, “Estimating whole-brain dynamics by using spectral clustering,” *J. R. Stat. Soc. Ser. C Appl. Stat.*, vol. 66, no. 3, pp. 607–627, 2017.
[133] T. Zhang, Q. Yin, B. Caffo, Y. Sun, and D. Boatman-Reich, “Bayesian interference of high-dimensional, cluster-structured ordinary differential equation models with applications to brain connectivity studies,” *Ann. Appl. Stat.*, vol. 11, no. 2, pp. 868–897, 2017.
[134] T. Zhang, J. Wu, F. Li, B. Caffo, and D. Boatman-Reich, “A Dynamic Directional Model for Effective Brain Connectivity Using Electrocorticographic (ECoG) Time Series,” *J. Am. Stat. Assoc.*, vol. 110, no. 509, pp. 93–106, 2015.
[135] B. B. Mandelbrot and J. W. Van Ness, “Fractional Brownian Motions, Fractional Noises and Applications,” *SIAM Rev.*, vol. 10, no. 4, pp. 422–437, 1968.
[136] S. Stoev, “ffgn().” MathWorks, 2016.
[137] C. R. Dietrich and G. N. Newsam, “Fast and Exact Simulation of Stationary Gaussian Processes through Circulant Embedding of the Covariance Matrix,” *SIAM J. Sci. Comput.*, vol. 18, no. 4, pp. 1088–1107, 1997.
[138] T. Z. Baram, W. G. Mitchell, A. Tournay, O. C. Snead III, R. A. Hanson, and E. J. Horton, “High-dose Corticotropin (ACTH) verses Prednisone for Infantile Spasms: A Prospective, Randomized, Blinded Study,” *Pediatrics*, vol. 97, no. 3, pp. 375–379, 1996.
[139] R. Ton and A. Daffertshofer, “Model selection for identifying power-law scaling,” *Neuroimage*, vol. 136, pp. 215–226, 2016.
[140] D. N. Politis and J. P. Romano, “A circular block resampling procedure for stationary data,” in *Exploring the Limits of the Bootstrap*, R. LePage and L. Billard, Eds. New York: Wiley, 1992, pp. 263–270.
[141] S. N. Lahiri, *Resampling Methods for Dependent Data*. New York: Springer, 2003.
[142] B. D. Malamud and D. L. Turcotte, “Self-affine time series: measures of weak and strong persistence,” *J. Stat. Plan. Inference*, vol. 80, no. 1–2, pp. 173–196, 1999.
[143] P. Flandrin, “Wavelet Analysis and Synthesis of Fractional Brownian Motion,” *IEEE Trans. Inf. Theory*, vol. 38, no. 2, pp. 910–917, 1992.
[144] S. Thurner, M. C. Feurstein, and M. C. Teich, “Multiresolution Wavelet Analysis of Heartbeat Intervals Discriminates Healthy Patients from Those with Cardiac Pathology,” *Phys. Rev. Lett.*, vol. 80, no. 7, pp. 1544–1547, 1998.
[145] M. C. Teich, “Fractal Character of the Auditory Neural Spike Train,” *IEEE Trans. Biomed. Eng.*, vol. 36, no. 1, pp. 150–160, 1989.
[146] J. Sen Leu and A. Papamarcou, “On Estimating the Spectral Exponent of Fractional Brownian Motion,” *IEEE Trans. Inf. Theory*, vol. 41, no. 1, pp. 233–244, 1995.
[147] G. M. Raymond and J. B. Bassingthwaighte, “Deriving dispersional and scaled windowed variance analyses using the correlation function of discrete fractional Gaussian noise,” *Phys. A Stat. Mech. its Appl.*, vol. 265, no. 1–2, pp. 85–96, 1999.
[148] Y. Shao, G. Gu, Z. Jiang, W. Zhou, and D. Sornette, “Comparing the performance of FA, DFA and DMA using different synthetic long-range correlated time series,” *Sci. Rep.*, vol. 2, no. 835, pp. 1–5, 2012.
[149] K. Hu, P. C. Ivanov, Z. Chen, P. Carpena, and H. Eugene Stanley, “Effect of trends on detrended fluctuation analysis,” *Phys. Rev. E*, vol. 64, no. 1, p. 011114, 2001.

[150] A. Montanari, M. S. Taqqu, and V. Teverovsky, “Estimating long-range dependence in the presence of periodicity: An empirical study,” *Math. Comput. Model.*, vol. 29, no. 10–12, pp. 217–228, 1999.
[151] R. J. Smith, A. Sugijoto, N. Rismanchi, S. A. Hussain, D. W. Shrey, and B. A. Lopour, “Long-Range Temporal Correlations Reflect Treatment Response in the Electroencephalogram of Patients with Infantile Spasms,” *Brain Topogr.*, vol. 30, no. 6, 2017.
[152] F. Crevecoeur, B. Bollens, C. Detrembleur, and T. M. Lejeune, “Towards a ‘ gold-standard ’ approach to address the presence of long-range auto-correlation in physiological time series,” *J. Neurosci. Methods*, vol. 192, no. 1, pp. 163–172, 2010.
[153] L. Berthouze and S. F. Farmer, “Adaptive time-varying detrended fluctuation analysis,” *J. Neurosci. Methods*, vol. 209, no. 1, pp. 178–188, 2012.
[154] E. A. F. Ihlen, “Introduction to multifractal detrended fluctuation analysis in Matlab,” *Front. Physiol.*, vol. 3, no. 141, pp. 1–18, 2012.
[155] M. Botcharova, S. F. Farmer, and L. Berthouze, “A maximum likelihood based technique for validating detrended fluctuation analysis (ML-DFA),” *arXiv:1306.5075*, 2013.
[156] C. J. Stam *et al.*, “Disturbed fluctuations of resting state EEG synchronization in Alzheimer’s disease,” *Clin. Neurophysiol.*, vol. 116, no. 3, pp. 708–715, 2005.
[157] J. S. Lee, B. H. Yang, J. H. Lee, J. H. Choi, I. G. Choi, and S. B. Kim, “Detrended fluctuation analysis of resting EEG in depressed outpatients and healthy controls,” *Clin. Neurophysiol.*, vol. 118, no. 11, pp. 2489–2496, 2007.
[158] R. J. Smith, D. W. Shrey, S. A. Hussain, and B. A. Lopour, “Quantitative Characteristics of Hypsarrhythmia in Infantile Spasms,” in *Proceedings of the Annual International Conference of the IEEE Engineering in Medicine and Biology Society, EMBS*, 2018, vol. 2018-July.
[159] F. J. K. O’Callaghan *et al.*, “The effect of lead time to treatment and of age of onset on developmental outcome at 4 years in infantile spasms: Evidence from the United Kingdom Infantile Spasms Study,” *Epilepsia*, vol. 52, no. 7, pp. 1359–1364, 2011.
[160] D. Schwender, M. Daunderer, S. Mulzer, S. Klasing, U. Finsterer, and K. Peter, “Spectral edge frequency of the electroencephalogram to monitor ‘depth’ of anaesthesia with isoflurane or propofol,” *Br. J. Anaesth.*, vol. 77, no. 2, pp. 179–184, 1996.
[161] C. E. Shannon, “A Mathematical Theory of Communication,” *Bell Syst. Tech. J.*, vol. 5, no. 3, p. 3, 1948.
[162] M. X. Cohen, *Analyzing Neural Time Series Data*. 2014.
[163] O. A. Rosso, W. Hyslop, R. Gerlach, R. L. L. Smith, J. A. P. Rostas, and M. Hunter, “Quantitative EEG analysis of the maturational changes associated with childhood absence epilepsy,” *Phys. A Stat. Mech. its Appl.*, vol. 356, no. 1, pp. 184–189, 2005.
[164] N. Kannathal, U. R. Acharya, C. M. Lim, and P. K. Sadasivan, “Characterization of EEG - A comparative study,” *Comput. Methods Programs Biomed.*, vol. 80, no. 1, pp. 17–23, 2005.
[165] N. Kannathal, M. L. Choo, U. R. Acharya, and P. K. Sadasivan, “Entropies for detection of epilepsy in EEG,” *Comput. Methods Programs Biomed.*, vol. 80, no. 3, pp. 187–194, 2005.
[166] D. Freedman and P. Diaconis, “On the histogram as a density estimator: L2 theory,” *Probab. Theory Relat. Fields*, vol. 57, no. 4, pp. 453–476, 1981.
[167] C. K. Peng *et al.*, “Long-range correlations in nucleotide sequences,” *Nature*, vol. 356, no. 6365, pp. 168–170, 1992.
[168] R. J. Smith, D. W. Shrey, S. A. Hussain, and B. Lopour, “Quantitative Characteristics of Hypsarrhythmia in Infantile Spasms,” *Conf Proc IEEE Eng Med Biol Soc*, pp. 538–541, 2018.
[169] C.-Y. Tsao, “Current trends in the treatment of infantile spasms,” *Neuropsychiatr. Dis. Treat.*, vol. 5, no. 1, pp. 289–299, 2009.
[170] R. D. Elterman, W. D. Shields, K. A. Mansfield, J. Nakagawa, and U. I. S. V. S. Group, “Randomized trial of vigabatrin in patients with infantile spasms,” *Neurology*, vol. 53, no. 8, 2001.

[171] J. Y. Wu, S. Koh, R. Sankar, and G. W. Mathern, “Paroxysmal Fast Activity: An Interictal Scalp EEG Marker of Epileptogenesis in Children,” *Epilepsy Res.*, vol. 82, no. 1, pp. 99–106, 2008.
[172] T. Inoue, K. Kobayashi, M. Oka, H. Yoshinaga, and Y. Ohtsuka, “Spectral characteristics of EEG gamma rhythms associated with epileptic spasms,” *Brain Dev.*, vol. 30, no. 5, pp. 321–328, 2008.
[173] K. Kobayashi *et al.*, “Very Fast Rhythmic Activity on Scalp EEG Associated with Epileptic Spasms,” *Epilepsia*, vol. 45, no. 5, pp. 488–496, 2004.
[174] C. J. Stam and E. C. W. van Straaten, “The organization of physiological brain networks,” *Clinical Neurophysiology*, vol. 123, no. 6. pp. 1067–1087, 2012.
[175] C. J. Honey *et al.*, “Predicting human resting-state functional connectivity from structural connectivity.,” *Proc. Natl. Acad. Sci. U. S. A.*, vol. 106, no. 6, pp. 2035–40, 2009.
[176] C. J. Chu *et al.*, “Emergence of Stable Functional Networks in Long-Term Human Electroencephalography,” *J. Neurosci.*, vol. 32, no. 8, pp. 2703–2713, 2012.
[177] J. Engel, P. M. Thompson, J. M. Stern, R. J. Staba, A. Bragin, and I. Mody, “Connectomics and epilepsy,” *Curr. Opin. Neurol.*, vol. 26, no. 2, pp. 186–194, 2013.
[178] M. A. Kramer and S. S. Cash, “Epilepsy as a disorder of cortical network organization,” *Neuroscientist*, vol. 18, no. 4, pp. 360–372, 2012.
[179] E. van Diessen, W. Otte, C. Stam, K. Braun, and F. Jansen, “Electroencephalography based functional networks in newly diagnosed childhood epilepsies,” *Clin. Neurophysiol.*, vol. 127, no. 6, pp. 2325–2332, 2016.
[180] A. E. L. Warren, D. F. Abbott, D. N. Vaughan, G. D. Jackson, and J. S. Archer, “Abnormal cognitive network interactions in Lennox-Gastaut syndrome: A potential mechanism of epileptic encephalopathy,” *Epilepsia*, vol. 57, no. 5, pp. 812–822, 2016.
[181] M. A. Kramer, U. T. Eden, S. S. Cash, and E. D. Kolaczyk, “Network interference with confidence from multivariate time series,” *Phys. Rev. E*, vol. 79, no. 6, 2009.
[182] T. Nichols and A. Holmes, “Nonparametric Permutation Tests for Functional Neuroimaging,” *Hum. Brain Funct. Second Ed.*, vol. 25, no. August 1999, pp. 887–910, 2003.
[183] G. D. Mitsis, M. N. Anastasiadou, M. Christodoulakis, E. S. Papathanasiou, S. S. Papacostas, and A. Hadjipapas, “Multi-scale periodicities in the functional brain networks of patients with epilepsy and their effect on seizure detection,” *bioRxiv*, 2017.
[184] M. Christodoulakis, A. Hadjipapas, E. S. Papathanasiou, M. Anastasiadou, S. S. Papacostas, and G. D. Mitsis, “Periodicity in functional brain networks: Application to scalp EEG from epilepsy patients,” in *Engineering in Medicine and Biology Society*, 2014, pp. 2805–2808.
[185] M. Anastasiadou, A. Hadjipapas, M. Christodoulakis, E. S. Papathanasiou, S. S. Papacostas, and G. D. Mitsis, “Epileptic seizure onset correlates with long term EEG functional brain network properties,” *Proc. Annu. Int. Conf. IEEE Eng. Med. Biol. Soc. EMBS*, vol. 2016-Octob, pp. 2822–2825, 2016.
[186] C. Geier, K. Lehnertz, and S. Bialonski, “Time-dependent degree-degree correlations in epileptic brain networks: from assortative to dissortative mixing,” *Front. Hum. Neurosci.*, vol. 9, no. August, pp. 1–11, 2015.
[187] C. Geier and K. Lehnertz, “Long-term variability of importance of brain regions in evolving epileptic brain networks,” *Chaos*, vol. 27, no. 4, 2017.
[188] M.-T. Kuhnert, C. E. Elger, and K. Lehnertz, “Long-term variability of global statistical properties of epileptic brain networks.,” *Chaos*, vol. 20, no. 2010, p. 043126, 2010.
[189] S. Fattinger, B. Schmitt, B. K. Bölsterli Heinzle, H. Critelli, O. G. Jenni, and R. Huber, “Impaired slow wave sleep downscaling in patients with infantile spasms,” *Eur. J. Paediatr. Neurol.*, vol. 19, no. 2, pp. 134–142, 2015.
[190] R. A. Hrachovy, J. D. Frost, and P. Kellaway, “Sleep characteristics in infantile spasms,” *Neurology*, vol. 31, no. 6, 1981.

APPENDIX A

AUTOMATIC ARTIFACT DETECTION

A.1 Introduction

EEG records the brain's electrical activity via electrodes placed on the subject's scalp. Because the potentials measured from the scalp are on the scale of microvolts, external factors such as patient movement and powerline noise can affect the voltage measurements and mask neural activity. Non-neural activity that affects the EEG signal are called artifacts. Artifacts can rise from subject movement, bad electrode contact, eye blinks, impedance checks, muscle activation, and a host of other things. Before making inferences about what is happening in the brain, these artifacts must be removed.

Physiological functions such as breathing, eye-blinking, and heartbeats can contaminate the EEG signal. When we are awake, the facial muscles around our scalp become activated and pollute the EEG. As such, it is not possible to remove all artifacts completely, but it is important to remove artifacts that mask the underlying neural activity.

There are several methods that are generally accepted to remove artifacts, but none are as thorough as visual identification of artifacts from a trained neurologist or EEG technician. However, this process is extremely time-consuming and often unfeasible for long-term studies. Thus, automatic artifact detection methods become necessary. We developed an automatic artifact detector with the aim to mimic visual marking by a trained clinician.

We compared our algorithm to visually marked artifacts in a retrospective dataset of 21 infantile spasms patients recorded at the Children's Hospital of Orange County (CHOC) (dataset

described in Section 2.1.2.1). Knowing that all artifacts could not be removed completely from the data, artifactual epochs that masked the underlying neural activity were visually marked. For example, muscle artifact and movement artifact that stood out from the background was marked. Eye blinks were marked, but smaller eye movements were often not marked. From these markings, we noticed that amplitude was a defining factor for whether an artifactual epoch was visually marked or not. We designed our artifact detector to match these artifact characteristics.

We primarily ensured that artifacts did not alter the results of specific analyses. For example, in our study of EEG amplitude, we wanted to remove artifacts that were going to inflate/deflate our measure of the amplitude. Thus, instead of testing the sensitivity and specificity of detecting the same artifactual time points that were visually-marked, we tested whether the data cleaned with our automatic artifact detector produced EEG amplitude results that were similar to the values calculated from data cleaned of visually-marked artifacts.

A.2 Methods

A.2.1 The algorithm

The algorithm first broadband bandpass filtered the data (1.5-40 Hz, butterworth filters). The mean was subtracted from each channel, and the standard deviation was calculated from the zero-mean time series. Then time points where the absolute value of the voltage exceeded a threshold of 7.5 standard deviations above or below the mean value in any single channel were marked. A buffer of 0.9 seconds was added to both sides of the marked extreme amplitude values to ensure that the entire artifact was marked. Data recorded during EEG impedance checks were also identified and marked.

A.2.2 Validation of the algorithm

We validated the automatic artifact detector on the retrospective dataset collected at CHOC (see Section 2.1.2.1). The dataset included 21 IS patients with 20-30 minute recordings both before and after treatment, resulting in 42 total datasets. Artifacts in these data were visually marked by a board-certified epileptologist at CHOC.

We calculated our five metrics of interest, namely 1) amplitude, 2) spectral edge frequency, 3) detrended fluctuation analysis, 4) functional connectivity, and 5) Shannon entropy. We first investigated how much the presence of artifacts affected each metric individually. The metric value obtained after removing artifacts that were visually marked will be labeled as CLEAN data, data without any artifact removal performed will be called ARTIFACT data, and data with automatically-detected artifacts removed will be termed AUTO data.

There were two parameters to be optimized in the automatic detection algorithm. First, the threshold that defined an "extreme value" was varied from four standard deviations above/below the mean to nine standard deviations above/below the mean. Second, the buffer time ranged from 0.2 seconds to 1.4 seconds. We calculated the buffer time to be 0.9 seconds via sensitivity/specificity measurements with visually-marked artifacts (data not shown).

To determine what threshold value would minimize the difference in the metric value between CLEAN data and AUTO data, we first calculated all metric values for CLEAN data, ARTIFACT data, and AUTO data with the threshold ranging from four to nine standard deviations above/below the mean. In every channel, we calculated the difference between the CLEAN data and ARTIFACT data as well as between CLEAN data and AUTO data with varying thresholds. We summed the absolute value of the differences over all channels and all patients to identify which threshold minimized the AUTO and CLEAN difference.

For each metric, we also calculated percent concordance for individual patients as the average absolute value of the difference between CLEAN and AUTO divided by the range of the CLEAN data, multiplied by 100:

$$percentConcordance = 100 - \frac{\frac{1}{k}\sum_{i=1}^{k}|auto_i - clean_i|}{\max(clean) - \min(clean)} * 100$$

where k is the number of channels in the data.

A.3 Results

We found that a threshold of 7.5-8 standard deviations above/below the mean minimized the difference between the metric values calculated from AUTO data and the metric values calculated from CLEAN data for most EEG features (Figure A.1). We chose 7.5 standard deviations above/below the mean for the final algorithm threshold. In some instances, the summed difference between AUTO data and CLEAN data was greater than the difference between ARTIFACT and CLEAN data, such as in the Amplitude calculation (Figure A.1A). This can happen when good data is marked, and its subsequent removal alters the metric value more than leaving the artifacts in. In the case of amplitude, when the automatic detector threshold was set to four standard deviations, the detector was identifying epochs of data that were clean, but were simply higher amplitude physiologically. As a result, the median amplitude value severely underestimated the true amplitude of the EEG signal and this was reflected in the high value of summed difference (Figure A.1A).

This effect also depends on the method in which the feature is calculated. In amplitude, for instance, we calculate the range of the data in one-second windows for the length of the time series and report the amplitude as the median of this distribution. By taking the median and not

the mean, we reduce the effect artifactual epochs have on the reported amplitude value (see also Figure A.7A).

We also assessed how ARTIFACT and AUTO data compared with CLEAN data on an individual patient and channel basis (Figures A.2-A.6). In each of these figures, panel A represents the difference between CLEAN data and ARTIFACT data for each metric calculated. Panel B reports the difference between CLEAN data and AUTO data with the threshold set to 7.5 standard deviations. Note that Patient 2, 6, and 20 had channels that were removed completely from the dataset, they are represented by the dark blue elements. Generally, in each case, the differences between the CLEAN and AUTO data were closer to zero than the differences between CLEAN and ARTIFACT data (Figures A.2-A.6). In some cases, the presence of artifacts generally increased or decreased the metric value. The DFA exponent is generally inflated by the presence of artifacts (Figure A.4A), but automatic removal of artifacts reduced these differences (Figure A.4B) (see also Section 3.3). Entropy was generally much lower in artifact data (Figure A.6A), and automatic artifact removal normalized the values to that of CLEAN data (Figure A.6B). The largest difference in amplitude between AUTO and CLEAN data was 58 μV, the mean absolute value difference was 3.25 μV, and the average percent concordance across patients was 95.3%. For SEF, percent concordance was 93.9%, the maximum difference was 17.2 Hz, and average difference was 0.84 Hz. For connectivity, the percent concordance was 94.0%, maximum difference was 0.66, and average difference was 0.07. For the DFA exponent calculation, percent concordance was 88.8%, maximum difference was 0.28, and average difference was 0.02. For entropy, percent concordance was 81.7%, maximum difference was 2.79 bits, and average difference was 0.17 bits.

Lastly, we report how the metric values vary between channels (Figure A.7). The figure shows the values in each channel averaged over all patients for ARTIFACT data (red line), CLEAN data (blue line), and AUTO data (green line). For EEG amplitude, as mentioned before, the difference between ARTIFACT data and CLEAN data is not large because we report the median value and not the mean (Figure A.7A). In other cases, such as entropy, the difference between ARTIFACT data and CLEAN data is substantial, and the AUTO data approaches the CLEAN line (Figure A.7D).

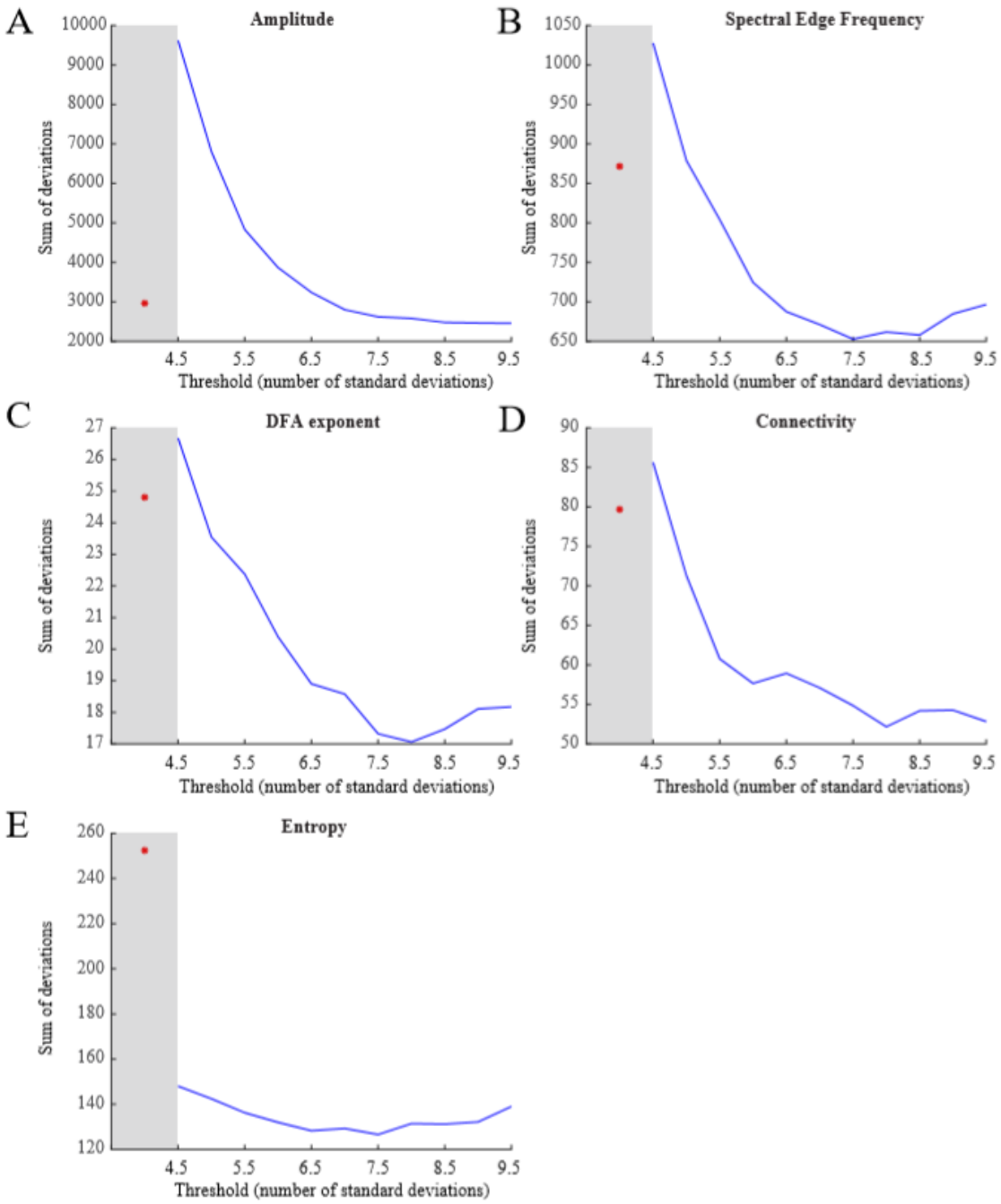

Figure A.1 Sum of differences over all patients and channels between CLEAN data and data with artifacts or data cleaned with automatic artifact removal. The sum of deviations is defined as the absolute value of the difference between the metric calculated on clean data and the metric calculated for artifact/automatically-cleaned data summed over all patient datasets. Data with no artifact removed is the red dot inside the grey shaded region, and the line denotes data with artifacts automatically removed using a varying threshold. The curves dip around 7.5 standard deviations, minimizing the difference between AUTO and CLEAN data metric value differences.

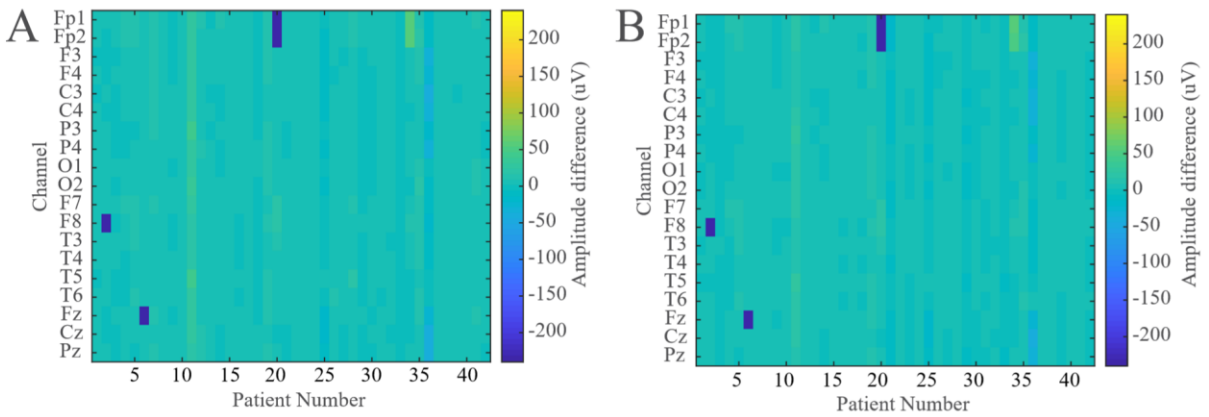

Figure A.2 Amplitude differences between clean data and (A) data with artifacts intact and (B) data cleaned with automatic artifact detection and removal with the threshold of detection set at 7.5 standard deviations above the mean and a 0.9 second buffer.

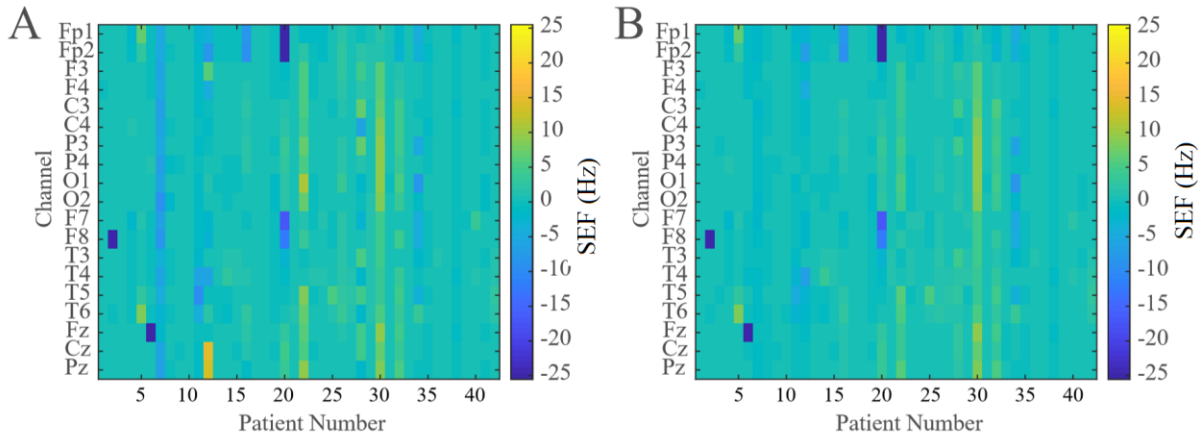

Figure A.3 Spectral edge frequency differences between clean data and (A) data with artifacts intact and (B) data cleaned with automatic artifact detection and removal with the threshold of detection set at 7.5 standard deviations above the mean and a 0.9 second buffer.

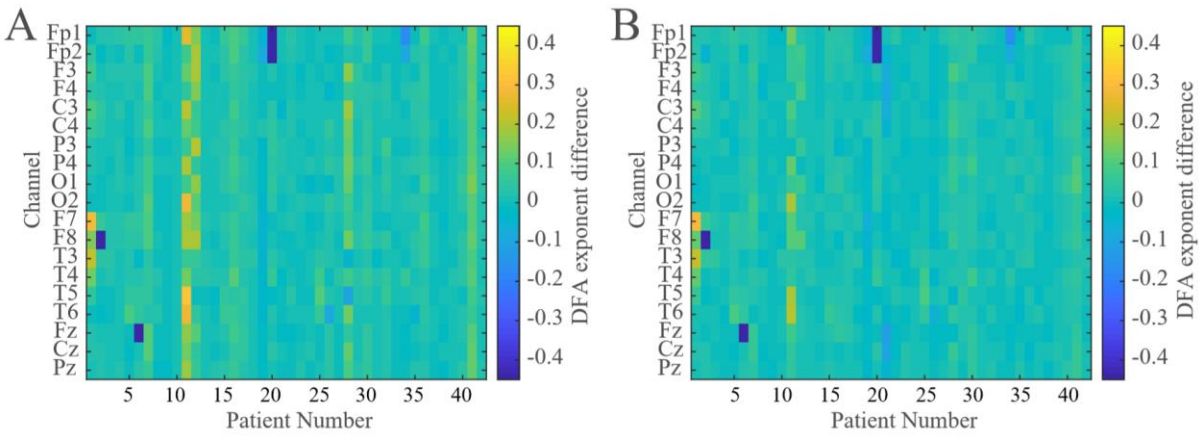

Figure A.4 DFA exponent differences between clean data and (A) data with artifacts intact, and (B) data cleaned with automatic artifact detection and removal with the threshold of detection set at 7.5 standard deviations above the mean and a 0.9 second buffer.

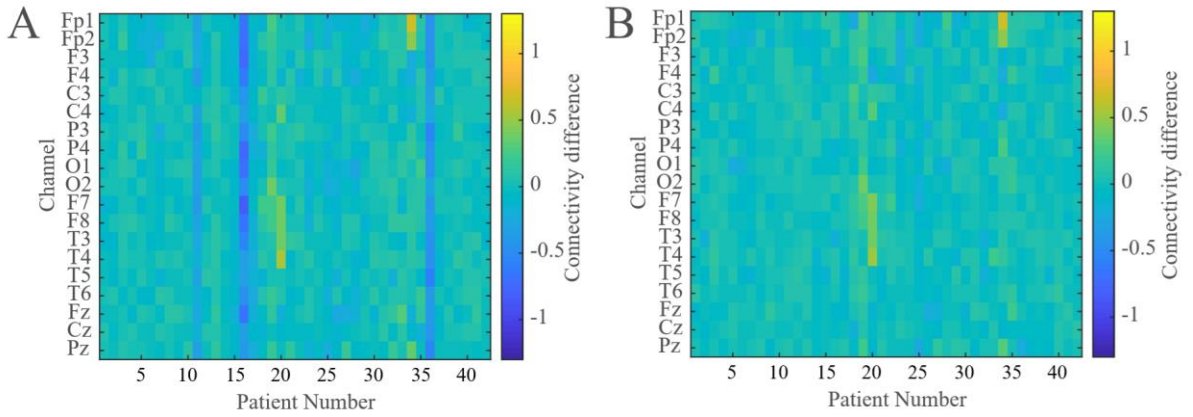

Figure A.5 Summed connectivity differences between clean data and (A) data with artifacts intact, and (B) data cleaned with automatic artifact detection and removal with the threshold of detection set at 7.5 standard deviations above the mean and a 0.9 second buffer.

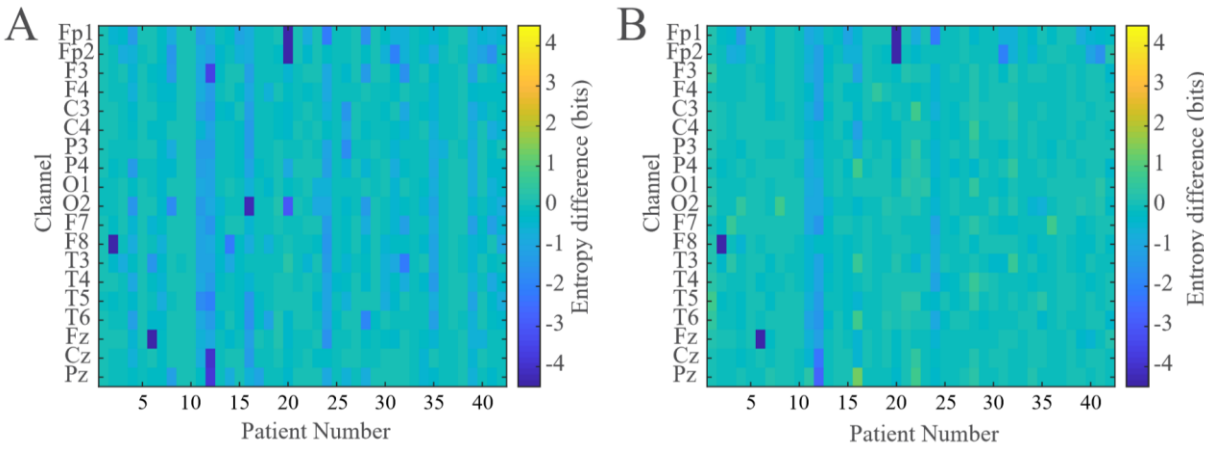

Figure A.6 Entropy differences between clean data and (A) data with artifacts intact, and (B) data cleaned with automatic artifact detection and removal with the threshold of detection set at 7.5 standard deviations above the mean and a 0.9 second buffer.

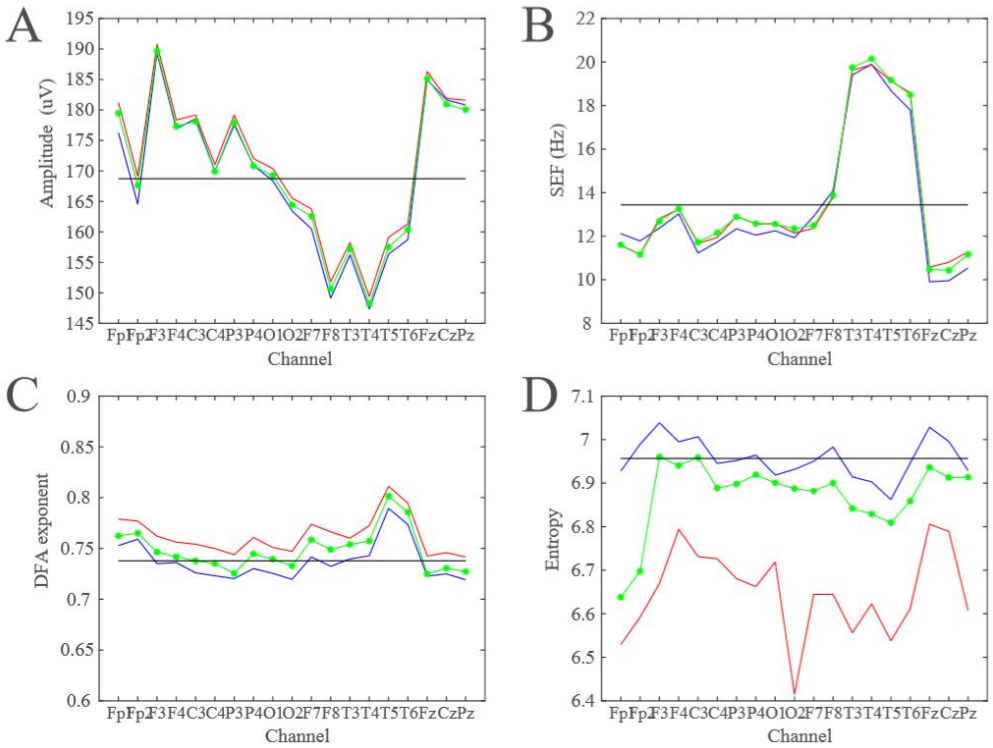

Figure A.7 Differences by channel between clean data (blue line) artifactual data (red line) and data with automated artifact detection (green line). Data is shown for (A) amplitude, (B) SEF, (C) DFA exponent, and (D) entropy. Threshold of detection for the automatic detector was set to 7.5 standard deviations above the mean and buffer was set to 0.9 seconds.

A.4 Discussion

Although many algorithms exist the identify and remove artifacts, we developed a method that identifies artifactual epochs such that our outcome metrics best align with visual artifact markings. In the future, other forms of artifact removal such as Independent Components Analysis (ICA) should be explored for use in this context. We did not use ICA in these analyses because we wanted a method of artifact detection that was completely supervised, but such methods may be extremely useful in long-term monitoring studies.